POLITECNICO DI MILANO

School of Industrial Engineering

Master of Science in Mechanical Engineering

Multiphysics Simulation of Electrostatically Actuated Micromirrors in Viscous Medium

Supervisor: Prof. Stefano Mariani
Co-Supervisor: Prof. Aldo Ghisi
Co-Supervisor: Dott. Marco De Fazio

Master of Science Thesis
by:
Ramin Mirzazadeh
Matr. 765206

July 2013

Contents

Acknowledgment

This section is appearing in the beginning of my thesis, but certainly is the last part to be written. Therefore, it is the first and only time, it is allowed to use “I”.

First of all, I want to express my sincerest gratitude to Prof. Stefano Mariani for his unceasing help and having trust on my capabilities more than I’ve ever asked for. Being his student is the greatest thing happened to me in POLIMI. I want to thank Prof. Aldo Ghisi for all of his kindness and useful helps in the times of need. I would like also to thank STMicroelectronics for their financial support for my research and in specific, Dott. Marco De Fazio for his supports and his useful technical comments.

I would like to thank my family. Simply I say: Maman, Baba and Shahin; merci. You are my life cornerstone; without you, I could not come this far.

These seven years of study have been great; not only because of what I have learnt but mostly because of getting the chance to find best friends everyone can wish for. So here, I should thank Ali, Ben, Mohammad, Larissa, Omid and Sirus for being there for me.

As always;

“Warm Wishes”

Ramin Mirzazadeh

List of Figures

List of Tables

Abstract

Electrostatically, comb-driven actuated MEMS (Micro-Electro-Mechanical Systems) micromirrors are of particular interest for a broad range of light manipulation applications like display, imaging, and telecommunication ones. They can meet the high-resolution, small size, low-power consumption and high-scanning speed requirements in such demanding applications. These resonating apparatuses are surrounded by air, which modifies the dynamics of the system. Study of these modifications and developing relevant simulation tools are important needs for design optimization.

The rotational resonance frequency of a micromirror is investigated in this thesis by a numerical modeling capable of taking account of the presence of residual stress in the device and fluid-structural interaction (FSI) between air and the micromirror interface. Viscous dissipation at the narrow gap between combfingers, as the dominant loss mechanism for the air-packaged micromirror, has been studied. First, an analytical model for simplified geometry and small oscillations has been provided, and the necessity of including slip boundary condition in the simulations has been investigated. Then, the detailed air flow between combfingers in the large angle oscillations has been modeled by a three-dimensional (3-D) computational-fluid-dynamics (CFD) simulation. Due to the mesh deformation, a constant remeshing method has been adopted. Also, the drag damping at the surface of the tilting micromirror is simulated. The quality factor corresponding to each dissipation mechanism has been obtained, and the overall value compared well with the available experimental results.

Keywords: Resonant micromirror, FSI, air damping, combdrive, quality factor, CFD.

Chapter 1

Introduction and thesis outline

Micro Electro Mechanical Systems (MEMS) are devices, whose characteristic length varies in the range between 1 μm (10^{-6} m) and 1 mm (10^{-3} m). In MEMS, electrical and mechanical components are combined by means of Integrated Circuit (IC) batch-processing technologies. Current manufacturing techniques for MEMS include surface silicon micromachining, bulk silicon micromachining, lithography, electrodeposition and plastic molding, and electrodischarge machining [1].

From a technological viewpoint, MEMS represent a development of the ICs fabrication technology, by extending the functionality of silicon components into many new applications such as sensors, actuators, integrated lab-on-a-chip products, and so on. The interesting point about this technology is its compatibility with the older equipments, since the lithography is not sub-micron deep. Moreover, the components are fabricated in a side-by-side array on wafer and by appropriate control procedure they can be much more precise and repeatable than similar products manufactured in other ways.

The possibility to exploit ICs fabrication technology allows obtaining in a straightforward manner also the connection between electronics and mechanical parts. In fact, almost all MEMS devices eventually need to be interfaced to a control system, and this is invariably in the form of an electronic one. In a final product, it is quite possible that a microcontroller is employed, which also requires some signal-conditioning circuits. The full system can then be easily packaged in a single device [2].

Microelectronic integrated circuits can be thought of as the ”brains” of systems, and MEMS augment this decision-making capability with ”eyes” and ”arms”, to allow microsystems to sense and control the environment. In its most basic form, the sensors gather information from the environment through measuring mechanical, thermal, biological, chemical, optical, and magnetic phenomena. The electronics process the information derived from the sensors and through some decision making capability direct the actuators to respond by moving, positioning, regulating, pumping, manipulating, thereby controlling the environment for some desired outcome or purpose.

In the last 20 years, a number of well known industrial success cases came from the MEMS field, such as inkjet printheads, pressure sensors, accelerometers and gyroscopes, devices for optics and communication technology, bio-chips and microfluidics devices. Applications range from automotive, aeronautics, aerospace, biomedicals, to consumer markets [3].

Among the aforementioned industrial applications, devices for optics known as Micro-Opto-Electro-Mechanical Systems (MOEMS), form a wide range of apparatuses such as tunable lasers [4], variable optical attenuators [5], optical switching [6-9], scanners and displays [10]. Micromirrors are an important element operating in these apparatuses. Various types of micromirrors are introduced and commercialized for different engineering targets.

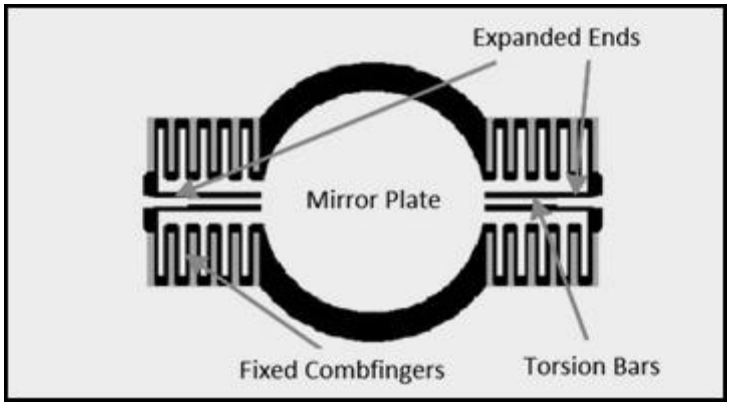

Figure 1.1 Schematic view of a comb-driven micromirror [11]

In this thesis, we focus our study on mechanical issues related to a type of micromirrors which use combdrive electrostatic actuation. An example of these micromirrors can be seen in Figure 1.1. These micromirrors are tilting resonant devices which, as their name indicates, employ electrostatic force for actuation. Operating in vacuum, the rotational mode of the system will be extremely excited, showing very high dynamic amplification within a short frequency band. This issue brings two deficiencies. First, spring bars which suspend the micromirror and store the elastic energy in oscillation, might fail due to high level of dynamic amplification. Second, controlling the device will need extensive accuracy of input voltage. Any small perturbation in the input leads to lose the resonance of the system, which means unreliability of system's performance. The solution for these problems lays in operating the device in ambient air. It should be mentioned that some modifications have been carried out in recent years to enhance micromirrors operating in vacuum packaged [11]. But, due to the economical reasons and specific applications which require the micromirrors to operate in air, we keep account of air in the simulations.

Presence of air as a viscous medium introduces extra damping to our oscillatory system in the form of fluid-mechanical forces, which smooth the frequency response of the system. On the other hand, the presence of air evolves into new issues and complexity to analyze the micromirror, because of the fluid-structural

interaction (FSI). This interaction has specific behaviors at different scanning frequency ranges, which are required for higher resolution levels like High-Definition (HD) and Full HD standard [29]. This fact brightly shows the need of correct and detailed understanding of these oscillatory systems.

To see the air presence effects on the natural frequencies and harmonic response of a micromirror, FSI effects should be accounted for. An acoustic-structural coupling technique is used to simulate the micromirror in this thesis. This FSI simulation employs structural element along acoustic ones. Thus, introducing a consistent matrix coupling set up between structural and acoustic elements, harmonic simulation of desired peak response within one single frequency step is performed very efficiently. By considering the fluid pressure only, the influence of fluid viscosity or shear layers is neglected in this method, meaning an ideal gas assumption.

At next step, we study the fluid-mechanical damping sources which are not considered in the previous simulations. These damping mechanisms are in charge of system energy dissipation and lowering quality factor of the micromirror. Two dominant mechanisms are the squeeze film damping by drag forces and the shear force damping occurring in the gap distance between the combfingers. Any device oscillating in air, suffers from air drag damping; but in microscale applications, it can be magnified by an extra dissipation mechanism, so-called squeeze film damping. This happens when two plates are located parallel to each other with a gap distance and one or both of them move in the normal direction. In this document, this phenomenon is studied by numerical simulations and its importance is examined for the problem at hand.

In the thesis, we study combfinger damping in micromirrors in details. Some analytical models based on Navier-Stokes equations are derived for lateral oscillatory infinite plates, and shear driven flow between two plates is solved for two different configurations. Since the gap between the pair of combfingers is $3\ \mu m$, the model is furnished by using ordinary and first order slip boundary conditions. The flow formation, velocity profiles and damping admittance of air between two plates for different frequencies are achieved.

Due to finite size of combfingers and complex geometry, the analytical modeling cannot be employed for damping analysis of combfingers. Therefore, after validating our numerical tool by a simple geometry amenable of analytical modeling, we conduct a set of simulations of the damping between rotor and stator combfingers. Laterally moving and tilting combfingers are studied, and significant effect of geometrical parameters on damping forces are shown. Final goal of this work is achieving the total quality factor of the micromirror, and comparing the result with experimental data. Thus, the simulation is conducted with real test

parameters including large tilting angle, $\pm 12^{o}$. These large oscillations require constant remeshing in the fluid, so as to prevent mesh distortion.

By this study, we can see the transient solution of fluid field over all the domain and along a period of oscillation. This work is an inclusive tool and complementary step to investigate the fluid structural effects on micromirror vibrations.

The next chapters of this thesis are organized as follows.

Chapter 2 covers the introductions on MOEMS, micromirror's applications, actuation methods and a brief review of operational principles of micromirrors.

Chapter 3 focuses on the specific micromirror manufactured by STMicroelectronics, which has been studied in this thesis. First, modal analysis is conducted to derive different resonance modes and frequencies. Then FSI method for coupling fluid domain, as an acoustic fluid, and solid domain is described, and harmonic analysis of micromirror by the proposed FSI methodology is done. Later, the influence of manufacturing residual stresses is modeled to capture the effects on the natural frequencies by modal analysis.

Chapter 4 deals with fluid-structural damping mechanisms. The CFX commercial code has been adopted to simulate the damping physics. Squeeze film damping is defined, and CFX model capability is examined by a test case. Then the same is done for shear force damping accounting for both ordinary and slip boundary condition, by comparing numerical method results with an analytical solution. Next, compact model is derived in the frequency domain for laterally oscillating plates.

Chapter 5 consisted of numerical simulations by CFX for squeeze film, shear force and drag damping in the micromirror plate and the combfingers' gap. The geometry influence on energy dissipation is studied, and their importance is shown. Then, combfinger damping is simulated in large angle oscillations and the evolution of fluid-mechanical torque on micromirror in time is obtained. Finally, the quality factor of the micromirror is calculated.

Chapter 6 summarizes the analyses done in the thesis and the corresponding results are brought in brief. The possible enhancements, based on the present work, are proposed for future developments.

CHAPTER 2

Micromirrors

This chapter is a short review on micromirrors and their applications. Section 2.1 presents the most popular applications of micromirrors. Different methods for actuation are also covered in Section 2.2 with more details on the electrostatic actuation. Finally, the target micromirror produced by STMicroelectronics is introduced in Section 2.3.

2.1 Introduction to micromirrors

The term MEMS (Micro-electro-mechanical-systems) is assigned to a wide range of devices and systems consisted of an integration of mechanical elements and electrical circuits on a common silicon substrate through microfabrication technology. These miniaturized apparatuses have been developed in the past decades, starting from the 1990s, with the aid of integrated circuits (IC) fabrication processes. MEMS have found their own applications and augmented the new applied ideas, expanding the space of possible designs. To name just a few, some of the commercialized applications are listed here below:

- accelerometers
- inject printheads
- MEMS gyroscopes
- pressure sensors
- micropumps
- bioMEMS
- Micro-Opto-Electro-Mechanical Systems (MOEMS).

The last application mentioned above is the outcome of a combination of optics and MEMS, and it opened new horizons for light manipulation. Recent improvements made them a promising field which can enhance functional fields, such as display systems, telecommunications, optical lithography, micro-optical-positioning systems (MOPOS), spectroscopy, etc. Among these applications, here the focus is on resonant micromirrors which are widely used in tunable lasers [4], variable optical attenuators [5], optical switching [6-9], and displays [10].

These fields are appropriately commercialized and a brief overview over these applications is mentioned in the following.

2.1.1 Displays

This field is considered the most successful application of micromirrors in commercial disciplines. One of the first and most famous products introduced in display and imaging systems market was the Digital Light Processor (DLP) by Texas Instruments. This technology has utilized micromirrors, because of their fast scanning speeds and high scan angles, obtained with acceptable energy consumption. DLP is a MEMS chip with an array of about 1 million movable micromirrors that operate digitally (ON-OFF), instead of continuously scanning the image [12]. This technology has been later used in main display units of many projection displays. Figure 2.1 shows a standard mirror array for this purpose.

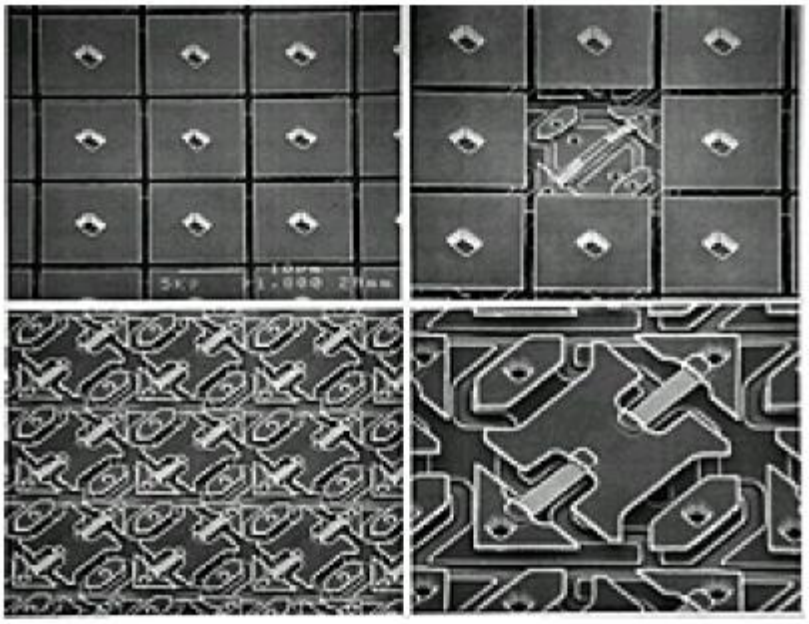

Figure 2.1 Texas instruments DLP, Mirror arrays and pixel structure [70]

Another successful application of MOEMS in display products has been the Retinal Scanning Display (RSD). This technology was developed by Microvision Inc. in the form of head mounted micro-display. It uses a single, two dimensional MEMS micromirror for scanning video data onto the retina of the user. It is a see-through display that simulates the displayed image onto what is actually seen by user. Despite of progresses achieved in design and manufacture of RSD, its performance critically depends on accuracy of the micromirrors design. This issue

has been well studied in some earlier researchers' works [13-14]. An example of RSD can be seen in Figure 2.2.

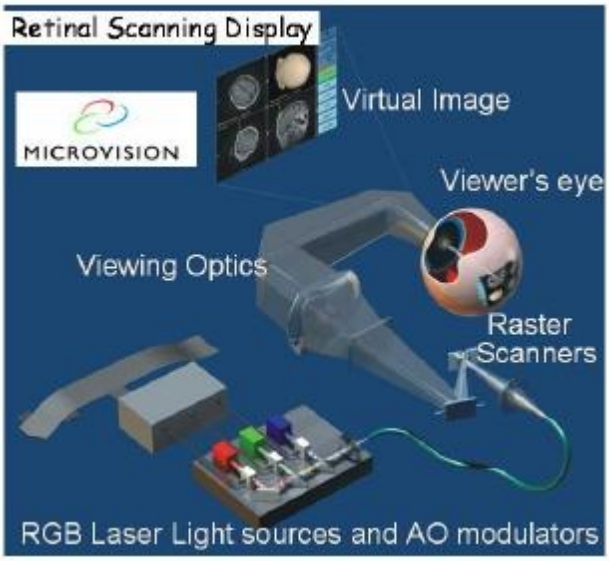

Figure 2.2 Retinal Scanning Display Technology by Microvision Inc, used a 2D MEMS micromirror [71]

In addition to the display applications mentioned above, micromirror technologies found their way through in imaging systems. Among different aspects of imaging applications, one of the most important is the barcode reading [15] which can be seen in Figure 2.3. Implementing micromirrors in 1D and 2D barcode readers offered high scanning frequency and lower power consumption in comparison to conventional technologies especially in compact hand held barcode readers. Micromirrors used in these devices are exposed to unpredicted high shock due to sudden fall or hits which can result in system malfunction.

Figure 2.3 Compact hand held barcode reader [72]

2.1.2 Optical switching

Another major application field of optical MEMS is the telecommunications industry. There has been an enormous interest and investment on fiber optic switching technologies during the exceptional growth of telecommunications market in the late 90's. However, since 2000 market conditions slowed down the progress in this area. Despite this drawback, optical MEMS are still a very attractive and promising technology for the telecommunications infrastructure of the future.

As a good tool for manipulating the direction of propagation of light, micromirrors play an important role in optical switching of fiber-optic data lines. Optical switching is significantly advantageous, since it allows optical routing of signals at nodes, without having to convert the signal into electrical state than back into optical signal, thereby maintaining high data bandwidths during transmission. Typical switching times for optical switches are in the order of few milliseconds.

There are many different applications that employ a stand-alone or an array of MEMS micromirrors. Single mirrors are generally used for routing in one-to-N fiber coupling, while array of mirrors are very suitable for optical cross connects (OXCs). Figure 2.4 shows a standalone micromirror designed for optical switching; Figure 2.5 describes two popular architectures for N-to-N fiber OXCs using micromirror arrays. There has been an enormous amount of research going on to develop fast, reliable and high capacity optical switching MEMS devices; a list of publications reporting some of the most successful devices for telecommunications applications can be found in [16].

Figure 2.4 A stand alone two-axis micromirror for optical switching applications [73]

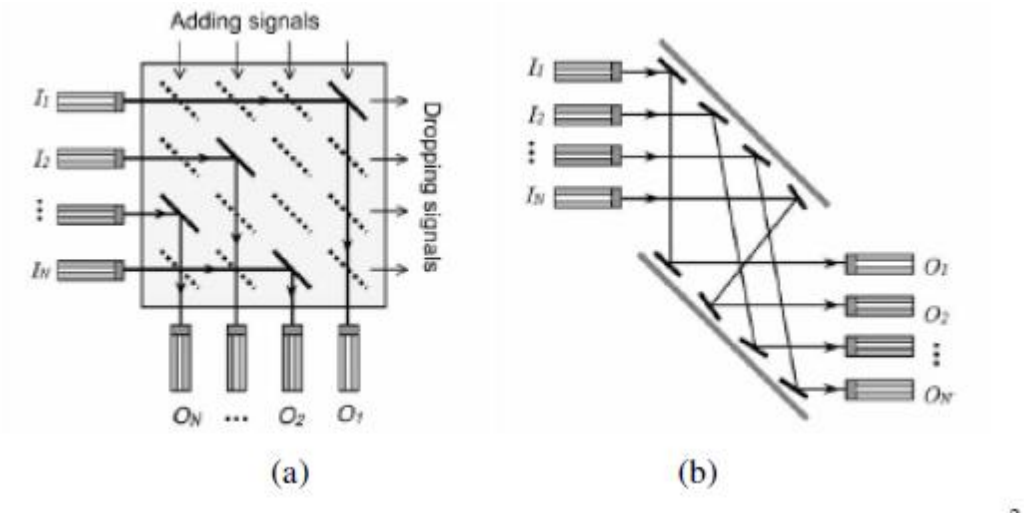

Figure 2.5 Two common structures for N-to-N OXC. (a) An N-to-N OXC with N2 mirrors. (b) An N-to-N OXC with 2N mirrors [17]

The applications of MOEMS and micromirrors are expanding. Here above, just a few of them are introduced, many others can be found in [18-20].

2.2 Actuation

Micromirrors can be considered as simple one-DOF (degree of freedom) or two-DOFs mechanical systems compounded of a mirror plate as mechanical mass and supporting silicon bars, holding the mirror and acting as springs to store the energy. Different kinds of actuation have been provided for MEMS applications, such as thermal actuation, electrostatic actuation, piezoelectric actuation, magnetic actuation and phase recover actuation using a shape memory alloy. All these methods need deposition of an extra layer on the silicon wafer surface but the electrostatic one. This electrostatic method is not functional in conventional mechanical systems, because it cannot exert enough force to displace or lift the mechanical components unless the introduced voltage is extremely high. By miniaturizing the mechanical systems at micro and nano scales, the magnitude of electrostatic forces turns relatively greater than inertial forces in comparison. Therefore, electrostatic driving method has found its own application in MEMS systems.

To have an overview on the different actuation methods, a short list of them has been brought; more detailed information on them can be found in the literature [22].

2.2.1 Electrostatic actuation

As it is obvious, the driving force is the electrostatic force between "positive" and "negative" charges. The fundamental of this force type is driven by Coulomb's law between two point charges. In engineering world, implementation of this law is based on the capacity variation of two capacitors; therefore, this method is also well-known as capacitive actuation.

In the simplest form, the concept can be shown by considering a system consisted of a battery and a capacitor of parallel plates. The plates are separated by a gap of width g, and free to move only along the lateral direction. An initial misalignment between parallel plates should be introduced to generate the electrostatic force. This misalignment causes an overlapping distance of X, which is much larger than the gap distance g.

The capacitance between the two plates is given by [74]:

$$C(X) = \frac{\varepsilon_0 W X}{g} \tag{2.1}$$

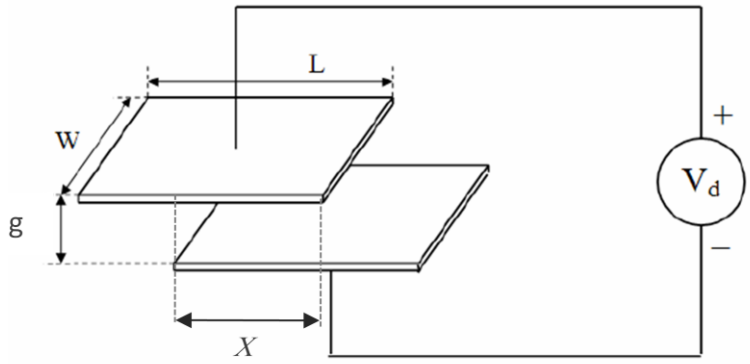

Figure 2.6 The electrostatic actuation by parallel plates [74]

where W (see Figure 2.6) is the width of plates and ε_0 is the permittivity of the medium between plates. When the plates are connected to a battery, whose voltage is V_d, the electric charge stores in the plates as:

$$Q = C(X)V_d \tag{2.2}$$

and the energy stored is expressed by:

$$E_c = \frac{1}{2}C(X)V_d^2. \tag{2.3}$$

Storing this energy in the capacitor, the battery energy is reduced to E_B

$$E_B = E_0 - Q_c V_d = E_0 - C(X)V_d^2 \tag{2.4}$$

and the total energy is:

$$E(x) = E_B + E_c = E_0 - \frac{1}{2}C(X)V_d^2 = E_0 - \frac{\varepsilon_0 WX}{2g}V_d^2 \tag{2.5}$$

where E_0 is the initial energy of the battery before connecting it to the capacitor. From the energy equation above, the lateral electrostatic force acting on the movable plate of the capacitor can then be derived as:

$$F_{el} = -\frac{\partial E(X)}{\partial x} = \frac{1}{2}\frac{dC(X)}{dx}V_d^2 = \frac{1}{2}\frac{\varepsilon_0 W}{2g}V_d^2 . \tag{2.6}$$

The negative sign in the equation indicates that the force tends to pull or push the plates in a way to maximize the overlapping distance X. To maximize the driving electrostatic force, we need to increase the total capacitance of the actuator plates. A good solution to this need is the combdrive layout, which increases the plates' surface. Figure 2.7 shows the basics of this actuation.

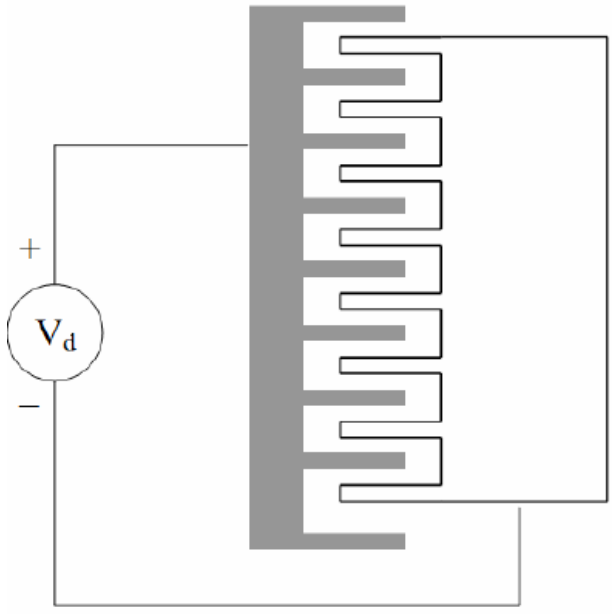

Figure 2.7 Basic Comb-drive actuation [74]

Combdrive actuators make use of electrostatic forces to move the resonator. Nevertheless, the normal forces between the capacitor plates should not be ignored. This force tends to move the pair of combfingers toward each other and in case of contact, a short circuit happens. This instability is called pull-in and to prevent it at operational magnitude of voltage, the spring stiffness should designed in a way to stop combfingers motion toward each other.

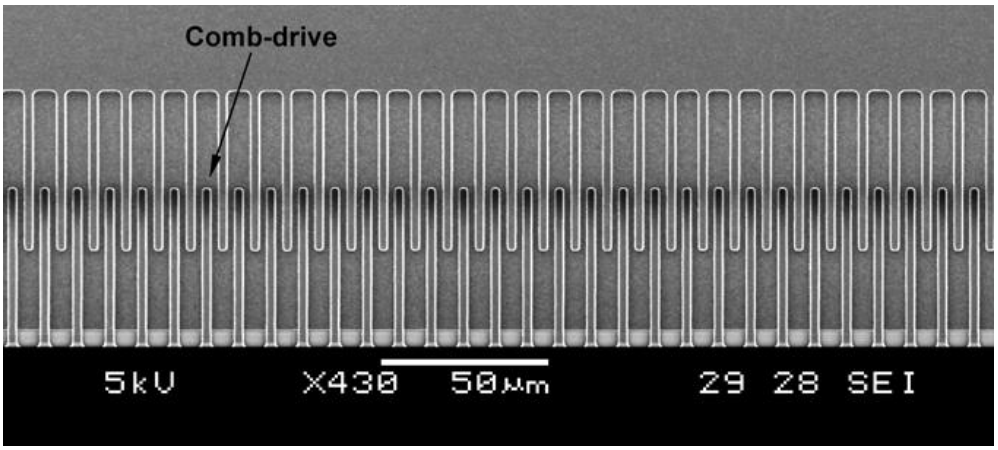

Figure 2.8 SEM image of two micromirrors and corresponding combfingers [21]

2.2.2 Electromagnetic actuation

This actuation technique can be carried out in various methods [22]. Usually, the actuation is achieved by utilizing Lorentz force imposed on a current carrying conductor located in a magnetic field. This force is dependent on the intensity of the current in the conductor, on the magnetic field intensity and on the length of the conductor which is located inside the magnetic field.

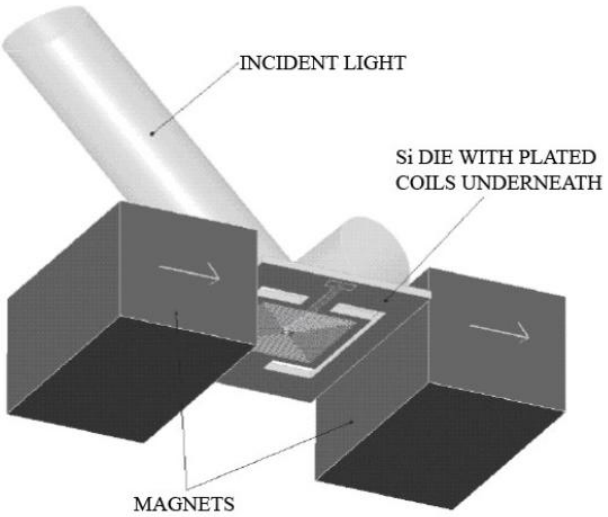

Figure 2.8 A basic one-dimensional electromagnetic micromirror [77]

Figure 2.8 shows a simple layout of a typical electromagnetic micromirror, in which the magnetic field is created by the side permanent magnets. Current passes through the coils located on the tilting mirror plate and in-plane electromagnetic forces exerted on the mirror result in a torsional deflection. In this method, a high current or a big magnetic field is required to increase the driving torque.

The other actuation methods are not common, including applying force to the magnetic material attached to the mirror by moving permanent magnet actuators [23] or permalloy actuators [24].

2.2.3 Thermal actuation

Several works have been done on using thermal actuation for micromirrors [25-26]. This method is based on the thermal expansion effect and on differences of the expansion coefficient in different materials. Two different materials are put together as a bimorph structure, such as a cantilever or a plate, and a temperature change bends this structure. The advantage of this method is simplicity of manufacturing. In general, thermal actuation tends to consume more power than the other actuation methods, with slow response time and high sensitivity to thermal noise. Another problem to be mentioned is the nonlinear response due to the temperature dependent properties of the materials [27].

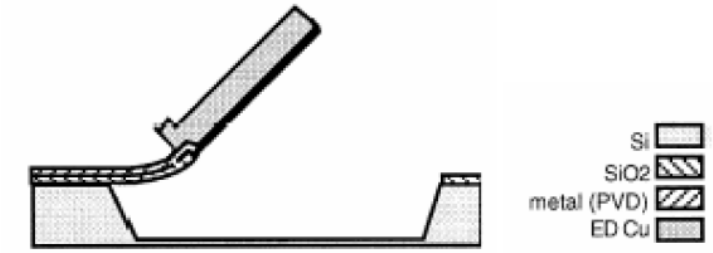

Figure 2.9 Cross section of a thermal actuation micromirror. The cantilever beam holding the mirror is a bimorph structure by two materials with different thermal expansion coefficient. Heating or cooling of the device actuates the mirror [25]

2.2.4 Piezoelectric actuation

Some crystalline materials will be compressed, twisted or distorted by applying a voltage charge. Piezoelectric actuation makes use of this behavior. This method benefits from high precision motion, linearity and fast switching time to 0.1 milliseconds, however, it needs high voltage for small deflections. There are

several successful application examples of this actuation for micromirrors, which took advantage of high mechanical gain and good performances [28-29]. Figure 2.10 shows a micromirror using piezoelectric actuation.

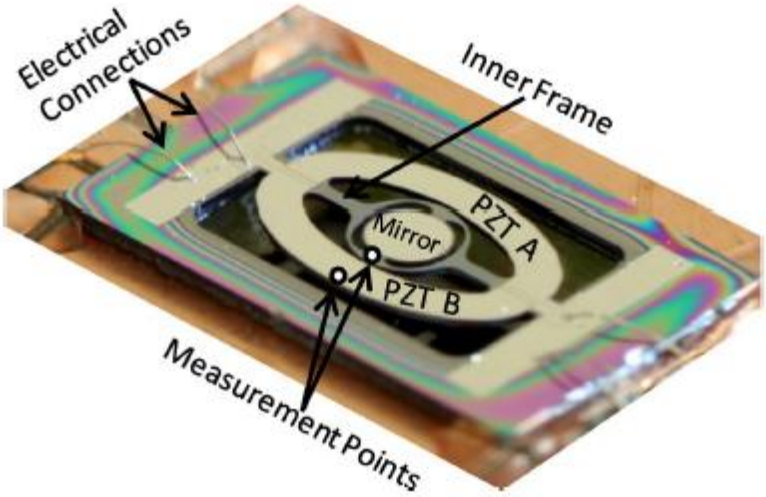

Figure 2.10 micromirror with piezoelectric actuation method [30]

In the end, a summary of advantages and disadvantages of each actuation method can be presented as in Table 2.1.

Actuation	Advantages	Disadvantages
Magnetic	- Low actuation voltage - Relatively large angular deflection with lower driving power	- Difficult to assemble permanent magnets and coils with current CMOS technology - Challenge in minimizing the size of device
Piezoelectric	- Higher switching speed - Low power consumption	- Short actuation range
Thermal	Ease of fabrication (require only one composite beam) for bulk production	- High power consumption - Slow response time - Fatigue due to thermal cycle
Electrostatic	- Low power consumption - Fast switching - Ease of integration and testing with electrical control circuitry	- Nonlinear characteristics - Limited by the pull-in effect - High actuation voltage - Fabrication complexity

Table 2.1 Summary of advantages and disadvantages of each actuation mechanism [22]

2.3 Reference micromirror

In this thesis, we focus on the micromirrors fabricated e.g. by STMicroelectronics. For sake of conciseness, we introduce here one of the models as the reference, see Figure 2.11. From now on we focus only on this micromirror. The micromirror movable structure is made of single crystal silicon, and consisted of a mirrorplate, torsional beams (suspending springs) and combdrive actuators (combfingers). The scanning frequency of this model is in range of 20 kHz, which gives a resolution in Video-Graphics-Array (VGA) standard.

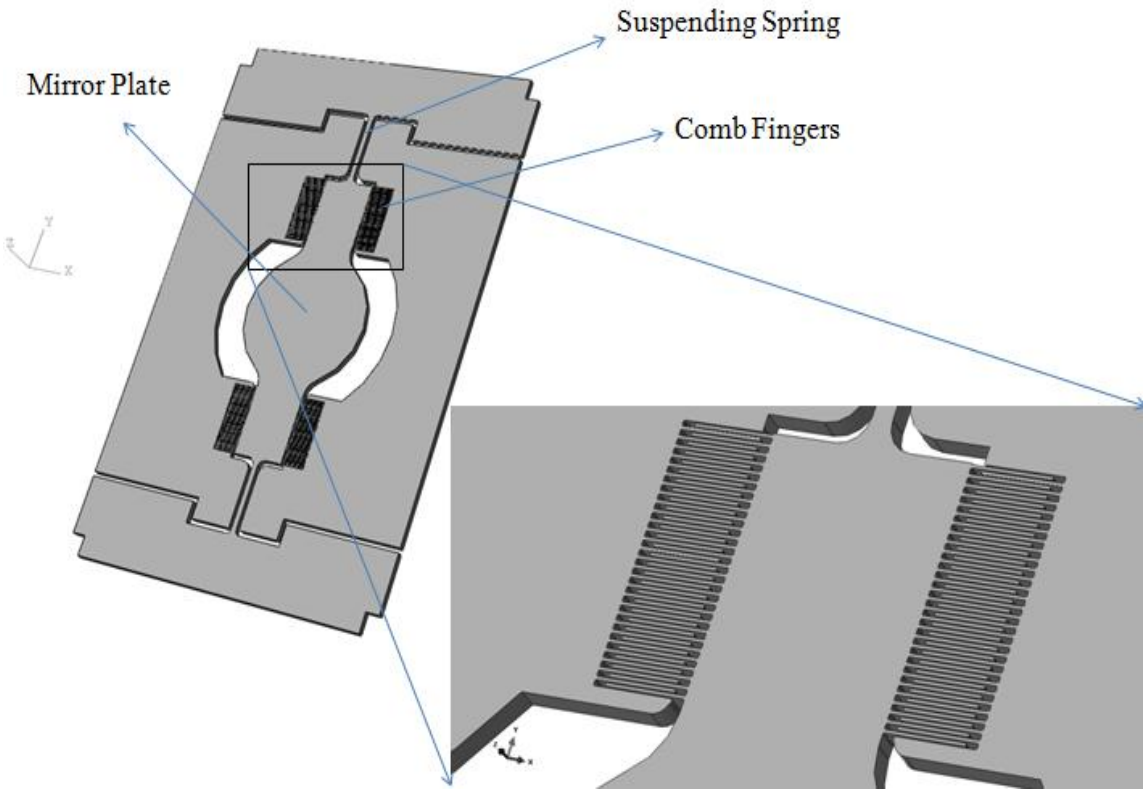

Figure 2.11 The general layout of the micromirror fabricated by STMicroelectronics.

The functional key element of the micromirror is the resonating mirror in torsional mode. The micromirror is suspended by two beams acting like springs for storing elastic energy, while resonating. Therefore, we aim having low stiffness of springs in torsional mode, and high stiffness as for the other degrees of freedom (axial and flexural ones). As mentioned before, the mirror is supposed to resonate in the torsional mode, but it is also possible to excite other modes. To prevent excitation of other modes, such modes should be separated enough in the frequency spectrum. This should be carried out by deigning the geometrical parameters of springs and mirrorplate. The actuation principle is based on the capacitance change in the combdrives; therefore, a slight difference between the mechanical and electrical rest positions is required to start the oscillations from the stationary position. As the required asymmetry is so slight, even process variations in microfabrication are enough to start the oscillations. The electrostatic force (torque) will be imposed on moving combfingers and tends to pull them to the equilibrium position in order to increase the overlap area of capacitors.

Having been introduced to basics of micromirrors and actuation methods in this chapter, we focus next on specific details of the selected micromirror in Chapter 3 to run the simulations.

Chapter 3

Operational and structural properties of micromirrors

In this chapter, the vibration modes of the reference micromirror are studied. Natural frequencies are derived in Section 3.1, and the mass effect of the surrounding air is considered for harmonics analysis in Sections 3.2 and 3.3. Also the residual stresses in the micromirror made by fabrication process are modeled in Section 3.4, to get their effect on the obtained torsional frequency.

3.1 Modal analysis and natural frequency modes

Modal analysis, to derive the natural frequencies of vibration and the relevant mode shapes, is one of the main steps in all dynamic analyses. By observing experiments on the micromirror, we recognized that the operational frequency is actually exciting the second mode of vibration. To conduct this numerical analysis by FEM (Finite Element Method), we adopted the ANSYS Mechanical APDL commercial code. By modeling the geometry of the micromirror and constraining the anchors displacements, the eigenvectors and eigenvalues of the system are first extracted disregarding the damping. It means ignoring structural damping, acoustic radiation and fluid damping.

Being the micromirror a type of resonator, its working resonance frequency and mode shapes are important issues to study. While designing the micromirror, special care should be considered to separate resonating frequencies, otherwise besides the torsional one, other modes can be excited. Measurements have shown that the working mode of this micromirror is the 2^{nd} one, whose frequency is $19{,}343$ Hz. FEM simulation is carried out, and different modes have been extracted, among which only the first one is close to the torsional mode. The geometrical data of the selected micromirror are provided in Table 3.1. Material parameters adopted in the analysis are the Young's modulus of 160 GPa, Poisson ratio of 0.23 and density of 2.33 $\mathrm{gr/cm^3}$. It should be noted, due to the symmetric geometry, only half of micromirror has been modeled with symmetry boundary condition along the midplane.

Parameter	Symbol	Value
Mirror Diameter	D	1,060 μm
Spring Length(considering fillets)	L_s	579.5 μm
Spring Width	W_s	44 μm
Finger Length	L_f	170 μm
Finger Width	W_f	6 μm
Finger Span (tip to tip)		760 μm
Finger Gap	G	3 μm
Number of Fingers on each actuator		29
Thickness of layout	t	50 μm

Table 3.1 Dimensions of the reference micromirror

Figure 3.1 illustrates the first five modes of the micromirror by contour plot of their displacement vector sum (blue stands for minimum value and red stands for maximum value). As it can be seen, the first and third modes are bending ones, the fourth and fifth are rocking modes, and the second mode is the working torsional mode.

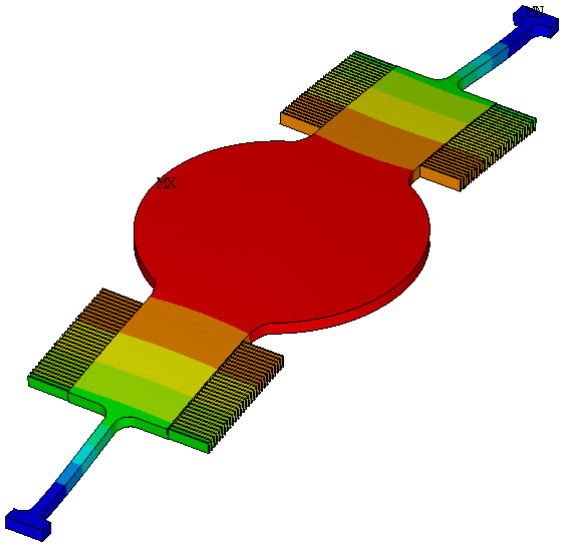

Mode 1 (Out of plane Bending)

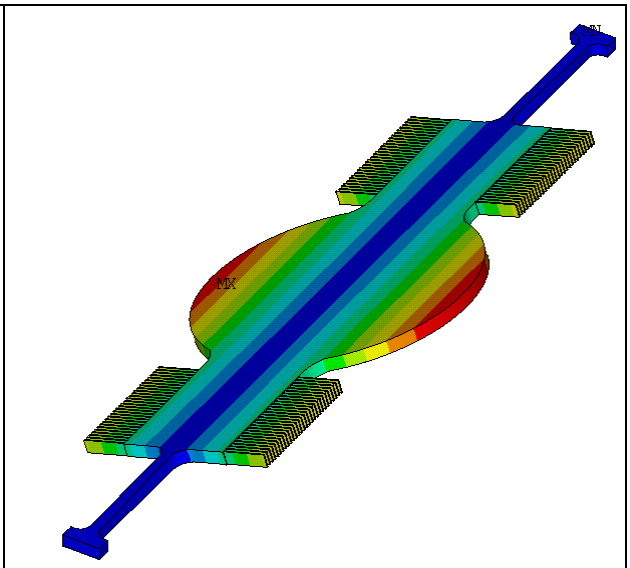

Mode 2 (Torsion)

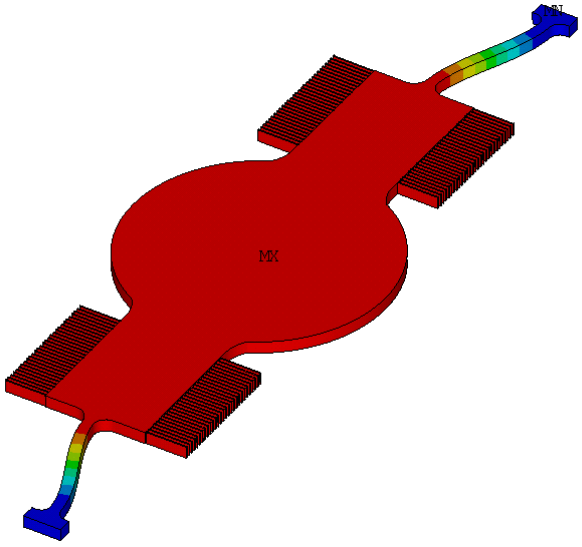

Mode 3 (In plane Bending)

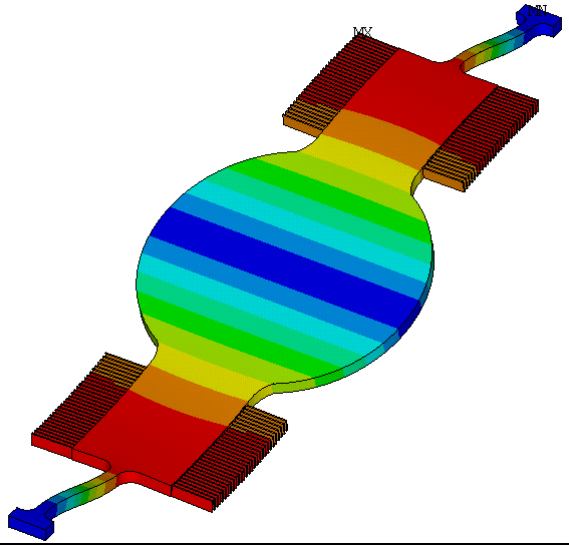

Mode 4 (Out of plane Rocking)

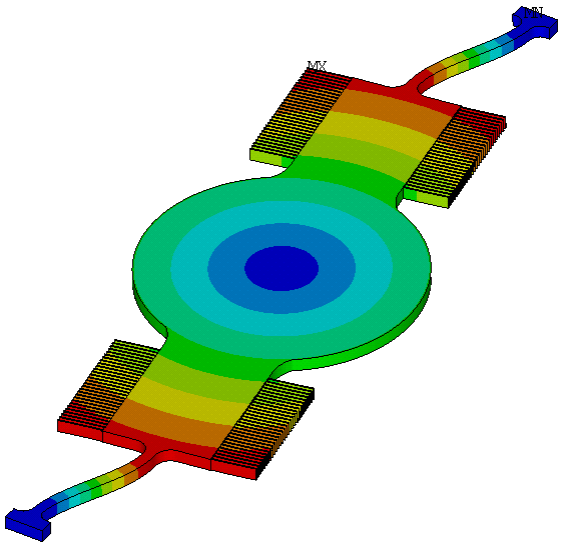

Mode 5 (In plane Rocking)

Figure 3.1 First five fundamental modes of vibration

Mesh size is a crucial factor for the accuracy of eigenvalues in FEM modal analysis especially when torsional vibrations are to be modeled. Considering this point, the analysis has been run using 4 different mesh sizes. As it is expected, decreasing the mesh size, we can settle the results to an asymptotic solution for eigenvalue.

Mesh global size (micron)	1st mode (kHz)	2nd mode (kHz)
30	19.79	22.45
15	19.33	20.99
7.5	19.21	20.56
3.75	19.18	20.35

Table 3.2 First two vibration modes frequencies obtained by different mesh sizes

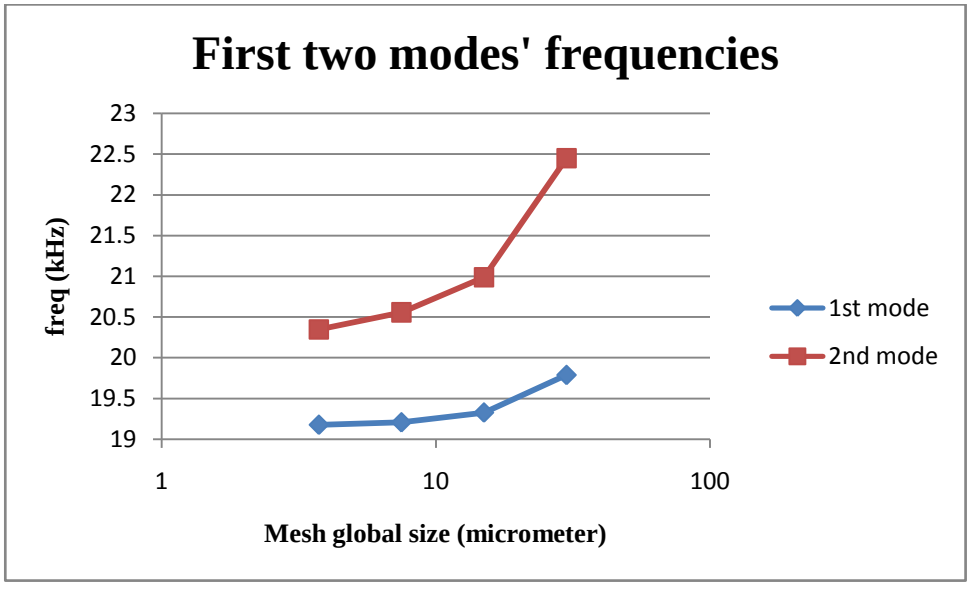

Figure 3.2 Dependence on mesh size of natural frequency of vibration

The difference between experimental data and results of the numerical simulation concerning working natural frequency can be in result of several factors. The uncertainty in geometry dimensions is one of the reasons that always exists at this length scale. The other one can be the difference between actual material properties and what has been input in the simulation. Beside all these issues, one should notice that main assumption in modal analysis is the approximate way to address the damping phenomena and neglecting nonlinearity due to electrostatic excitation (which have a decreasing effect in natural frequency [38]). Last but not

least, additional mass-type effect of air as an acoustic fluid should be noticed which we study in detail in subsequent sections by introducing a fluid-structural interaction (FSI) technique to couple acoustic and structural fields.

3.2 Acoustic fluid effect on natural frequencies of structure

In the next step, the acoustic fluid surrounding the structure has been modeled. This interaction between fluid and structure, through the acoustic pressure causes a force on the structure and reciprocally the structure motion produces loading on the fluid domain. These issues in the fluid structure interaction problems require the mechanical dynamic equations be solved, along with the Navier-Stokes equations of fluid momentum and fluid continuity [30]. Simplifying the Navier-Stokes and continuity equations, Kinsler derived the formulation of acoustic wave through the following assumptions [31]:

- the fluid is compressible (density changes due the pressure variations);
- the fluid viscosity is ignored (no viscous dissipation);
- there is no mean fluid flow (average flow of gas on domain's boundaries);
- mean density and pressure are uniform throughout the fluid.

These assumptions yield the acoustic wave equation as follows:

$$\frac{1}{c_s^2}\frac{\partial^2 P}{\partial t^2} - \nabla^2 P = 0 \tag{3.1}$$

where t is time, P is the acoustic pressure variable in time and space, $P = P(x, y, z, t)$ and c_s is the sound speed in fluid medium which is correlated with density through $c = \sqrt{K/\rho_f}$ in which ρ_f is the mean density of fluid in the domain and K is the bulk modulus of fluid. ∇^2 is the Laplace operator

Introducing the following matrix operators on the above equation the wave equation can be rewritten.

$$\nabla.(\,) = \{L\}^T = \left[\frac{\partial}{\partial x}\frac{\partial}{\partial y}\frac{\partial}{\partial z}\right] \tag{3.2}$$

$$\frac{1}{c_s^2}\frac{\partial^2 P}{\partial t^2} - \nabla.\nabla P = 0 \tag{3.3}$$

$$\frac{1}{c_s^2}\frac{\partial^2 P}{\partial t^2} - \{L\}^T(\{L\}P) = 0. \tag{3.4}$$

Element matrices can be derived using the Galerkin procedure [32]. By multiplication of virtual pressure variation into wave equation and by integration over the domain volume, it yields:

$$\int_{\mathrm{V}} \frac{1}{\mathrm{c}_s^2}\delta P \frac{\partial^2 P}{\partial t^2} d\mathrm{V} + \int_{\mathrm{V}} (\{L\}^T \delta P)(\{L\}P) d\mathrm{V} = \int_S \{n\}^T \delta P(\{L\}P)\, d(S) \tag{3.5}$$

where V represents the volume domain, δP is the virtual change in pressure $\delta P = \delta P(x, y, z, t)$, S is the interface of fluid and structure where the virtual derivatives of pressure normal to surface are applied (the natural boundary condition), and $\{n\}$ is the unit normal to the interface S.

Considering the assumptions already made, the momentum equation for the fluid can result in the following relationship between the normal pressure gradient in the fluid and the normal acceleration of the structure at the boundary of solid and fluid interface S:

$$\{n\}.\{\nabla P\} = -\rho_f \{n\}.\frac{\partial^2 \{\bar{u}\}}{\partial t^2} \tag{3.6}$$

$$\{n\}^T \{\{\mathrm{L}\}P\} = -\rho_f \{n\}^T \left(\frac{\partial^2}{\partial t^2}\{\bar{u}\}\right) \tag{3.7}$$

where $\{\bar{u}\}$ is the displacement vector of the structure at the interface with the fluid domain. After substituting the last equation in Equation (3.5), the outcome is:

$$\int_{\mathrm{V}} \frac{1}{\mathrm{c}_s^2}\delta P \frac{\partial^2 P}{\partial t^2} d\mathrm{V} + \int_{\mathrm{V}} (\{L\}^T \delta P)(\{L\}P) d\mathrm{V} = -\int_S \rho_f \delta P \{n\}^T \left(\frac{\partial^2}{\partial t^2}\{\bar{u}\}\right) d(S). \tag{3.8}$$

This equation contains the fluid pressure and the structural displacement components of $\{\bar{u}\}$ as dependent variables to solve. By introducing the shape functions for spatial variations, the spatial discretization of the problem gives:

$$P = \{N\}^T \{P_e\} \tag{3.9}$$

$$\bar{u} = \{N'\}^T \{\bar{u}_e\} \tag{3.10}$$

where $\{N\}$ is the shape function for pressure related to element type, $\{N'\}$ is the shape function for structural displacement related to element type, $\{P_e\}$ is the nodal pressure vector, and nodal displacement components vector are $\{\bar{u}_e\} = \{\bar{u}_{xe}\ \bar{u}_{ye}\ \bar{u}_{ze}\}$.

Second time derivatives of the variables and virtual pressure variation can be written as:

$$\frac{\partial^2 P}{\partial t^2} = \{N\}^T\{\ddot{P}_e\} \tag{3.11}$$

$$\frac{\partial^2}{\partial t^2}\{\bar{u}\} = \{N'\}^T\{\ddot{\bar{u}}_e\} \tag{3.12}$$

$$\delta P = \{N\}^T\{\delta P_e\}. \tag{3.13}$$

The matrix operator of $\{L\}$ can be applied on the element shape function $\{N\}$ and yields:

$$\{B\} = \{L\}\{N\}^T. \tag{3.14}$$

Finally, the finite element statement of the acoustic wave problem can be expressed as:

$$\int_{\mathrm{V}} \frac{1}{\mathrm{c_s^2}}\{\delta P_e\}^T\{N\}\{N\}^T d\mathrm{V}\{\ddot{P}_e\} + \int_{\mathrm{V}} \{\delta P\}^T[B]^T[B]d\mathrm{V}\{P_e\} + \int_S \rho_f\{\delta P\}^T\{N\}\{N\}^T\{N'\}^T\, d(S)\{\ddot{\bar{u}}_e\} = \{0\}. \tag{3.15}$$

Some terms which do not vary over element are taken out of integration sign and the virtual change in pressure, $\{\delta P_e\}$, will be crossed out; henceforth, we have:

$$\frac{1}{\mathrm{c_s^2}}\int_{\mathrm{V}} \{N\}\{N\}^T d\mathrm{V}\{\ddot{P}_e\} + \int_{\mathrm{V}} [B]^T[B]d\mathrm{V}\{P_e\} + \rho_o \int_S \{N\}\{N\}^T\{N'\}^T\, d(S)\{\ddot{\bar{u}}_e\} = \{0\}. \tag{3.16}$$

Now the above equation can be written in matrix notation to get the discretized wave equation:

$$[M_e^P]\{\ddot{P}_e\} + [K_e^P]\{P_e\} + \rho_o[R_e]^T\{\ddot{u}_e\} = \{0\} \tag{3.17}$$

where the fluid mass matrix, the fluid stiffness matrix and the coupon mass matrix in fluid-structure interface, are respectively:

$$[M_e^P] = \frac{1}{c_s^2}\int_V \{N\}\{N\}^T dV \tag{3.18}$$

$$[K_e^P] = \int_V \{\delta P\}^T[B]^T[B]dV \tag{3.19}$$

$$\rho_f[R_e] = \rho_f \int_S \{N\}\{N\}^T\{N'\}^T\, d(S)\,. \tag{3.20}$$

As already mentioned, on the interface the fluid exerts a pressure load on the structure. Adding the fluid pressure load acting at the interface to dynamic equilibrium equation for a linear system with an arbitrary external load, F_e, we can completely describe the fluid-structure interaction problem. To this issue, the structural equation is rewritten here:

$$[M_e]\{\ddot{\bar{u}}_e\} + [K_e]\{\bar{u}_e\} = \{F_e\} + \{F_e^{pr}\} \tag{3.21}$$

The fluid pressure load can be obtained by integrating the pressure over the area of the interface S. This expression can be written as below:

$$\{F_e^{pr}\} = \int_S \{N'\}P\{n\}d(S) \tag{3.22}$$

and, substituting the finite element approximating function for pressure given by the Equation (3.9) into the Equation (3.16):

$$\{F_e^{pr}\} = \int_S \{N'\}\{N\}^T\{n\}d(S)\{P_o\}\,. \tag{3.23}$$

Comparing the definition of the coupling matrix of the fluid-structure interface with the above integration, one obtained:

$$\{F_e^{pr}\} = [R_e]\{P_e\} \tag{3.24}$$

where:

$$[R_e] = \int_S \{N'\}\{N\}^T\{n\}d(S)\,. \tag{3.25}$$

Substitution of the last equation into the dynamic elemental equation of structure, gives:

$$[M_e]\{\ddot{\bar{u}}_e\} + [K_e]\{\bar{u}_e\} - [R_e]\{P_e\} = \{F_e\}. \tag{3.26}$$

To have a complete description of the system in presence of fluid-solid interface, we can assemble two elemental dynamic equations of solid and fluid in the form of:

$$\begin{bmatrix} [M_e] & [0] \\ [M^{fs}] & [M_e^P] \end{bmatrix} \begin{Bmatrix} \{\ddot{\bar{u}}_e\} \\ \{\ddot{P}_e\} \end{Bmatrix} + \begin{bmatrix} [K_e] & [K^{fs}] \\ [0] & [K_e^P] \end{bmatrix} \begin{Bmatrix} \{\bar{u}_e\} \\ \{P_e\} \end{Bmatrix} = \begin{Bmatrix} \{F_e\} \\ \{0\} \end{Bmatrix} \tag{3.27}$$

where the two coupling sub-matrices of fluid-solid interaction are:

$$[M^{fs}] = \rho_f [R_e]^T \tag{3.28}$$

and

$$[K^{fs}] = -[R_e]. \tag{3.29}$$

Through these equations, the structural field and the fluid fields are coupled disregarding the dissipative effects and structural damping. It is worth to be noticed that the matrix system here is unsymmetrical, and during the analysis special care should be taken with the solution technique.

3.3 Harmonic response analysis along FSI

Cyclic loads are common in the engineering world and the response of dynamic systems to these types of loads is also cyclic or, in other words, "harmonic". To verify whether the structural system is able to overcome fatigue or other harmful outcomes of forced vibration, a harmonic response analysis might be conducted. Through harmonic response analysis, the steady state response of a system undergoing cyclic force is obtained. The transient phase of vibration, which occurs at the beginning of the excitation, cannot be obviously followed with this method.

Some important issues should be noticed about this analysis. The harmonic analysis is linear; non-linearities will be ignored. But it is capable of handling the

unsymmetric system of matrices like FSI problem described in previous section. The solution method for these systems of matrices are well defined in [33].

Here we have run a full harmonic response analysis in ANSYS Mechanical APDL. The same geometry as the modal analysis is imported in the work space, and a surrounding box of air is modeled as shown in Figure 3.3. Fixed boundary conditions (BCs) at the anchor, symmetry BCs at the midplane of the structure, and ambient pressure on the outer surface of air have been introduced. As a load needs to be imposed on the structure for the system excitation, it is important to only excite the desired mode of vibration which is the rotational one. Therefore, we used a pair of forces to induce a torque on the system. The fluid FSI boundary condition should be assigned to the nodes that are shared by air and solid having 4 DOFs (pressure and spatial displacement components). In this way, the pressure field and the structural displacements will be coupled. Thus as presented in previous section, a consistent matrix coupling is set up between structural and fluid elements. Consequently, simulation of the desired peak response within one single frequency step is performed very efficiently.

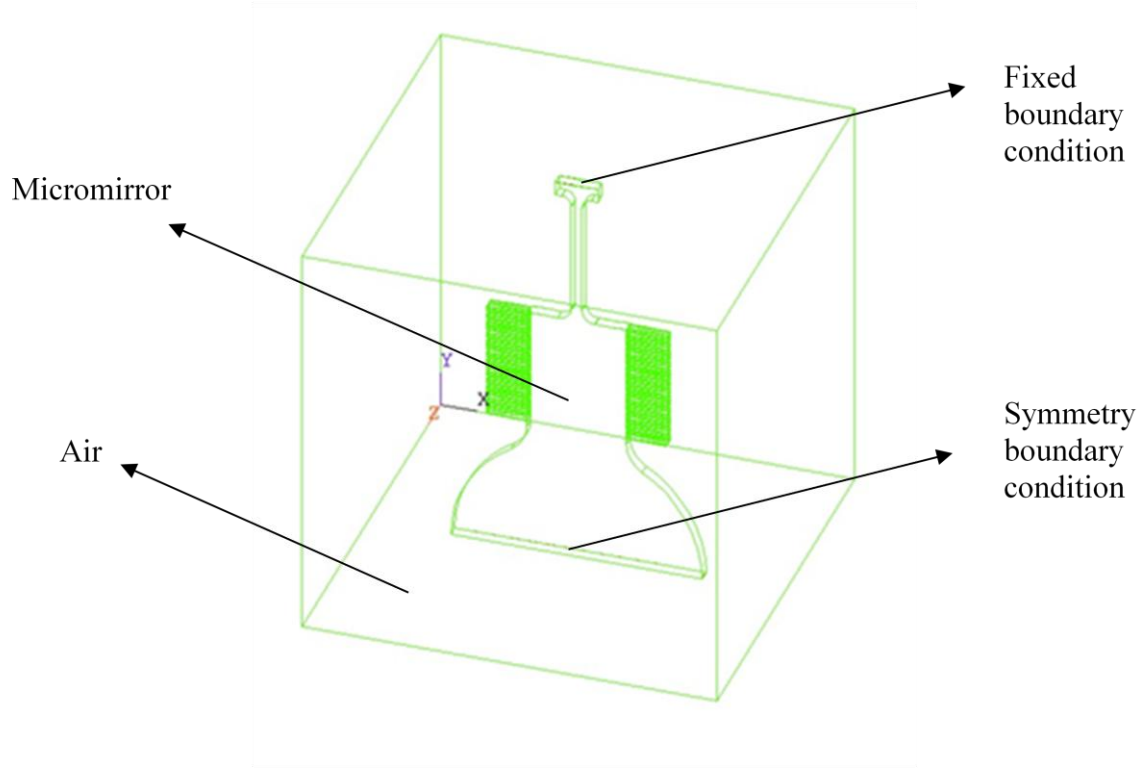

Figure 3.3 Micromirror inside the surrounding air

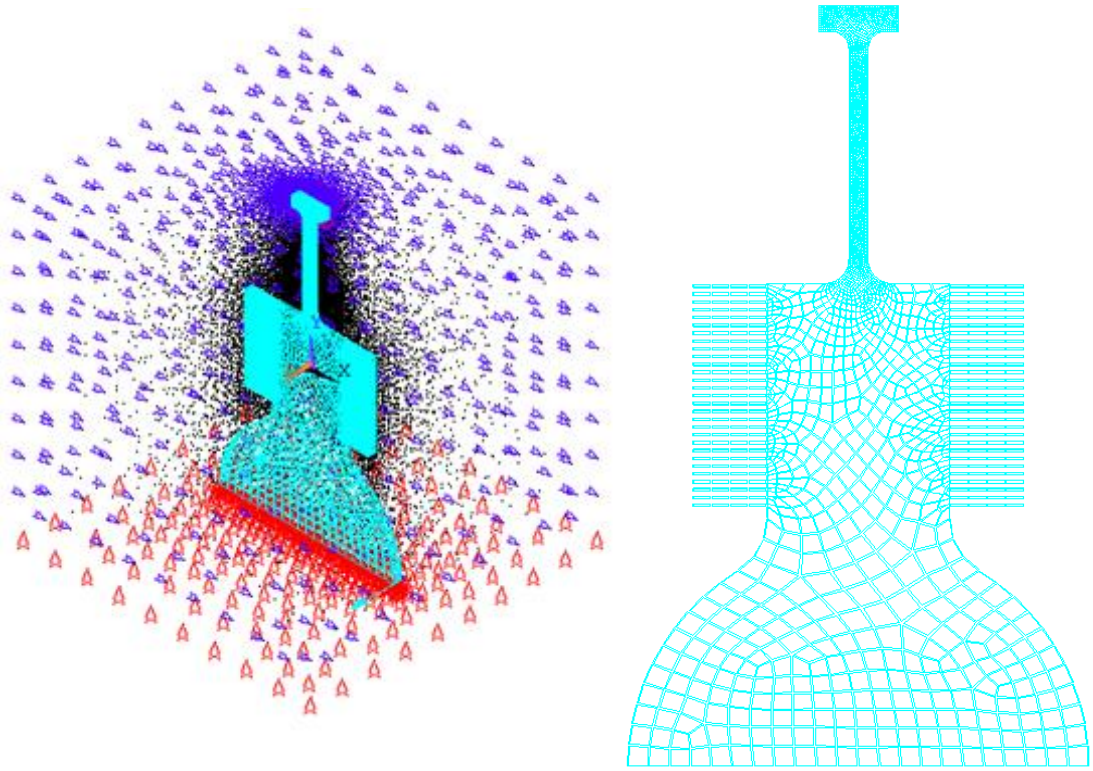

Figure 3.4 The micromirror mesh and the different boundary conditions applied to the system.

Figure 3.4 shows nodal BCs in the analysis and the aqua colored net around the micromirror shows the FSI BC on micromirror elements. The analysis parameters are summarized in Table 3.3:

	Property	Value
Micromirror	Elastic modulus-isotropic (GPa)	160
	Poisson ratio	0.23
	Density (kg/m3)	2,330
	Element type	SOLID45
Air	Density (kg/m3)	1.225
	Sonic Velocity (m/s)	343.2
	Element type	FLUID30

Table 3.3 Material characteristics used in analysis

Doing the analysis, the nodal displacement and stress fields are obtained in the frequency domain. Through following figures, we report the results in the form of our-of-plane displacement of one of the edge nodes on the midplane of micromirror versus sweep frequency. Due to the absence of damping effects, the

dynamic amplification should be infinite; and apparently we are not able to obtain infinity in numerical simulations

One of the analysis prerequisites is assigning the sweep frequency range of interest. So at first, the analysis is run over a wide frequency range with rough frequency discretization. Upon estimating the resonance frequency, harmonic response analysis has been repeated for frequencies near the estimated resonance with finer frequency discretization. By this procedure, we derive the accurate resonance frequency.

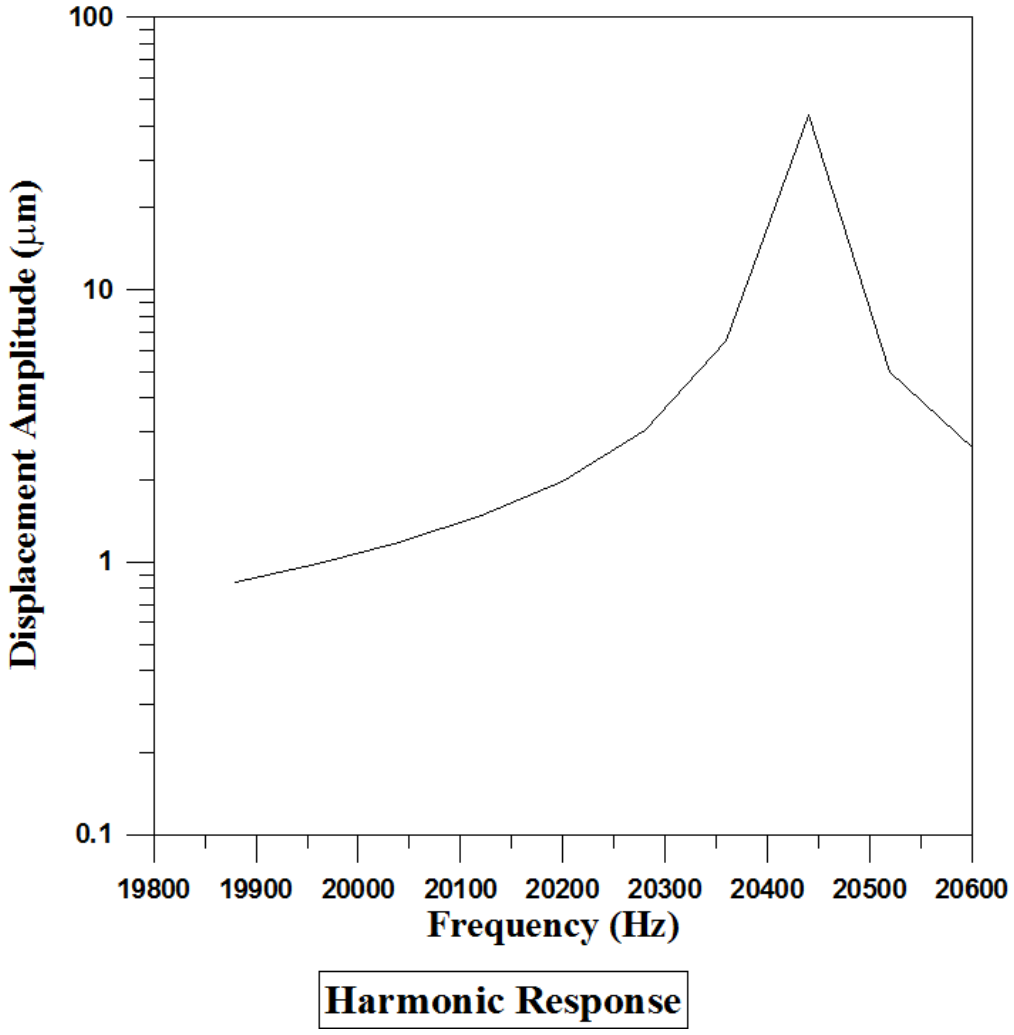

Figure 3.5 Rough harmonic response analysis to locate the resonance frequency range

Figure 3.5 shows the dynamic amplification in the vicinity of 20,450 Hz. By finer discretization of this frequency range of interest to 1 Hz, the steady state response corresponding to the same excitation is obtained in Figure 3.6.

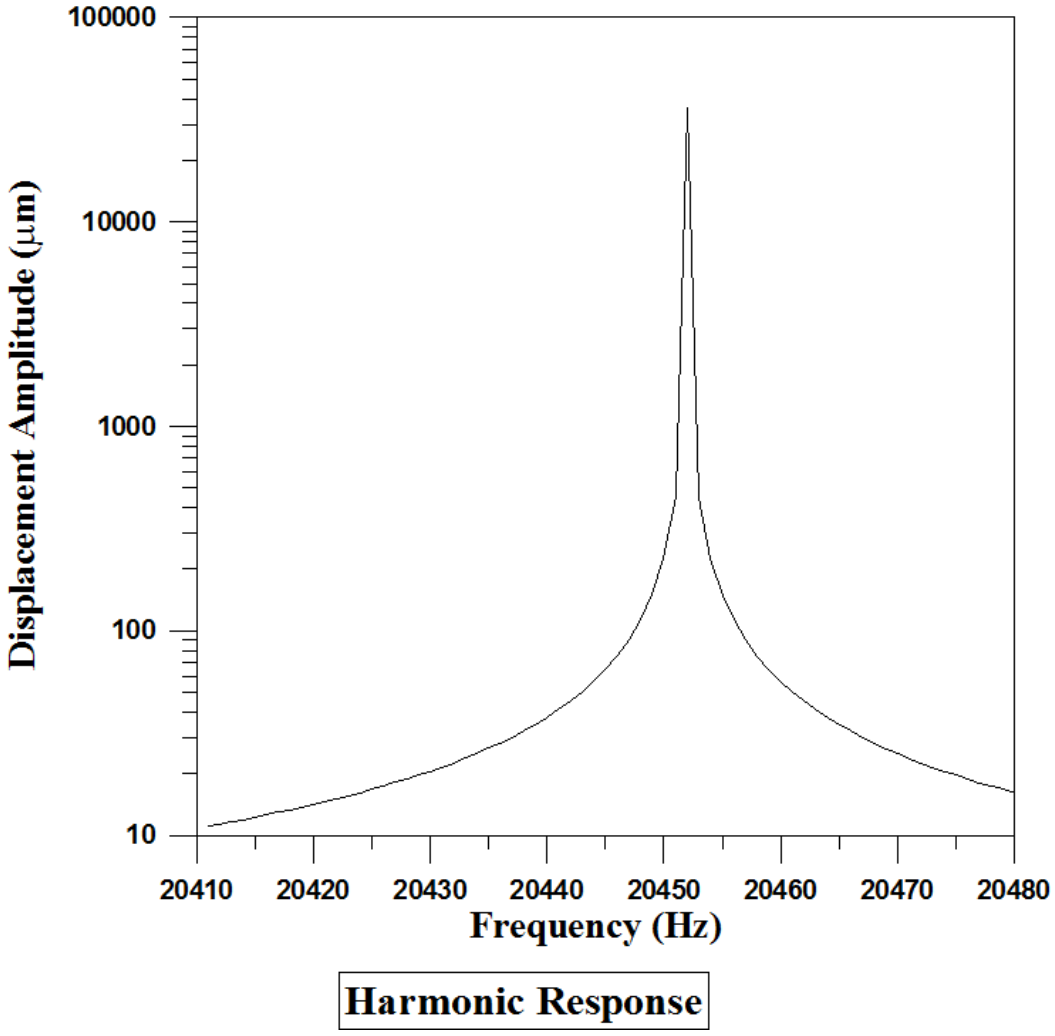

Figure 3.6 Harmonic response analysis with 1 Hz *accuracy, micromirror structure without surrounding air*

Figure 3.6 shows the response for structure vibration only and not the air effect on dynamics of the system. The microstructure used here has an average mesh size between 3.75 μm and 7.5μm so as it is shown above, the resonance frequency is 20,451 Hz. It was already shown in mesh sensitivity analysis, the 2nd natural frequency will change from 20,560 Hz to 20,350 Hz corresponding to mesh size changing of 7.5μm to 3.75 μm. We used this mesh size in harmonic analysis to have a reasonable time expense for analysis. Using very fine mesh in this analysis due to presence of the fluid elements leads to long time consuming analysis.

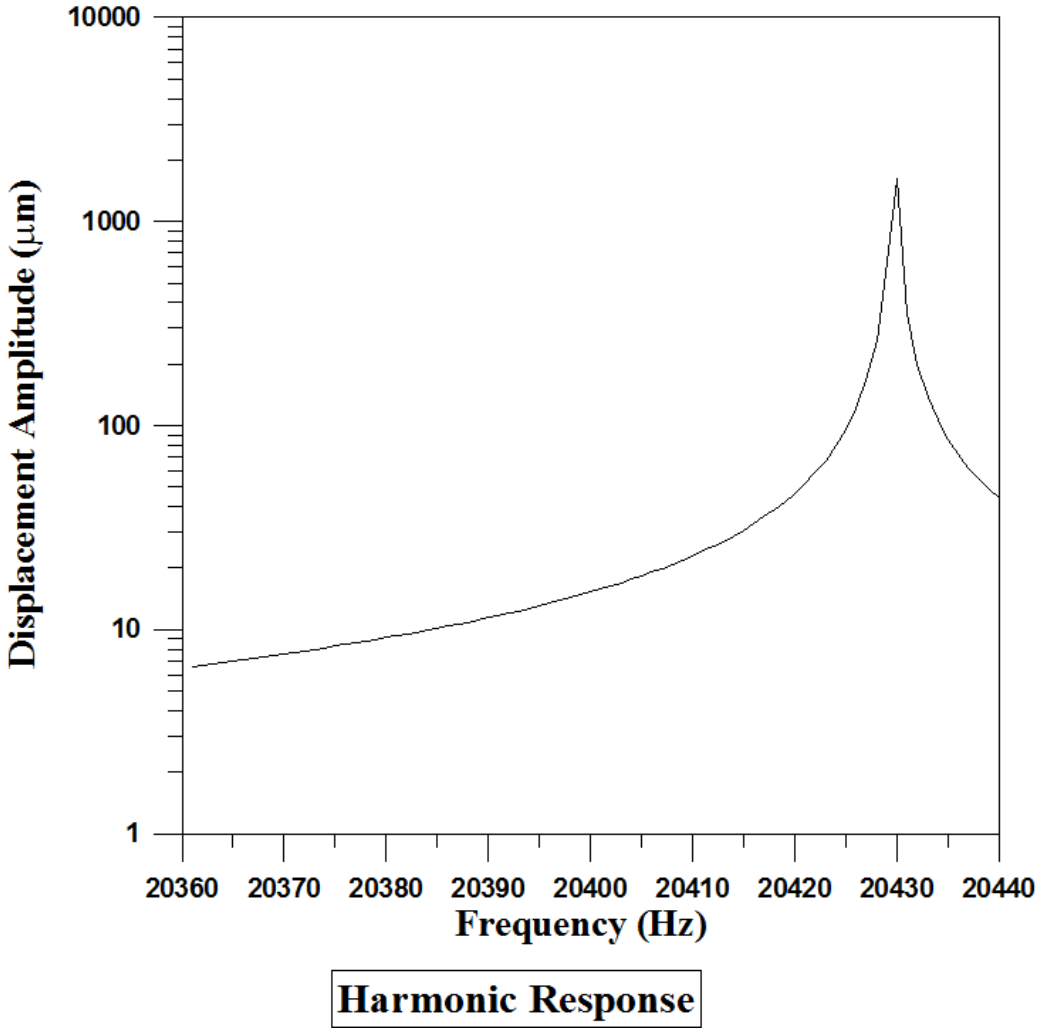

Figure 3.7 Harmonic Response analysis with 1 Hz *accuracy, micromirror structure with surrounding air*

In the Figure 3.7, the fluid elements are imported to the system and the harmonic response of coupled field of structure and fluid is achieved. It shows that the resonance happens in $20{,}429$ Hz which is lower than the structural natural frequency itself. This frequency shift due to existence of fluid even without considering the viscosity effects are shown in previous researches like as [34].

3.4 Prestressed modal analysis

One of the phenomena that may modify the dynamic response of the whole system is the presence of residual stress and/or residual strain gradient in the material. Residual stress/strain gradients are capable of changing the resonance frequency and the deformed shape. Almost any manufacturing process introduces residual stress gradients within the MEMS devices. Manufacturing parameters such as baths compositions, seed layer material properties, temperature and time deposition, etc. affect the final stress gradient [35]. These gradients are here defined as prestress for the structure.

In [36] and [37] the dynamic characteristics modification of structures under prestress load is discussed, showing that axial load or any load which may tend to cause buckling of a structure may have a significant effect on the bending stiffness of the structure itself. It is well shown that the bending frequencies are greatly affected by the magnitude of the prestress load in the structure, while the torsional mode frequency is not that much sensitive to prestressed condition.

The residual stress tends to bend the micromirror; this can be measured in some of the samples. This curvature observed to reach up to 0.1 μm at the middle of the micromirror. To capture the curvature in FEM modeling, researchers use an equivalent thermal loading on the structure (ignoring its influence on the elastic moduli of the material). The approach for calculation of the dynamic properties of the micromirror includes at first a static thermal analysis, to extract internal forces and resultant stress field (see Figure 4.8), and in second step, imposing this stress field as complementary BC for the final modal analysis. All these analyses should be conducted considering the nonlinear geometries effects.

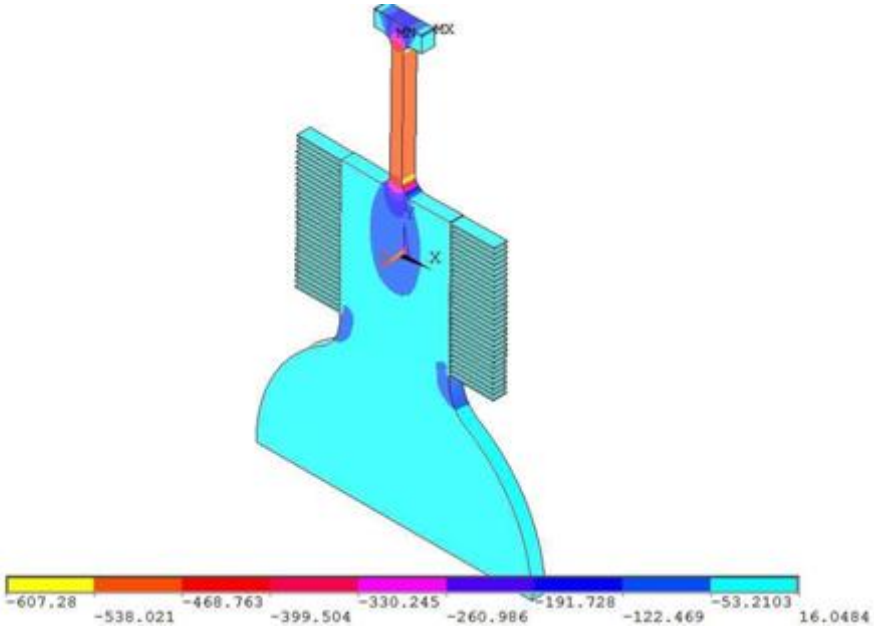

Figure 3.8 Longitudinal stress contour

The resonance frequencies of the first three modes are extracted for the stress free and prestressed condition and reported in Table 3.4. To save time in the analysis, a medium size mesh is used and therefore, the frequencies are higher than the exact solution presented before. This technique is an important step to ensure our capability to account for the prestress condition in modal analysis.

	1st mode	2nd mode	3rd mode
Stress free	18,914 Hz	20,456 Hz	33,641 Hz
Prestressed	7,466 Hz	20,370 Hz	22,494 Hz

Table 3.4 First three natural frequencies of vibration in the micromirror with stress free and prestressed condition

As shown in the Table 3.4, prestress presence changed the frequencies in different manners for the bending and torsional modes. With attention to the resonance vibration mode, which is bending for 1st and 3rd and torsional for 2nd one, it is worthwhile to emphasize that the bending modes are significantly influenced by axial load while the torsional mode shows less sensitivity. Therefore, we conclude that an insignificant role of this manufacturing made residual stress is played in working resonance mode.

In this chapter, we studied the natural frequency for torsional mode in details. FSI harmonic analysis has been adopted to check the acoustic effects of the surrounding air on the resonance frequency. Then, the residual stress influence has been modeled by a thermal loading. In the next chapter, we will study the damping mechanisms in micromirrors

.

Chapter 4

Damping in micromirrors

This chapter is dedicated to the study of damping mechanisms in the resonant micromirrors. After a short overview on the damping mechanisms in Section 4.1, squeeze film damping is briefly introduced, and the capability of our numerical tool to account for this mechanism is examined in Section 4.2. Then, we go into details of the damping mechanism occurring in combfingers in Section 4.3. Providing analytical approaches, the numerical tool is again tested. Finally, in Section 4.4 we study the shear driven flow between oscillatory infinite plates as a function of the oscillation frequency, adopting either stick or slip boundary conditions.

4.1 Introduction

In vibrating mechanical systems, damping plays an important role in modulating the response. Therefore, understanding the nature of damping is crucial to effectively control the system. In the world of MEMS applications, due to the dominance of surface forces (like damping ones) over body forces (like inertial ones), damping mechanism plays a more important role in system identification. For example, a too low damping in accelerometers, coupled to the resonance of the system upon an impact of external force, might produce such a large signal which causes system failure. High damping levels are instead not desired in yaw rate gyroscopic sensors; instead, low damping is needed to achieve sufficient sensitivity of the system under a given driving force [39].

The dominant damping mechanisms in MEMS devices like micromirrors is fluid-induced damping, rather than structural or radiation dissipation [40]. Fluid damping mostly happens in parallel moving plates. A gas layer between two closely spaced parallel plates, oscillating with a normal relative motion, generates a force, due to compression and internal friction opposing the motion of the plates. The damping, related to an energy loss of the system due to such forces is referred to as “squeeze film damping”. Another case occurs when two closely spaced parallel plates oscillating in a direction parallel to each other; the damping generated by a gas film in this situation is referred to as “shear damping”. Under the assumption of small displacement in during the oscillation, both damping

mechanisms generate damping forces relatively linear to the displacement and velocity of the moving plates. However, in large oscillations, due to end-effect and geometrical changes, boundary conditions during an oscillation varies; consequently, the force will show nonlinearity.

Extensive works have been done in [41-44] on squeeze film damping identification on MEMS. They showed viscous damping of air around the structure dominates at low frequencies but as frequency increases squeeze damping exceeds viscous one. In these works, both continuum and molecular approaches have been implemented, along with slip boundary conditions and compact models for different MEMS applications. One of the methods suggested to overcome the damping problem is through a perforated surface, but this approach is not applicable into micromirrors due to their optical performance.

As it will be discussed below, temperature, pressure, and the geometric properties play a role to dictate the physics of the interaction between the fluid and the solid walls. Because the micromirrors operate in air, however, and because of geometry of these devices, the hypothesis of continuum can be acceptable, even if in some cases detailed boundary conditions (e.g. slip boundary condition) are required. It is worthwhile to mention that, when decreasing the pressure to a fraction of the ambient one or down to a few millibars, the physics of the fluid problem tends to resemble rarefied gas dynamics, so that the fluid is no more a continuum.

In the following, we examine capability of our CFD tool, CFX, to model squeeze film damping and then we focus on shear damping happening in the actuator combfingers. Available analytical models for shear damping physics are presented. In these models slip boundary condition is formulized and is used to modify CFX for microscale simulations.

4.2 Squeeze film damping

Several MEMS devices like capacitance sensors and electrostatic actuators use electrodes in the form of parallel plates with a gap in between. One of these plates moves in the direction perpendicular to the plate surface, as plenty of them work at ambient pressure and not in vacuum, the air in the gap between plates plays an important role in the dynamic properties of system. Since the ratio of plates' area to the gap size is often very large, a fairly small displacement will squeeze high amount of air flow in or out of the narrow gap. Due to the fluid viscosity, the flow rate between the plates is limited, and this will increase the air pressure in the gap. The total damping by pressure force, which is acting on plates and affects the dynamics of plates, is called squeeze film damping. The theory of squeeze film damping has been developed years ago [62]. In [63] and [64] the authors

linearized the squeeze-film damping governing equation, the Reynolds equation, into a compact form to investigate the dynamic effect of air film. It has been shown that at low frequencies, the viscous dissipation dominates, whereas at higher frequencies, the spring like and inertial effects dominate. This behavior can be explained; in the presence of a compressible gas film, the moving surfaces are forced to squeeze the gas from between them to be able to move. The phenomenon has an interesting frequency response: below the corner frequency, the gas has enough time to flow away from the gap, thus causing dissipation, whereas above the corner frequency, the gas film is trapped and squeezed between the moving plates and behave like a spring with low dissipation. At the corner frequency the viscous and the spring-like forces acting on the surfaces are equal.

In case of torsional micromirrors, the mirror plate tilts around its centreline. On the contrary to the reflecting surface, the lower surface is confined with substrate. Tilting of the plate induces air squeezing and sucking at two sides. Squeeze film damping effect in micromirrors has been studied to show the dependency of the damping torque on the geometry of micromirror and substrate [65]. In practice, to decrease the damping effect in MEMS devices, some perforations need to be made in the plate to ease the flow of air from the gap; in micromirrors this option is out of Table, because of optical reasons. The Figure 4.1 shows the squeeze damping mechanism in a micromirror plate.

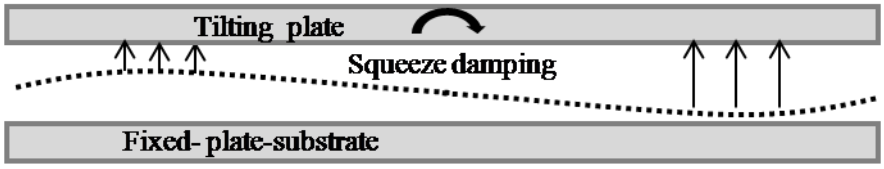

Figure 4.1 Schematic view of damping mechanism in tilting plates

Here, we adopt CFX as computational fluid dynamics (CFD) software to simulate the squeeze damping effect. Therefore, we adopted a test case, which has been already analyzed, and the results regarding squeeze film damping were extracted, in order to validate the CFX results with this set of data.

The aforementioned problem is a rotational resonator containing micro perforations; at one surface they are unconfined and, on the other surface, they are facing the stator, see Figure 4.2. We consider one of these micro perforation cells to study squeeze film damping.

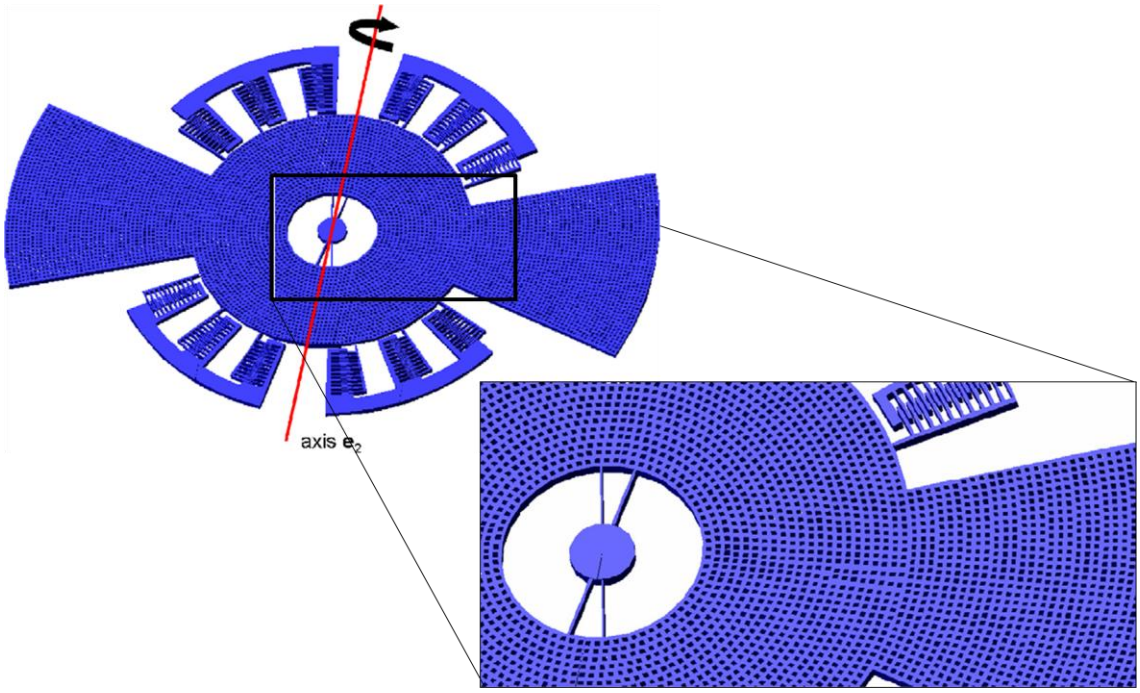

Figure 4.2 Reference MEMS structure (rotational resonator): detail of perforation cell [75]

The Figure 4.3 shows the fluid domain in the perforation cell consisting of three different zones from bottom to top; the slender part is in contact with the substrate (and within which squeeze film damping is happening), the middle body is in contact with the resonator cell, and the bigger cubic volume, which is the air above the perforation cell.

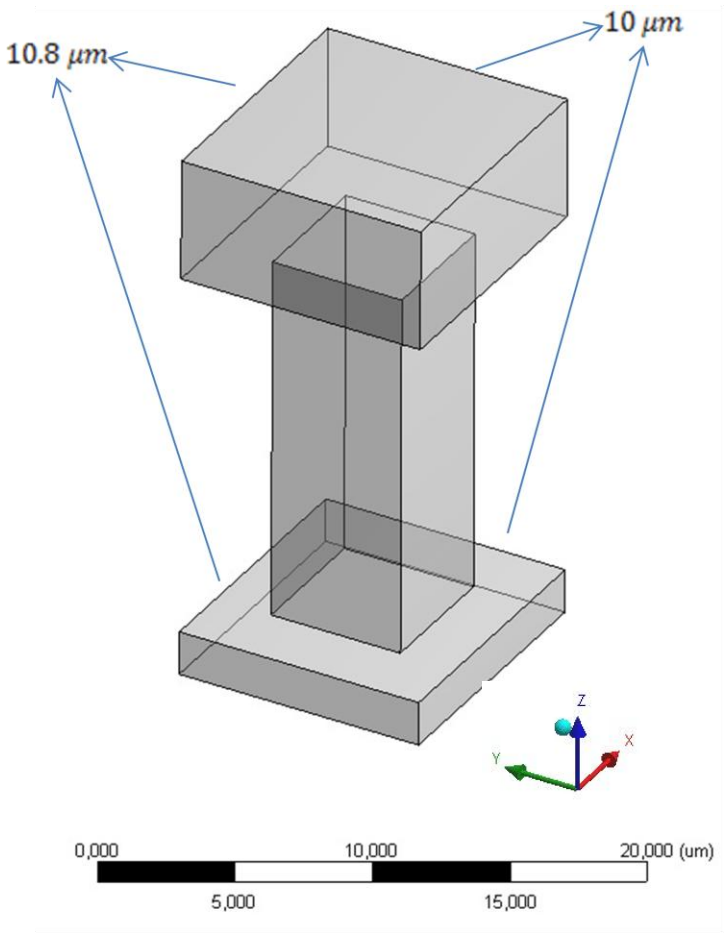

Figure 4.3 Perforation cell geometry showing the fluid domain

The perforation cell resonates in the *z*-direction and the air in lower part is squeezed. A symmetry boundary condition is introduced to account for neighboring cells' surfaces and the upper surface is left at the ambient air. The working frequency of the device is set to 4,550 Hz and the ambient pressure to 1 bar. The solid boundary is moved with a sinusoidal function of time, with unit velocity magnitude. The overall force on the unit cell reported in [75] as $1.492 \cdot 10^{-7}$ N.

Because of the symmetry, a quarter of perforation cell is modeled. The transient analysis is conducted in CFX and, after having approached a steady state, the unit force is computed. The Figure 4.4 shows the pressure contour at squeeze film section at one timestep. It should be mentioned that the squeezed cross section is not a square shape; therefore, the pressure contour at the squeeze wall is not symmetric.

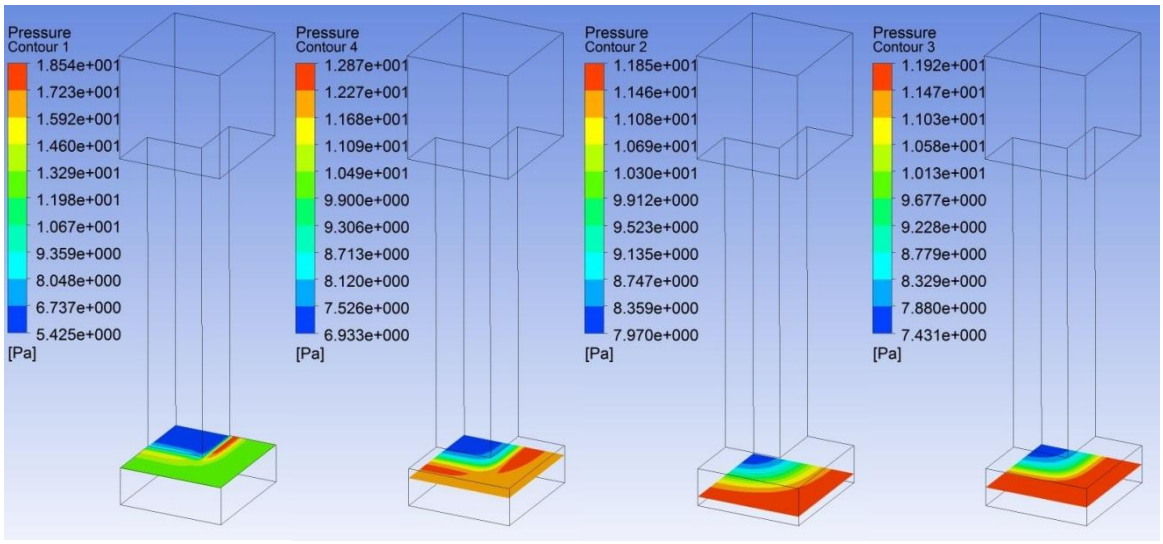

Figure 4.4 Pressure contour at air film

In the diagram below a sample of flow field is brought.

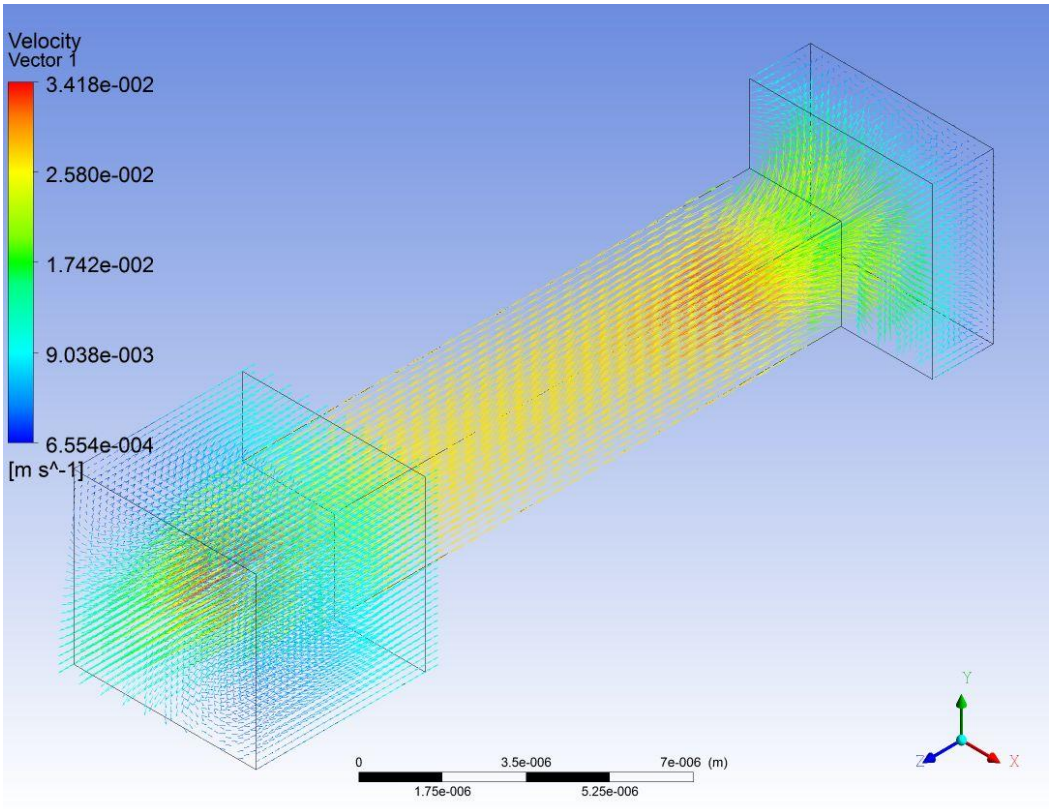

Figure 4.5 Flow field showing the velocity vectors

The solution here is an asymptotic one to the problem; as it can be seen in the Figure 4.5 the asymptote target (horizontal red line) is the overall force in [75].

These two diagrams in Figure 4.5 show that by lowering the value of input velocity and by using finer mesh, the results approach closer to the target value.

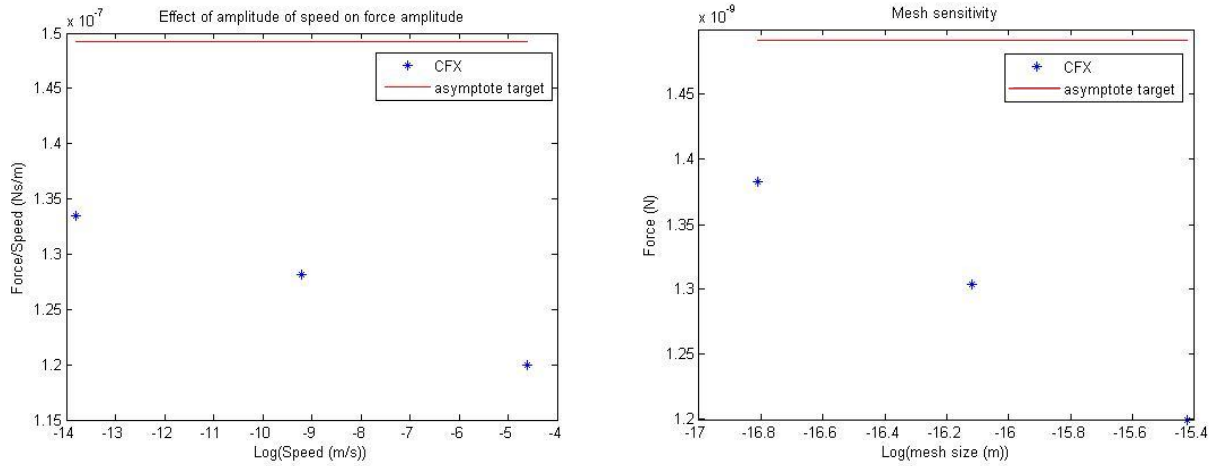

Figure 4.6 Asymptotic results regarding mesh sensitivity and input order sensitivity

This test case has demonstrated that, squeeze film damping can be modeled by CFX if fine mesh in air film region is used. It should be mentioned, by conducting more simulations for other squeeze film damping configurations, we would be more assure on accuracy of the method. Here in this thesis, our attention is focused on shear damping occurring in combfingers; therefore, further configurations are not studied.

4.3 Fluid damping between combfingers

Among different damping mechanisms in the resonant micromirrors, in [45] it has been shown that, the fluid-mechanical interaction within the combfingers is the dominant effect. In this section, the damping effect in combfinger zone is studied by presenting hydrodynamic equations governing the fluid domain for both fully developed steady flow and dynamic one. The conventional boundary condition and the slip boundary condition are applied for the both flow types.

4.3.1 Governing hydrodynamic equations

The Navier-Stokes equations are the main governing rules for flows. These equations are written in tensor notation for the flow of a viscous, laminar, Newtonian fluid of constant viscosity as [51]:

$$\text{continuity: } \frac{\partial \rho}{\partial t} + \frac{\partial (\rho u_k)}{\partial x_k} = 0 \tag{4.1}$$

$$\text{momentum: } \frac{\partial (\rho u_k)}{\partial t} + \frac{\partial (\rho u_k u_i)}{\partial x_k} = -\frac{\partial p}{\partial x_i} + \frac{\partial \tau_{ik}}{x_k} \tag{4.2}$$

where u is the fluid velocity vector (with components $u_k, k = 1,2,3$), p is the pressure and ρ is the fluid density. τ_{ik} is the viscous stress tensor, which can expressed as:

$$\tau_{ik} = \mu \left(\frac{\partial u_i}{\partial x_j} + \frac{\partial u_j}{\partial x_i} \right) - \frac{2}{3} \mu \frac{\partial u_k}{\partial x_k} \delta_{ij} \tag{4.3}$$

where μ is the coefficient of dynamic viscosity and δ_{ij} is the Kronecker delta. For a one-dimensional flow in a Cartesian coordinate system, the equations can be rearranged as follows:

$$\frac{\partial \rho}{\partial t} + \frac{\partial (\rho u)}{\partial x} = 0 \tag{4.4}$$

$$\frac{\partial(\rho u)}{\partial t}+\frac{\partial(\rho u u)}{\partial x}-\frac{\partial}{\partial x}\left(\mu\frac{\partial u}{\partial x}\right)-\frac{\partial}{\partial y}\left(\mu\frac{\partial u}{\partial y}\right) = -\frac{\partial}{\partial x}\left(p+\frac{2}{3}\mu\frac{\partial u}{\partial x}\right)+\frac{\partial}{\partial x}\left(\mu\frac{\partial u}{\partial x}\right) \tag{4.5}$$

where u is the Cartesian velocity component in the *x* direction, v is the Cartesian velocity component in the *y* direction.

In MEMS applications like our in hand problem due to the small length scales Reynolds number $Re=\rho\frac{VL}{\mu}\ll 1$, V and L are respectively, fluid velocity and characteristic length. Stokes number $St=\sqrt{frequency.\rho.H^2/\mu}$ shows the balance between the unsteady and viscous effects. If MEMS work in frequencies lower than 100 kHz, $St<1$, so a quasi-static incompressible Newtonian Stoke formulation can be implemented. Therefore, the Navier-Stokes equations for one-dimensional flow can be simplified to;

$$\mu\frac{d^2u}{dy^2}=\frac{dp}{dx} \tag{4.6}$$

where dp/dx is the pressure gradient.

4.3.1.1 Slip boundary condition

To account for non-continuum flow effects, arising from the relatively small dimensions of the gaps in MEMS, the governing Navier-Stokes formulation should be solved along with the slip boundary condition proposed by Basset [52];

$$\tau_t=\beta u_t \tag{4.7}$$

in which τ_t is the tangential shear stress on the wall, u_t is the tangential slip velocity on the wall and β is the slip coefficient relating shear stress and slip velocity on the wall. β can be expressed as a function of the mean free path between molecules of air [53], as:

$$\beta=\frac{\mu}{\frac{2-\sigma}{\sigma}\lambda} \tag{4.8}$$

where μ is the air viscosity, σ is the tangential momentum accommodation coefficient (TMAC), and λ is the mean free path of air molecules. In the cases where the mean free path is not negligible in compared to the characteristic length of the system, the collision of gas molecules with surface walls cannot be ignored. On the other hand, the ratio of surface to volume is also large. These characteristics emphasize the importance of gas interaction on micro flow fields. To be more accurate, this interaction should be considered where modeling the wall boundary condition. To account for this effect, TMAC is used to represent the statistical characteristics of the mean exchange of the tangential momentum [54]. For an ideally smooth wall (at the molecular level), the angle of incidence and reflection of molecules colliding with the wall surface remains identical and the tangential momentum does not change. This ideal condition is referred to as the "specular reflection" condition, which stands for the complete slip boundary condition. On the contrary, in the case of an ideal rough wall surface, the angle of reflection of the molecules is random so they lose all their tangential momentum. This case is referred to as the "diffusive reflection" condition. In real situations some molecules reflect diffusively and some specularly, so TMAC as a statistical coefficient, varying between 0 and 1 according to the ratio of diffusive reflected molecules to the overall collisions, accounts for the phenomenon. This coefficient is dependent on the characteristics of the fluid and solid involved in the problem, and on surface finishing. In case of the MEMS working at ambient pressure, TMAC usually is considered as 0.9 [55].

Using 4.7 and 4.8 we can write:

$$u_t = \frac{2-\sigma}{\sigma}\frac{\lambda}{\mu}\tau_t \,. \tag{4.9}$$

By knowing the definition of the Knudsen number, Kn as the ratio between the mean free path of air molecules and the characteristic length of the geometry, we rearrange the formulation as follows:

$$u_t = \frac{2-\sigma}{\sigma}\frac{KnD_h}{\mu}\tau_t \,. \tag{4.10}$$

Here, D_h is the characteristic length which depends upon the geometric parameters of problem including P_w and A_w respectively wetted perimeter and area of flow duct. Hydraulic diameter is usually calculated through:

$$D_h = \frac{4P_w}{A_w} \tag{4.11}$$

In the case of flow between parallel plates (see Figure 4.2) with a separation distance of H, it can be said that D_h is twice of the plate separation distance:

$$D_h = 2H. \tag{4.12}$$

Arranging these formulations we arrive at:

$$u_t = \frac{2-\sigma}{\sigma}\frac{Kn2H}{\mu}\tau_t. \tag{4.13}$$

The shear stress on the lower wall can be expressed as;

$$\tau_t = \mu\frac{du}{dy}\Big|_{y=0}. \tag{4.14}$$

It is worth mentioning that the shear stress on the upper wall can be calculated with the same method, with the little exception that the velocity gradient has the same magnitude as the lower one's but with opposite sign.

The tangential slip velocity can be written as;

$$u_t = \frac{2-\sigma}{\sigma}Kn2H\frac{du}{dy}\Big|_{y=0}. \tag{4.15}$$

To implement the above equation in the Navier-Stokes equations, calculation of the mean free path of air molecules is important. For an ideal gas modeled as rigid spheres of diameter $\mathfrak{D}$, the mean distance a molecule can travel between two successive collisions is titled as mean free path, and defined as [56]:

$$\lambda = \frac{\mathfrak{K}T_K}{\sqrt{2}\pi p\mathfrak{D}^2} \tag{4.16}$$

where $\mathfrak{K}$ is the Boltzmann's constant whose value is $1.380662 \cdot 10^{-23}$j/K and T_K is the absolute temperature (j and K respectively stand for joule and Kelvin). For standard ambient temperature and pressure (SATP), and an averaged air molecule diameter $\mathfrak{D} = 3.66 \cdot 10^{-10}$m (air is a set of different molecules, so a absolutely exact molecule diameter for air cannot expressed), the mean free path of air molecules is 69 nm. Later in the numerical setup, we will introduce the mean free path into the equations as a function of pressure as it is.

4.3.2 Fully developed laminar flow in parallel plates

As previously discussed, laminar flow between parallel plates is called Poiseuille flow and forms a parabolic velocity profile, see Figure 4.7. Analyzing this flow at the microscales, requires special considerations to be done as provided in the previous sections. By assuming of incompressible Newtonian fluid in laminar flow regime for the space between two plates (see Figure 4.7), the flow will be one-dimensional. Navier-Stokes momentum equation for this flow can be expressed as;

$$\mu \frac{d^2u}{dy^2} = \frac{dp}{dx}. \tag{4.17}$$

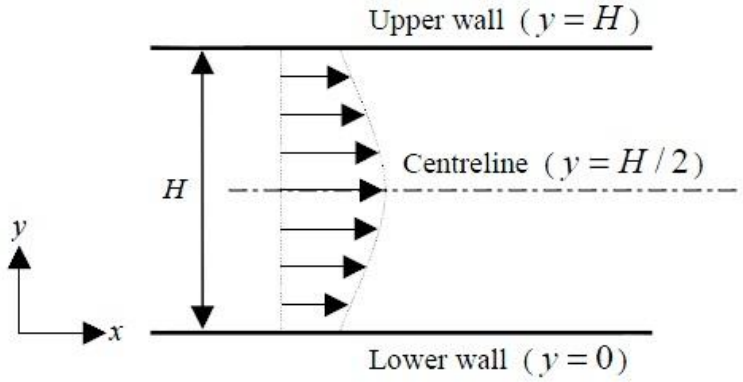

Figure 4.7 Slip flow between parallel plates

This equation must be solved along with the slip boundary condition which has been obtained previously (see Equation (4.15)):

$$u_t = \frac{2-\sigma}{\sigma} Kn2H \frac{du}{dy} \quad at\ y = 0 \tag{4.18}$$

and

$$u_t = -\frac{2-\sigma}{\sigma} Kn2H \frac{du}{dy} \quad at\ y = H\ . \tag{4.19}$$

The Navier-Stokes momentum equation is a linear, second order ordinary differential equation whose solution for velocity profiles along the *y*-directions in the form of:

$$u(y) = ay^2 + by + c \tag{4.20}$$

By imposing a slip boundary condition, the solution can be found as:

$$u(y) = -\frac{H^2}{2\mu}\frac{dp}{dx}\left(\frac{y}{H} - \frac{y^2}{H^2} + 2\frac{2-\sigma}{\sigma}Kn\right). \tag{4.21}$$

If Kn approaching to zero ($Kn \to 0$), one can get the familiar flow field with no-slip (stick) wall boundary condition for parallel plates [57]:

$$u_{no\ slip} = -\frac{H^2}{2\mu}\frac{dp}{dx}\left(\frac{y}{H} - \frac{y^2}{H^2}\right). \tag{4.22}$$

The maximum flow velocity can be observed in the centreline of flow ($y = H/2$) which is;

$$u_{max} = -\frac{H^2}{2\mu}\frac{dp}{dx}\frac{1}{4}\left(1 + 8\frac{2-\sigma}{\sigma}Kn\right). \tag{4.23}$$

Getting the above expressions is an important step to validate the results of the numerical simulation. Having u_{max} and the velocity profile in the space between the parallel plates, we can compare them with the results of the CFD software along with the slip boundary condition.

4.3.3 Computational setup for CFX

For the Poiseuille flow validation case, a rectangular channel has been developed with size of $12.5 \cdot 25 \cdot 50\ \mu m^3$. This geometry has been chosen to have a validation case with low computation cost. Therefore, meshing is not a crucial issue in the simulation procedure as it will be in later analyses. Still, a mesh sensitivity analysis was done to assure this statement.

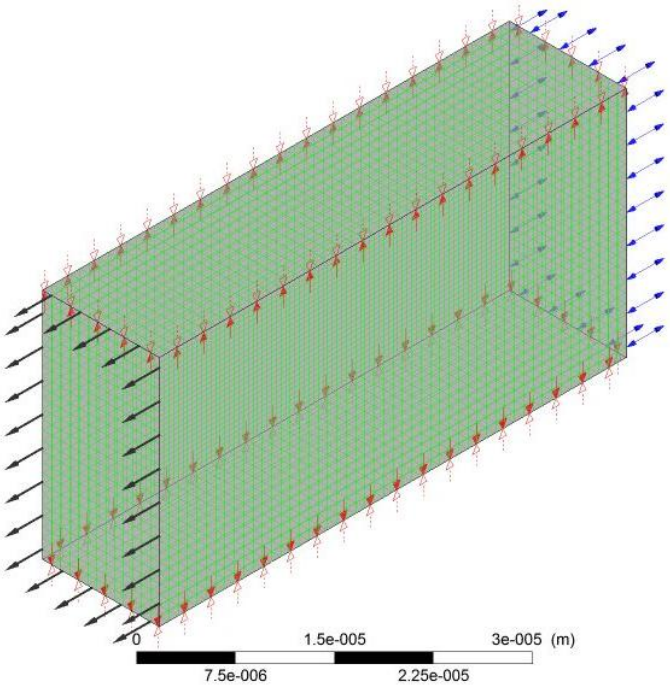

Figure 4.9 Poiseuille flow case study geometry

In Figure 4.9, a symmetry boundary condition is provided along the top and bottom surfaces to simulate infinite plates; a slip boundary condition is applied to two side surfaces and the other two surfaces are outlet and inlet shown by arrows in the figure. The air reference pressure is set to 200 Pa and a pressure drop of 2 Pa is introduced between openings, by considering the small length of the duct, it means a pressure gradient of 40000 Pa/m. The slip boundary condition has been introduced into CFX software through a CFX Expression Language (CEL) code as boundary conditions. Then, the simplified Navier-Stokes equation is solved using the expression of $\tau_t = (\sigma/(2-\sigma)) \cdot (\mu/\lambda)\, u_t$ with the λ as a function of total pressure of each point of fluid domain. Therefore, the mean free path is not constant in the fluid domain.

The analysis has been carried out in the form of a steady state analysis; the velocity field in duct is shown in Figure 4.10 and it can be seen that, the flow at the inlet is not fully developed. Therefore, the velocity profile is extracted at the end of the duct.

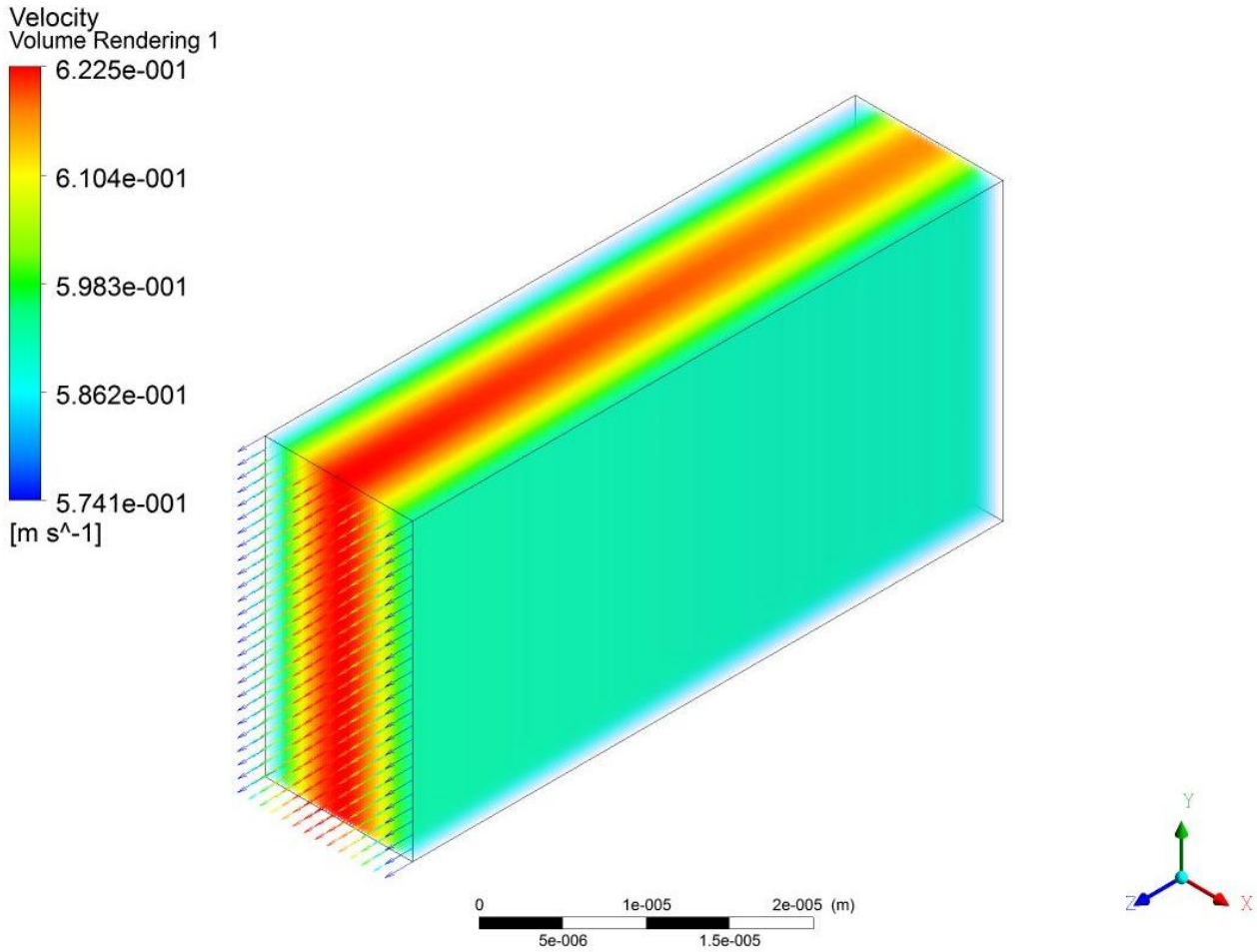

Figure 4.10 Flow velocity field

Also, velocity profile is analytical achieved by Equation (4.21) and is plotted in Figure 4.11 along with the velocity profile extracted from CFX. The difference between the profiles is 0.01 m/s constant over duct width. The discrepancy of the numerical result respect to the analytical method is 1.5 %, which is an acceptable error.

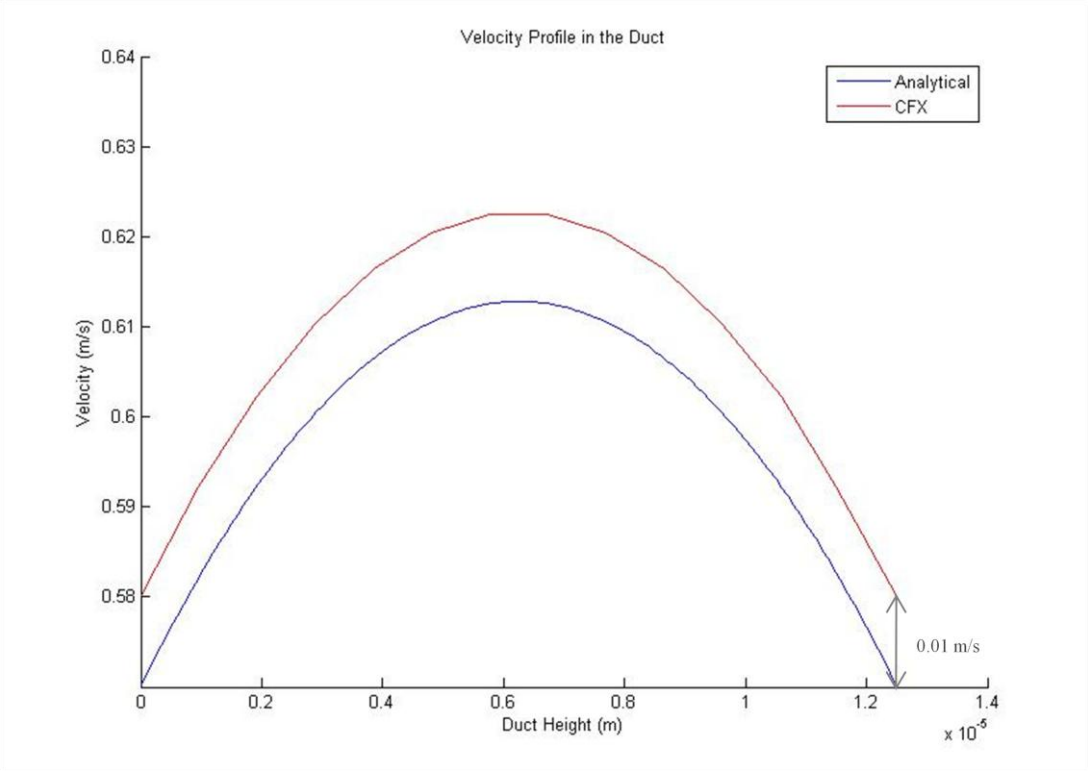

Figure 4.11 Comparison between CFX (numerical) and analytical Solution

4.3.4 Dynamic damping model

In the previous section, the Navier-Stokes equations have been solved neglecting the inertial forces. We assumed the presence of a quasi-static flow, hence the analytical frequency-independent damping model has been derived. To extend the damping model to fast vibrating structures, a velocity distribution changing with time and displacement should be considered [58]. Assume two surfaces bounding a flat gas film, separated by H and moving in a direction parallel to each other. The surfaces are considered large with respect to the other dimensions and thus the edge effect is neglected. The problem is still governed by the Navier-Stokes equations but some assumptions and restrictions should be made at the beginning;

- The amplitude of oscillation is small in comparison with size of surface;
- The width and length of plates are large with respect to gap between plates;
- The velocity of the surfaces is low enough to prevent heating the fluid in between. This limits the amplitude at high frequencies.

The dynamics of gas in between of plates can now be modeled through the one-dimensional diffusion equation [59]:

$$\frac{\partial u(y)}{\partial t} = \nu \frac{\partial^2 u(y)}{\partial y^2} \tag{4.24}$$

where $u(y)$ is the velocity distribution; ν is the kinematic viscosity $\nu = \mu/\rho$; ρ desnsity of the gas. Equation (4.24) is solved in the frequency domain for a steady-state sinusoidal velocity excitation with an amplitude u_r and an angular frequency ω. The solution can be written in the form of;

$$u(y) = C_1 \sinh(qy) + C_2 \cosh(qy) \tag{4.25}$$

where $q = \sqrt{j\omega/\upsilon}$ is the complex frequency variable. The constants C_1 and C_2 are determined from the boundary conditions. The shear force acting on the walls with a surface area A is:

$$\tau_{xy} = -\mu A \frac{\partial u(y)}{\partial y}\Big|_{y=0,H} \tag{4.26}$$

and the quantity

$$\xi = -\frac{\tilde{\tau}_{xy}}{u_r} \tag{4.27}$$

gives the relation between the shear force acting on the surface and the surface velocity, for a periodic steady state. This complex quantity, the damping admittance ξ, also contains the phase information, and the actual damping coefficient which is the real part of ξ.

Equation (4.25) should be solved by assigning the boundary conditions; then, the velocity profile and damping coefficient of the fluid-structure will be obtained.

4.3.4.1 One surface moving, continuum boundary condition

Let's assume, the lower surface be fixed and the upper one moves with a velocity u_r and let be $u_0(y)$ the velocity distribution formed in the gap. Applying boundary condition for viscous flow as;

$$u_0(0) = 0 \tag{4.28}$$

$$u_0(H) = u_r \ . \tag{4.29}$$

The velocity function is

$$u_0(y) = u_r \frac{sinh(qy)}{sinh(qH)}. \tag{4.30}$$

The resulting complex damping admittance solved from equitation (4.26) and Equation (4.27) is

$$\xi_0 = \frac{\mu A q}{\tanh(qH)}. \tag{4.31}$$

The actual damping on the moving surface is the real part of Equation (4.31).

4.3.4.2 One surface moving, slip boundary condition (stick BC)

The method for deriving the damping the admittance is similar to what described in Section 4.3.4.1, but the boundary condition is different. Again, one surface is moving, but the boundary condition is the first order slip model instead of stick one [60]:

$$\begin{aligned} u_1(0) &= \lambda \frac{\partial u_1(y)}{\partial y}\Big|_{y=0} \\ u_1(H) &= u_r - \lambda \frac{\partial u_1(y)}{\partial y}\Big|_{y=H}. \end{aligned} \tag{4.32}$$

The velocity function that satisfies Equation (4.25) with the given boundary condition is

$$u_1(y) = u_r \frac{\sinh(qy) + q\lambda\cosh(qy)}{(1+q^2\lambda^2)\sinh(qH) + 2q\lambda\cosh(qH)}. \tag{4.33}$$

Therefore, the damping admittance for this boundary condition can be derived, as:

$$\xi_1 = \frac{\mu A q(1+q\lambda\cosh(qy))}{2q\lambda + (1+q^2\lambda^2)\tanh(qH)}. \tag{4.34}$$

The actual damping coefficient is once again the real part of the damping admittance above reported.

4.3.4.3 Two surfaces moving, continuum boundary condition (stick BC)

In this configuration we investigate the flow between two oscillating plates by u_r. The flow should have uniform velocity u_r on all domain at low frequencies. As the frequency increases, the inertial force importance emerges.

Assume both surfaces oscillate with velocity u_r and have the same phase. The velocity distribution of the flow in the gap is shown by u_{p0}. The flow at higher frequencies should show a parabolic Poiseuille-type flow [61]. The boundary conditions are:

$$u_{p0}(0) = u_{p0}(H) = u_r \ . \tag{4.35}$$

Solving the general Equation (4.25) with this boundary condition, the velocity distribution in the gap for different frequencies appears to be:

$$u_{p0}(y) = u_r \left[\frac{1-\cosh(qH)}{\sinh(qH)}\sinh(qy) + \cosh(qy)\right]. \tag{4.36}$$

Like before, the damping admittance, ξ_{p1}, can be derived by Equations (4.31) and (4.36)

$$\xi_{p0} = \mu A q \left[\frac{1-\cosh(qH)}{s\sinh(qH)}\cosh(qH) + \sinh(qH)\right]. \tag{4.37}$$

4.3.4.4 Two surfaces moving, slip boundary condition

To investigate the effect of slip boundary condition on the flow formation in between two oscillating plates, we consider appropriate boundary conditions:

$$u_{p1}(0) = u_r + \lambda \left.\frac{\partial u_1(y)}{\partial y}\right|_{y=0} \tag{4.38}$$

$$u_{p1}(H) = u_r - \lambda \frac{\partial u_1(y)}{\partial y}\bigg|_{y=H}.$$

The difference between boundary conditions in $y = 0$ and $y = H$ is coming from the coordinate point we put on the lower surface. Velocity gradient at two surfaces are similar but we should consider negative direction in lower surface.

After deriving C_1 and C_1 in Equation (4.26), the velocity profile u_{p1} becomes:

$$u_{p1}(y) = K_{p1}\sinh(qy) + (u_r - \lambda q K_{p1})\cosh(qy) \tag{4.39}$$

where

$$K_{p1} = u_r\left[\frac{1 - \cosh(qH) - \lambda q\sinh(qH)}{\sinh(qH) + 2\lambda q\cosh(qH) + \lambda^2 q^2\sinh(qH)}\right]. \tag{4.40}$$

Like before, by deriving the velocity profile at near the wall, we can obtain the damping admittance;

$$\xi_{p1} = \frac{\mu A}{u_r}\left[K_{p1} q\cosh(qH) + (u_r - \lambda q K_{p1}) q\sinh(qH)\right]. \tag{4.41}$$

By what achieved above for four different configurations, and defining corner frequency $f_d = \nu/(2\pi H^2)$, where $qH = 1$, a wide range of studies can be done. First we derive the profile of velocity amplitude in different frequencies and consecutively to show the dynamic response characteristics, the flow formation is shown by time snapshots of flows. Also damping is studied for the presented configurations. The mean free path of air molecules in ambient pressure is 69 nm, the dynamic viscosity is $18.3 \cdot 10^{-6}$ kg/ms and flows are obtained for $H = 3$ and 12 μm . These gaps are chosen based on the fact that, the gap between a pair of stator/rotor combfinger and two successive rotor combfingers are respectively 3 and 12 μm .

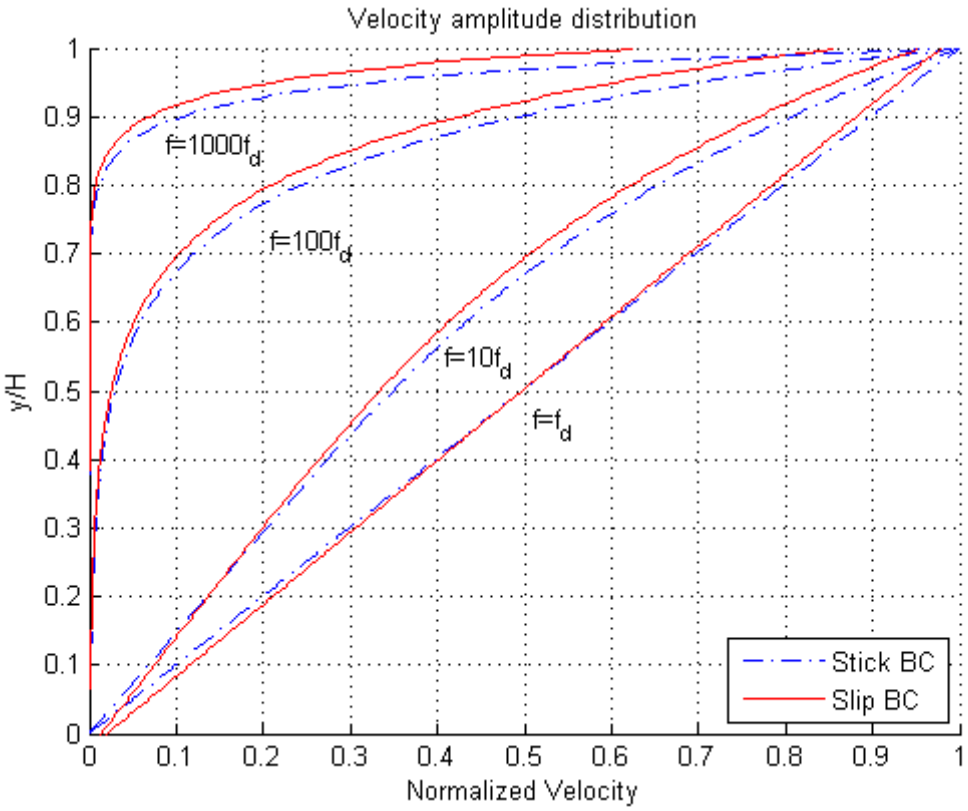

Figure 4.12 Velocity amplitude distribution for "one surface moving" configuration along with both stick and slip boundary condition, gap $H = 3$ μm

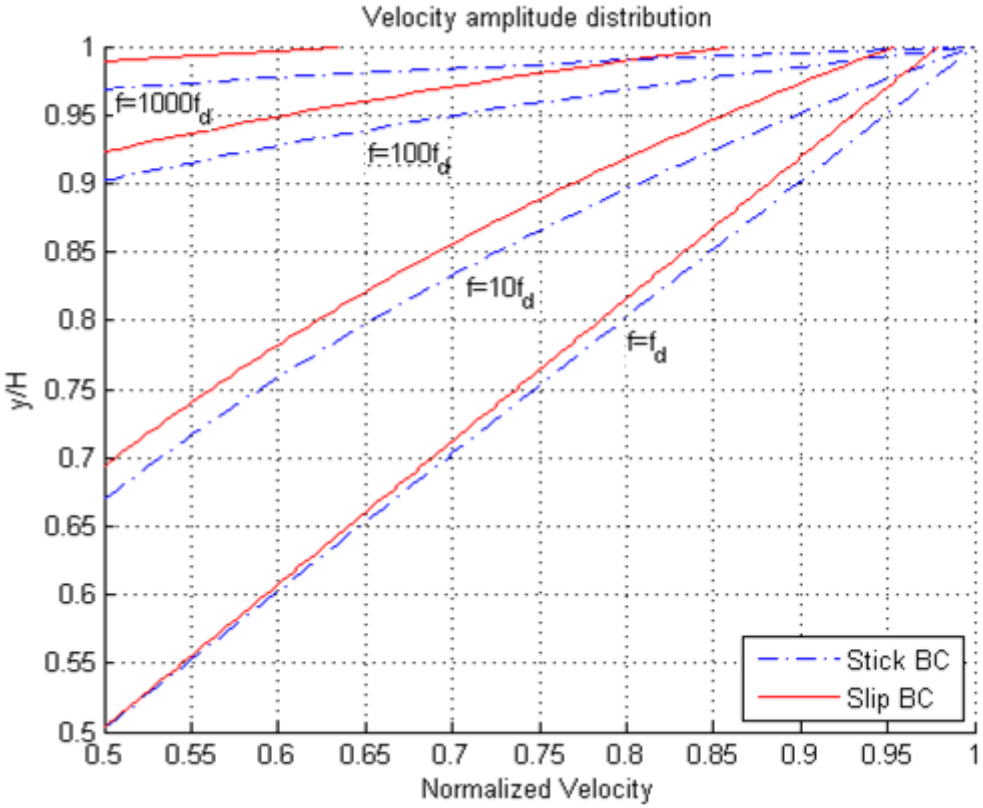

Figure 4.13 Magnification of Fig. 4.6 near the wall vicinity

From Figure (4.12), the importance of oscillation frequency in inertial forces and consequently on flow formation can be seen. At frequencies smaller than $f_d = 323{,}615$ Hz (considering 3 μm gap), the velocity field shows a Couette flow between two surfaces. As the frequency exceeds f_d, inertial forces get dominant and affect velocity amplitude and phase. A higher frequencies and only a small part of the gas close to the moving surface oscillates.

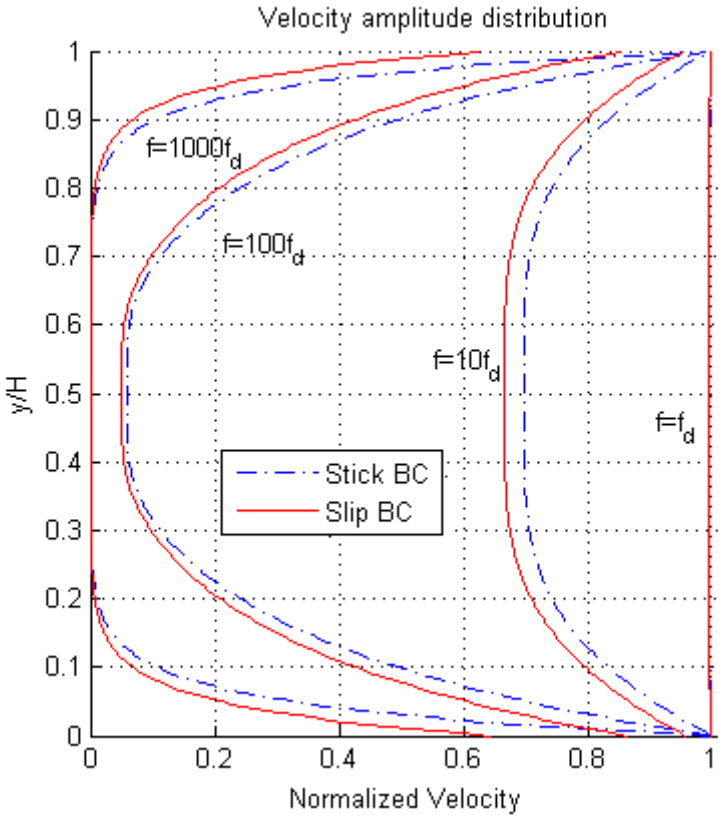

Figure 4.14 Velocity amplitude distribution for "two surfaces moving" configuration along with both stick and slip boundary condition, gap $H = 3$ μm

The velocity profile between the two oscillating surfaces is illustrated in Figure 4.14. It is obvious that at frequencies lower than f_d, the inertial forces are not strong enough, so the gas between two surfaces moves with the same velocity as the walls move. Further than f_d, inertial forces change the velocity profile. The flow formed has a parabolic profile which, in case of pressure driven flow between two fixed walls is called Poiseuille flow. At higher frequencies, like in the previous configuration, only a small part of gas moves and this portion decreases as the frequency increases. Another point which should be noticed is the similarity

of flow between these two configurations at high frequencies. At high frequencies the shear forces do not penetrate through all flow profile; therefore, only a portion of the flow near the wall moves. This point makes these configurations identical at high frequencies.

To see the effect of gap H between two surfaces, the velocity profile is achieved for another value of $H = 12$ μm. In the diagrams below the difference on the slip boundary condition can be seen.

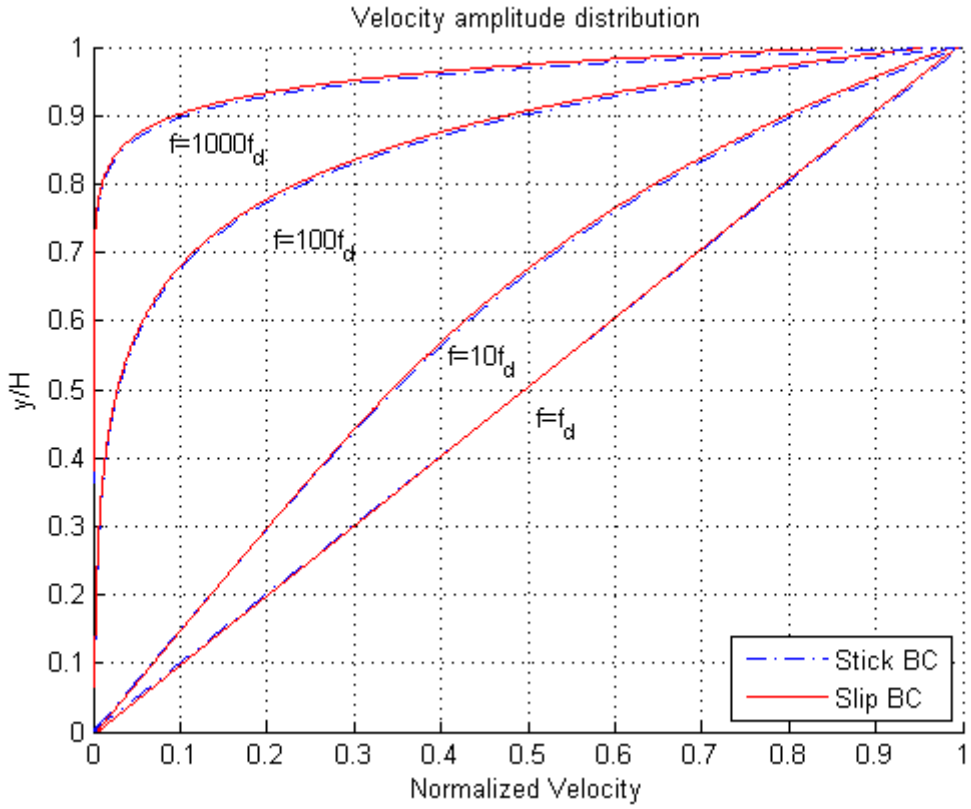

Figure 4.15 Velocity amplitude distribution for "one surface moving" configuration along with both stick and slip boundary condition, gap $H = 12$ μm.

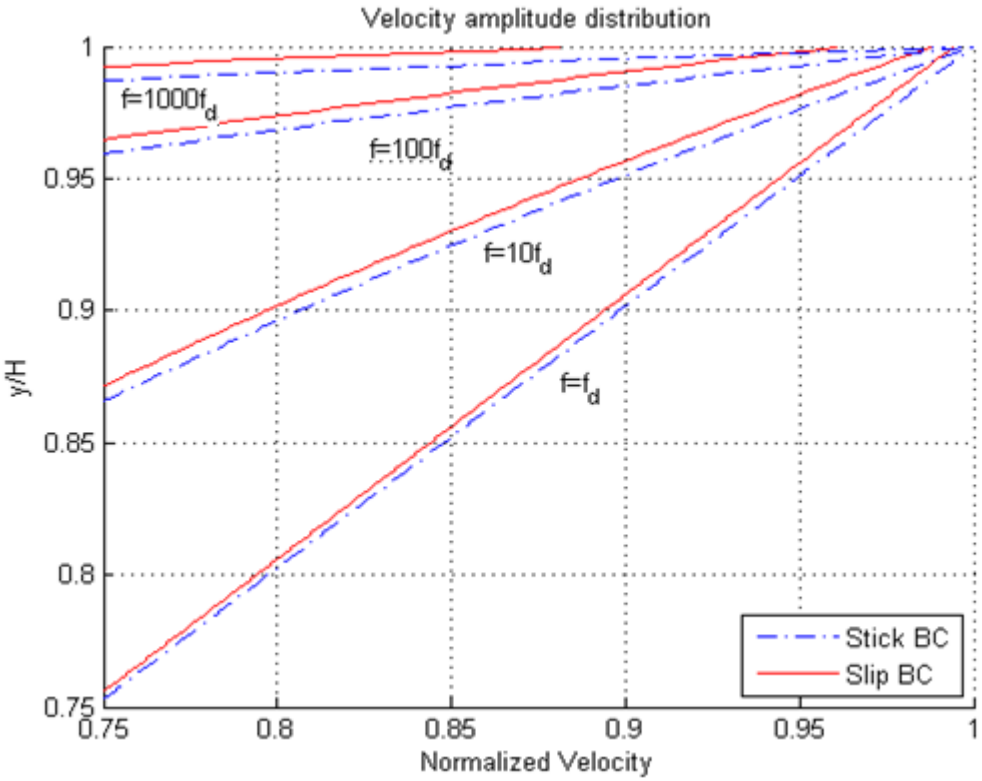

Figure 4.16 Magnification of Fig. 4.9 near the wall

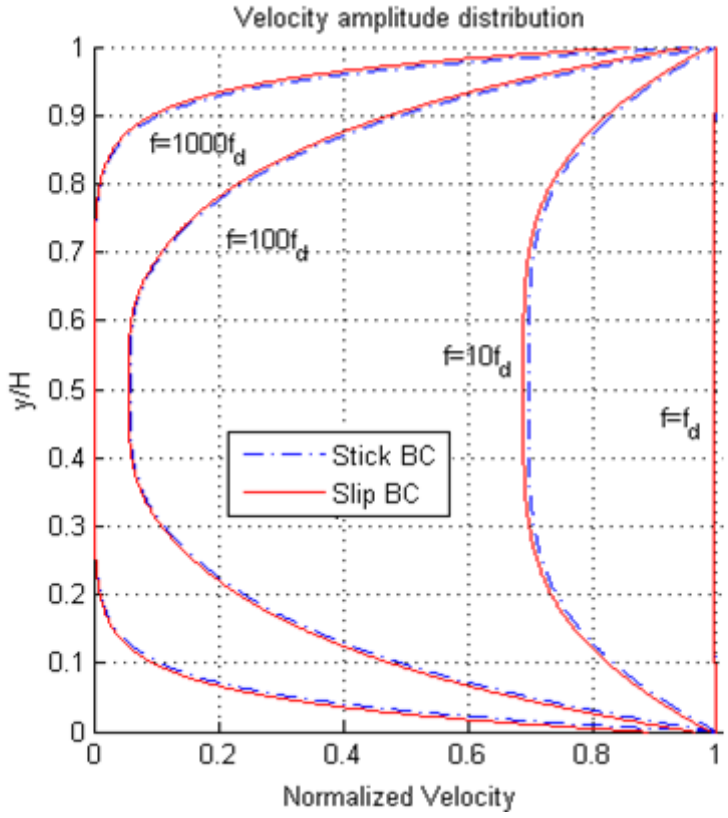

Figure 4.17 Velocity amplitude distribution for "two surfaces moving" configuration along with both stick and slip boundary condition, gap $H = 12$ μm

Figures 4.9-11 show that, increasing the gap to 12 μm has decreased the corner frequency to $f_d = 20{,}225$ Hz. This means the inertial forces are important in lower frequencies. Also increasing the gap has attenuated the slip boundary condition. So for this gap size, the stick and the slip boundary condition do not make any difference, see Equation (4.22).

In Figure 4.18 and 4.19, snapshots of the velocity distribution at different times are shown, for both the cases of one moving surface and two moving surfaces. The frequency chosen to illustrate the flow dynamics should be more than f_d, otherwise the flow will be in the fully developed quasi static condition and in phase with wall. Here, we chose $f = 100 f_d$ to obtain Figures 4.18-21 and $H = 3$ μm. It is shown that, with the exception of wall slip velocity, the dynamics of flow in stick and slip boundary condition is the same.

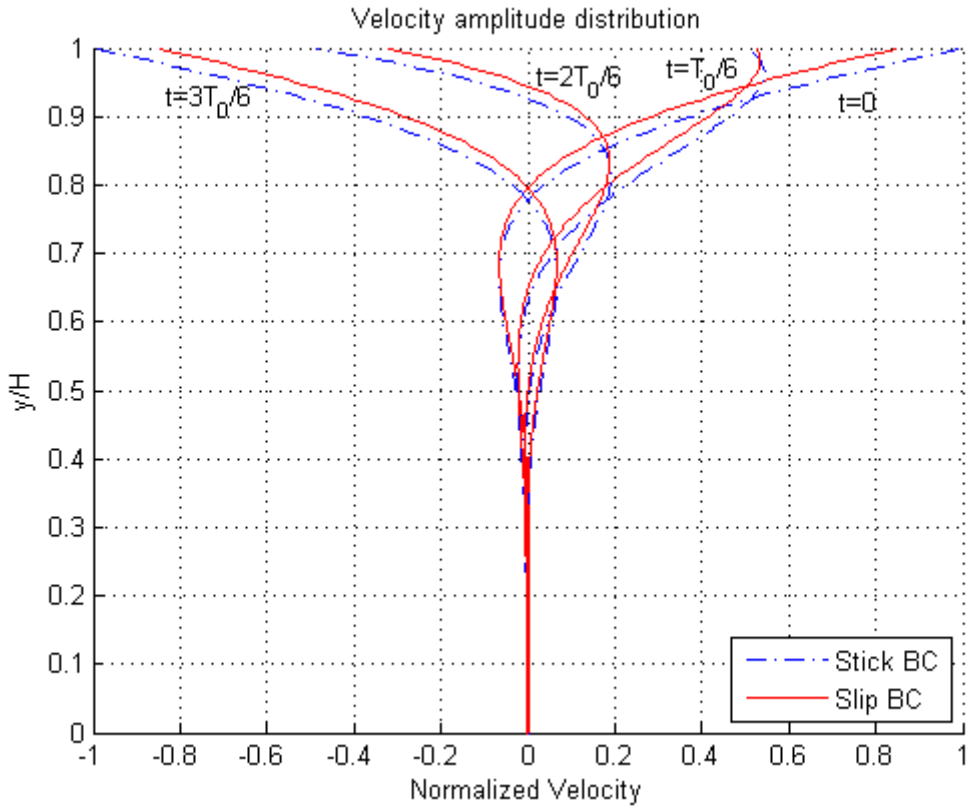

Figure 4.18 Velocity distribution between walls, gap $H = 3$ μm , one moving surface.

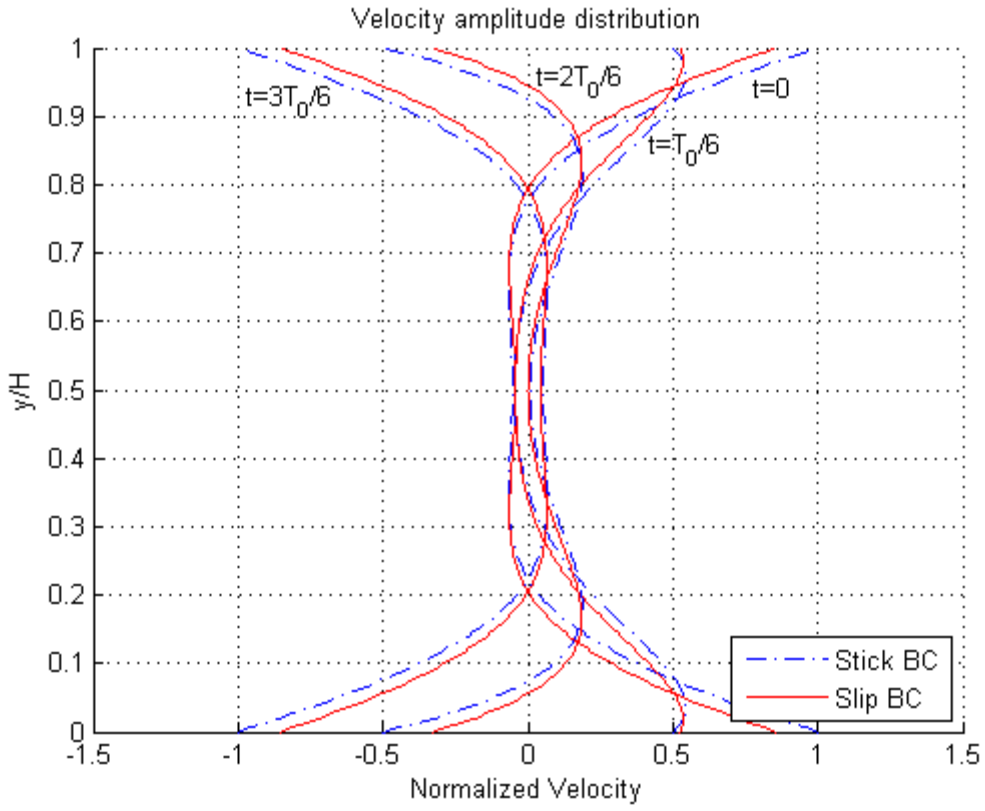

Figure 4.19 Velocity distribution between walls, gap $H = 3$ μm *, Two moving surfaces.*

In figures 4.18 and 4.19, snapshots of velocity distribution are shown at different fractions of oscillation period of wall motion, T_0. Velocity distribution at other times like, $t = \frac{4T_0}{6}\ and\ \frac{5T_0}{6}$ are mirror of the ones in these two figures.

To see once again the effect of gap between the plates, in Figures 4.20 and 4.21, we report velocity distributions for a gap $H = 12$ μm ;

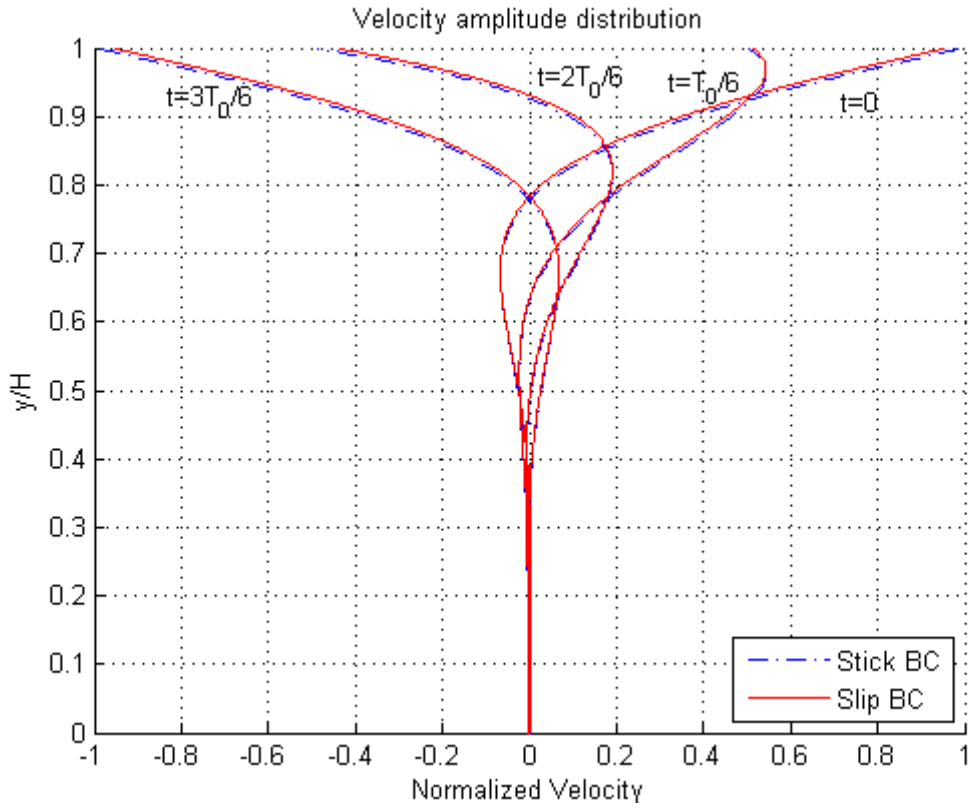

Figure 4.20 Velocity distribution between walls, gap $H = 12$ μm , one moving surface.

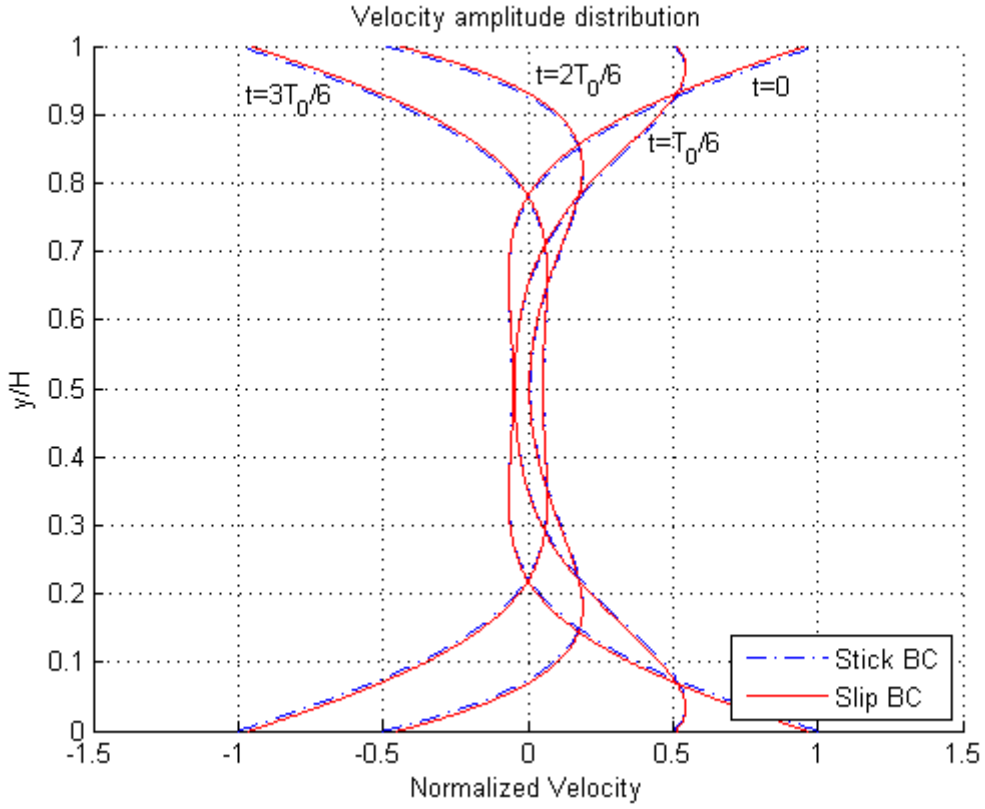

Figure 4.21 Velocity distribution between walls, gap $H = 12$ μm , Two moving surfaces.

As it can been understood by comparing Figures 4.20 and 4.21 with Figures 4.18 and 4.19, the gap distance only slightly affects the flow with the slip boundary condition and not stick boundary condition.

Another issue we can investigate on the topic of the equations derived in this chapter is the damping coefficient in all these cases. Normalizing the real values of Equations. (4.31) and (4.34) by $\mu A/\mathrm{H}$, the damping coefficients are shown in Figure 5.16 and Figure 4.17 for the configuration of one moving surface with $H = 3$ μm and $H = 12$ μm.

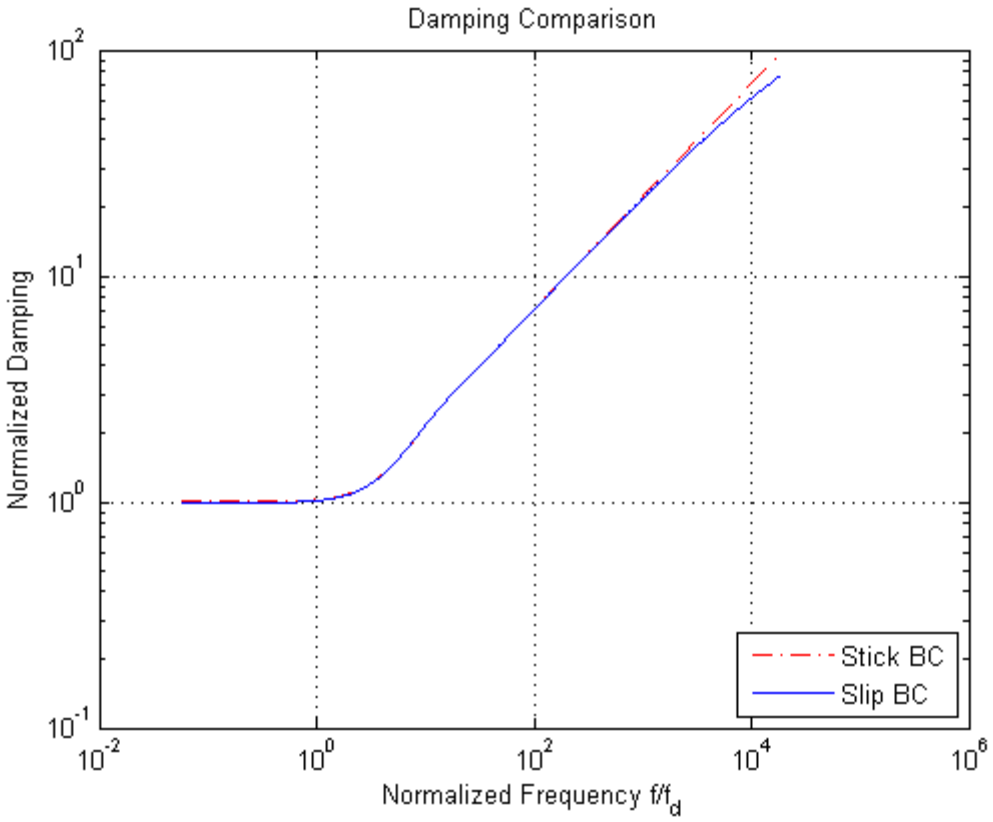

Figure 4.22 Normalized damping coefficient for case of one moving surface, gap $H = 12$ μm

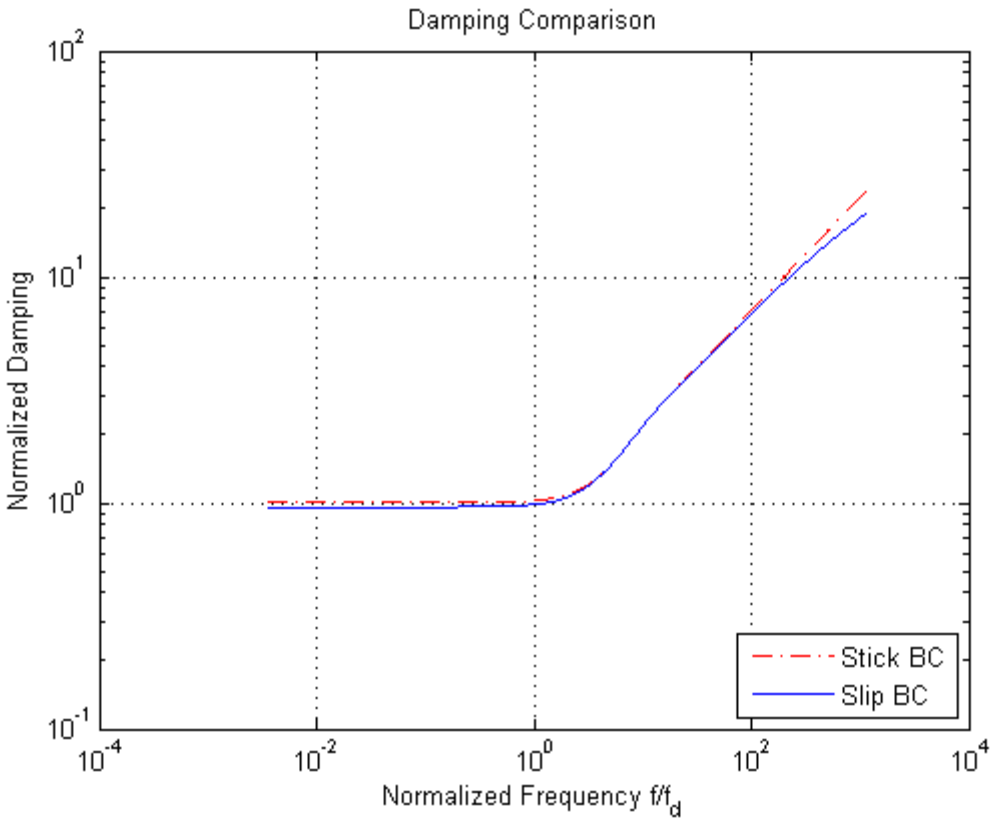

Figure 4.23 Normalized damping coefficient for case of one moving surface, gap $H = 3$ μm

As it can be seen from Figures 4.22 and 4.23, damping coefficients at frequencies below f_d show constant values. This value for the slip boundary condition is a bit lower than the one corresponding to the stick boundary condition. Another difference observable at higher frequencies is that, the slip boundary condition shows a lower damping coefficient than the stick boundary condition.

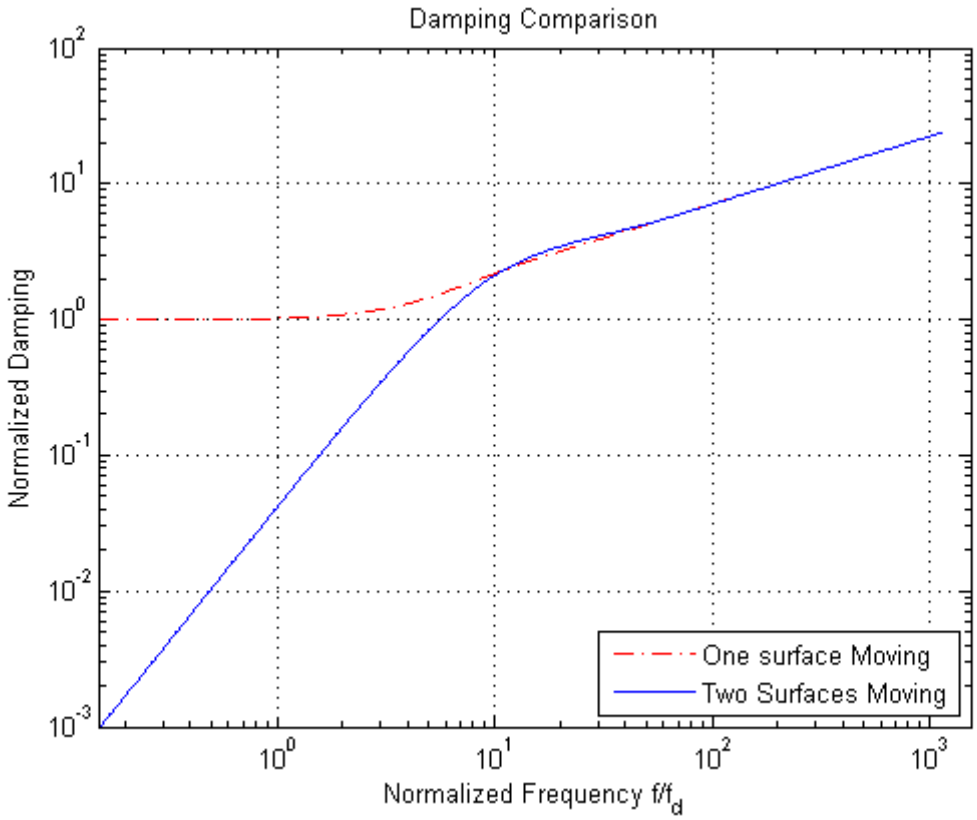

Figure 4.24 Normalized damping coefficient for case of one moving surface, stick boundary condition.

Figure 4.24 shows the damping value for the stick boundary condition in both configurations. Damping for two moving surfaces case at low frequencies is negligible and by increasing the frequency, damping for both cases show the same value and trend. As already mentioned in this section, at higher frequencies only a small part of air is moving with the oscillating wall. This behavior can be seen also in the resemblance of damping diagrams of one moving and two moving surfaces.

From this basic understanding regarding the simplified geometry, it emerges the importance of the oscillation frequency in the damping of combfingers. Therefore, an extensive 3-D simulation of the fluid-mechanical effects is required not only to consider the oscillation frequency but also to take account of the complexity of the geometry. This simulation must be carried out individually for future designs of the HD and the Full-HD micromirrors, which need high frequency ranges such as 25 up to 30 kHz.

This chapter has investigated two important damping mechanisms occurring in the micromirror. Also our numerical tool, CFX has been examined to validate its capability for simulating damping in micromirror. It has been shown by an analytical model that, damping in our microscale model is not only geometry dependent, but also varies with higher oscillation frequencies. In the next chapter, the damping effects in the actual micromirror will be simulated and studied.

Chapter 5

Air damping modeling in combfingers

First, in Sections 5.1 and 5.2 we present the general characteristics of the model adopted, along with the results in the simple case of small amplitude of oscillations (small displacements). Then, in Sections 5.3, 5.4 and 5.5, we address the issue related to the large relative motion of the solid parts of the micromirror. It is worthwhile to emphasize that, in order to account for the effect of vibrations on fluid when large displacements of solid boundaries are present, a considerable modeling effort is necessary. Finally, in Section 5.6, the corresponding quality factor is obtained, and comparisons with the experimental results are carried out.

5.1 Numerical simulation: base model

Among different damping mechanisms in the micromirror, in [45] it has been shown that, the fluid-mechanical interaction within the combfingers (the shear damping) is dominant. In this section, the damping effect in combfinger zone is examined through CFX by considering a closed volume boundary of the combfinger pair.

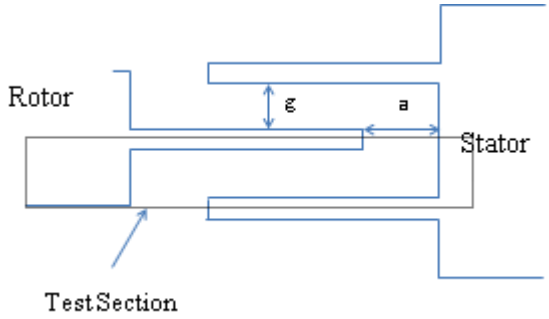

Figure 5.1 Schematic of a combfinger pair

To apply the slip boundary condition a user subroutine which already worked properly in previous analysis (see Section 4.3.2) was adapted to CFX. Due to the complexity of the geometry and the dynamic nature of the problem, using this boundary condition in the analysis is drastically time consuming. Noticing that the

damping mechanism is mostly happening in the gap between two fingers when they are completely aligned, one can write the shear force equation such as below:

$$\{F_d\} \approx \{F_{Couette}\} = -\mu \frac{A_s}{g}\{u\} \tag{5.1}$$

where A_s is the overlapped area of combfinger which the damping force is applied on, g is the gap between combfingers, μ is the dynamic viscosity and $\{u\}$ is the moving finger's velocity vector. This equation explains the drag force for the ordinary stick boundary condition. Recalling that the definition of Knudsen number Kn, as the ratio between mean free path of air molecules and the characteristic length of the geometry, this number here turn out to be around 0.01. That is on the limit between the continuum approach and the slip velocity approach. Several corrections are developed and suggested by different researchers to modify the Couette flow formula to adapt the new situation. The common ground of these approaches is to use a modified (effective) dynamic viscosity of fluid into the formulation [46]:

$$\mu_{eff} = \frac{\mu}{1 + f(Kn)} \tag{5.2}$$

$$\{F_{Couette}\} = -\mu \frac{A_s}{g}\{u\} \quad \rightarrow \quad \{F_{Couette}\} = -\mu_{eff} \frac{A_s}{g}\{u\} \tag{5.3}$$

Different approximations for $f(Kn)$ used in literature are gathered in Table 5.1. They differ especially at high Knudsen numbers, and the approaches to derive these equations are different mostly in terms of geometry and applications. The first empirical equation [47], by Knudsen, is achieved for the gas flow in capillary tubes. Burgdorfer [48] used the modified Reynolds equation and it is applicable in the analysis of gas-lubricant bearings, but limited to Knudsen numbers up to unity. Hsia, Domoto [49] and Mitsuya [60] tried to extends the applicability range of Burgdorfer's equation by adding a higher-order term. The latter one furnished a surface-correcting coefficient $(2-\sigma)/\sigma$ where σ is the tangential momentum accommodation coefficient (TMAC). This coefficient as it has been already explained, is dependent on the interaction of fluid molecules colliding the solid surface and for most engineering uses, it is between 0.9 and unity (the maximum possible value for the coefficient). Veijola [46] expressed the effective viscosity in terms of the Poiseulle flow rate, which cannot be presented in closed form solution, so an approximation is suggested that is consistent with original equation higher than 95% at $0 \leq Kn \leq 880$.

Author	Year	Function *f*(Kn)
Knudsen	1906	$\frac{ZKn}{0.4174}, Z = \frac{Kn + 2.507}{Kn + 3.095}$
Burgdorfer	1959	$6Kn$
Hsia and Domoto	1983	$6Kn + 6Kn^2$
Seidel	1993	$\frac{Kn}{0.7}$
Mitsuya	1993	$6\frac{(2-\sigma)}{\sigma}Kn + \frac{8}{3}Kn^2, 0 \leq \sigma \leq 1$
Veijola	1995	$9.638Kn^{1.159}$

Table 5.1 Different auxiliary expressions used for deriving the effective viscosity in equation $\mu_{eff} = \mu/(1 + f(Kn))$.

It should be noted that the effective viscosity is not only dependent on the dynamic viscosity, but also on temperature and pressure fields in the fluid domain. On the other hand, the effective viscosity is dependent on the Knudsen number, which is related to the local characteristics of fluid (pressure and temperature) and structure (characteristic length).

As already mentioned, using the aforementioned subroutine for slip boundary condition in the analyses is time consuming. Considering the worst possible situation, featuring all the combfingers' lateral surfaces located with 3 μm gap in between (the minimum gap between different surfaces in the geometry), with this gap that stands still during the tilting period, we can show with Veijola empirical equation that the error of using no slip boundary condition instead of slip boundary condition reaches at most 5%. Therefore, simplifying the boundary conditions provides a significant time saving and ease of convergence on exchange with a bit of accuracy.

In this chapter, we analyze a model based on the actual geometry of the micromirror, whose dimensions can be found in Table 3.1. The real motion of the rotor is a tilting one around *y*-direction mentioned in Figure 2.11. To start with, we examine the model with a translational motion of the combfinger along *z*-direction. It should be noted that in Figure 5.2 one side of combfinger is shown with translational movement, but for the rotational case both sides should be modeled, see Figure 5.24. The motion is applied on the rotor in the form of a

sinusoidal function of time with different values for displacement amplitude of the oscillation. Several analyses have been conducted with different values for displacement amplitude. The displacement amplitude can be increased till it causes mesh distortion in the fluid domain. To overcome the mesh distortion problem and conducting the simulation for large oscillations, we will introduce a remeshing method in Section 5.3.

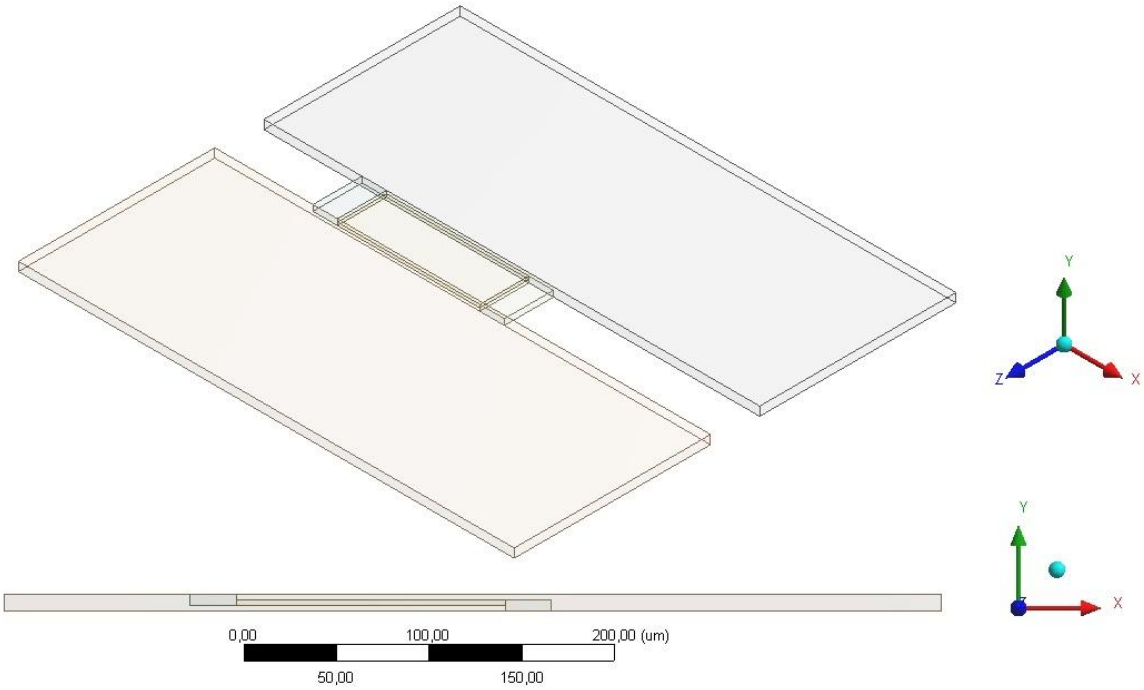

Figure 5.2 Geometry modeled in ANSYS CFX. The domains visible correspond only to air; structure are considered at the boundaries of fluid domain

FEM modeling is carried out in ANSYS-CFX. One quarter of a combfinger pair made of stator and rotor, and the surrounding air have been input. Boundary conditions are applied, including symmetry, opening and stick boundary conditions. On the Figure 5.3 the different boundaries are visible. The laminar fluid model without heat transfer capability is used for modeling air. The state properties of air are temperature $T = 25\,℃$; density $\rho = 1.185\,\mathrm{kg/m^3}$ and pressure $p = 1\,\mathrm{atm}$.

To adjust the appropriate flow regime to the solver, we have to define the turbulence of problem. This can be done by estimation of Reynolds number in the flow field through:

$$Re = \frac{\rho V L}{\mu} \tag{5.4}$$

where ρ is the air density; μ is air dynamic viscosity; V is mean flow velocity value and L is the geometry characteristics length scale. MEMS applications where the length scales are on the order of micron, limits the upper level of Re far lower than $2{,}300$, in which the regime transition between laminar flow and turbulence flow occurs. Thus, we can assume the flow inside the control volume to be laminar.

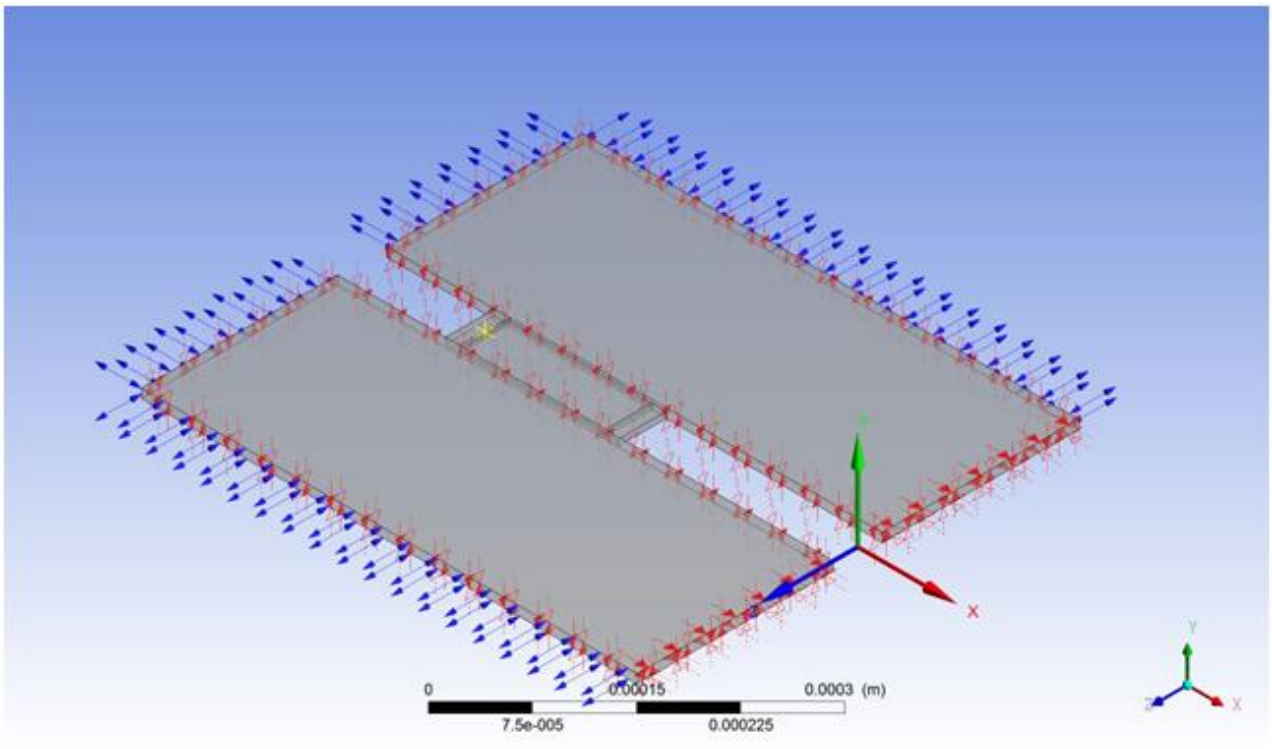

Figure 5.3 Fluid control volume and boundaries

In the Table 5.2 a short summary of analysis identification is provided.

Property	Value
Material	Air
Temperature (no heat transfer)	25 °C
Density	$1.185\ \mathrm{kg/m^3}$
Dynamic viscosity	$1.831 \cdot 10^{-5}\ \mathrm{kg/ms}$
Pressure	1 atm
Flow regime	Laminar
Analysis type	Transient
Velocity amplitude	$0.01\ \mathrm{m/s}$
Oscillation frequency	20,000 Hz

Table 5.2 Analysis's input characteristics

In the analysis results, the shear stress on the surfaces is obtained by integrating shear values over surface of rotor combfinger. This can be done on different surfaces, in order to investigate their contribution to the total force on the finger. These surfaces are names as depicted in Figure 5.4.

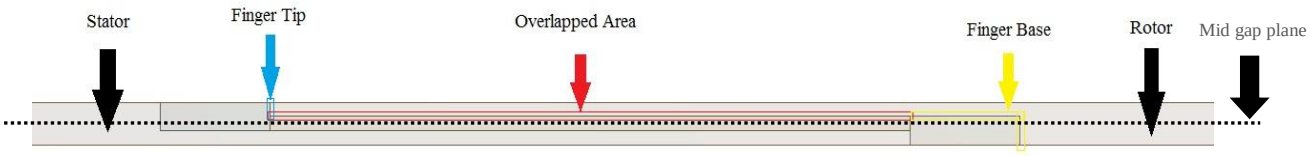

Figure 5.4 Finger Zones

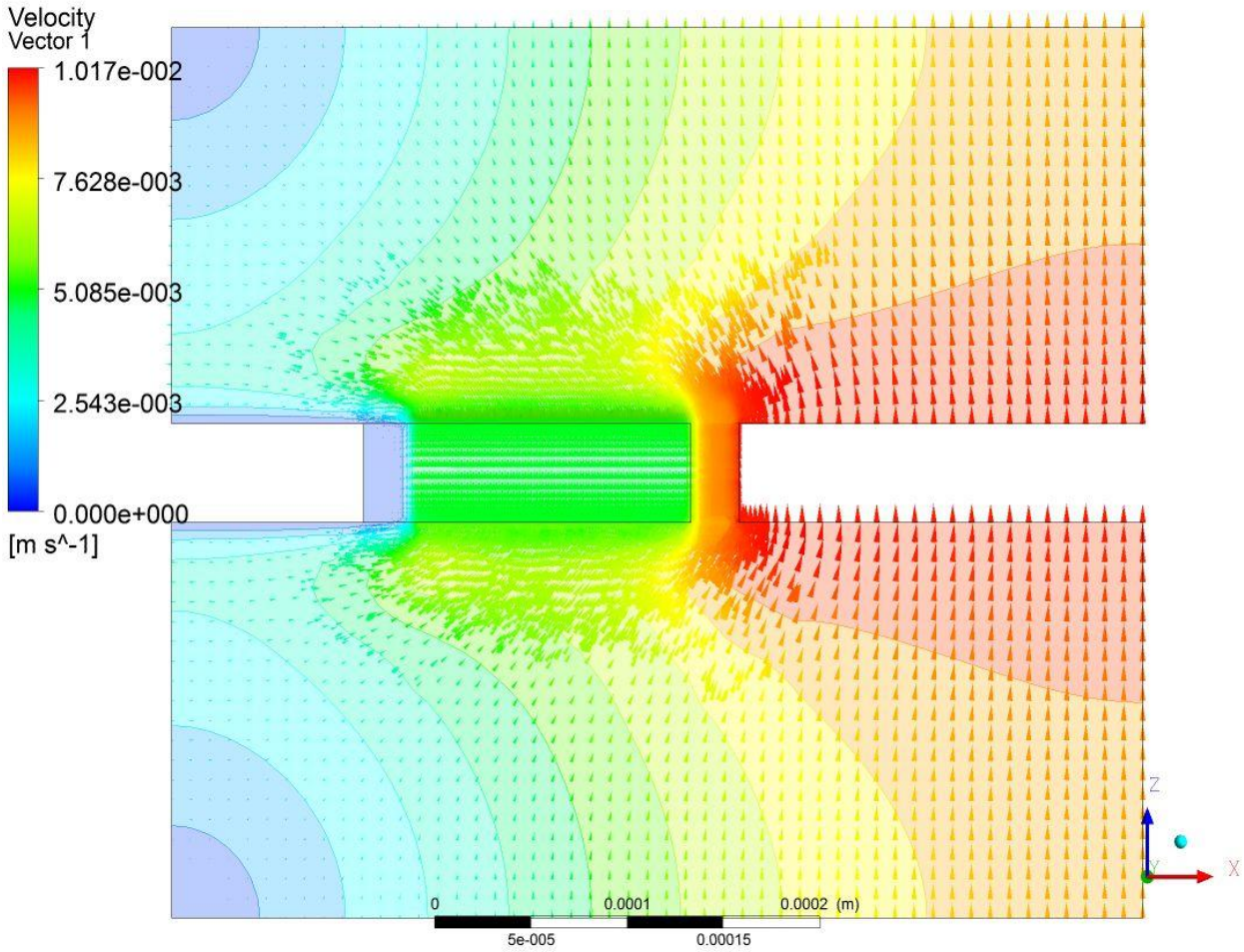

Figure 5.5 Velocity flow field showing on mid gap plane

By extracting the shear forces on the combfinger surface corresponding to a sinusoidal velocity, we show one period of motion in Figures 5.6-5.8. The Couette flow equation is utilized to have an estimation of the results. This analytical solution is just applicable on the overlapped area, in which the Couette flow can be assumed. On the other zones, the flow field is too more complicated to present the force equation in a closed form. The numerical result of force on the overlapped area differs by 2% from the analytical solution, see Figure 5.7. Comparing phases between total shear force and zone by zone, shear force with corresponding velocity, phase difference is obvious in Figure 5.7. This effect has been seen in similar studies ([66] and [67]) on MEMS fluid-mechanical damping phenomena. This phase difference, φ_{lag}, depends on the oscillation frequency and on the geometry. The force can be almost in-phase with the velocity for small frequencies and near to 90° (out-of-phase) for high frequencies. In general, it is noted that the total force has two components: one in phase with the velocity, $F_{\parallel}$ and the other 90^{o} out-of-phase with the velocity, $F_{\perp}$:

$$F_{\parallel} = F\cos(\varphi_{lag}) \tag{5.5}$$

$$F_{\perp} = F\sin(\varphi_{lag}). \tag{5.6}$$

$F_{\parallel}$ contributes into the fluid damping and $F_{\perp}$ does into additional mass loading effect [62]. These two phenomena will result in the resonance frequency phase shift.

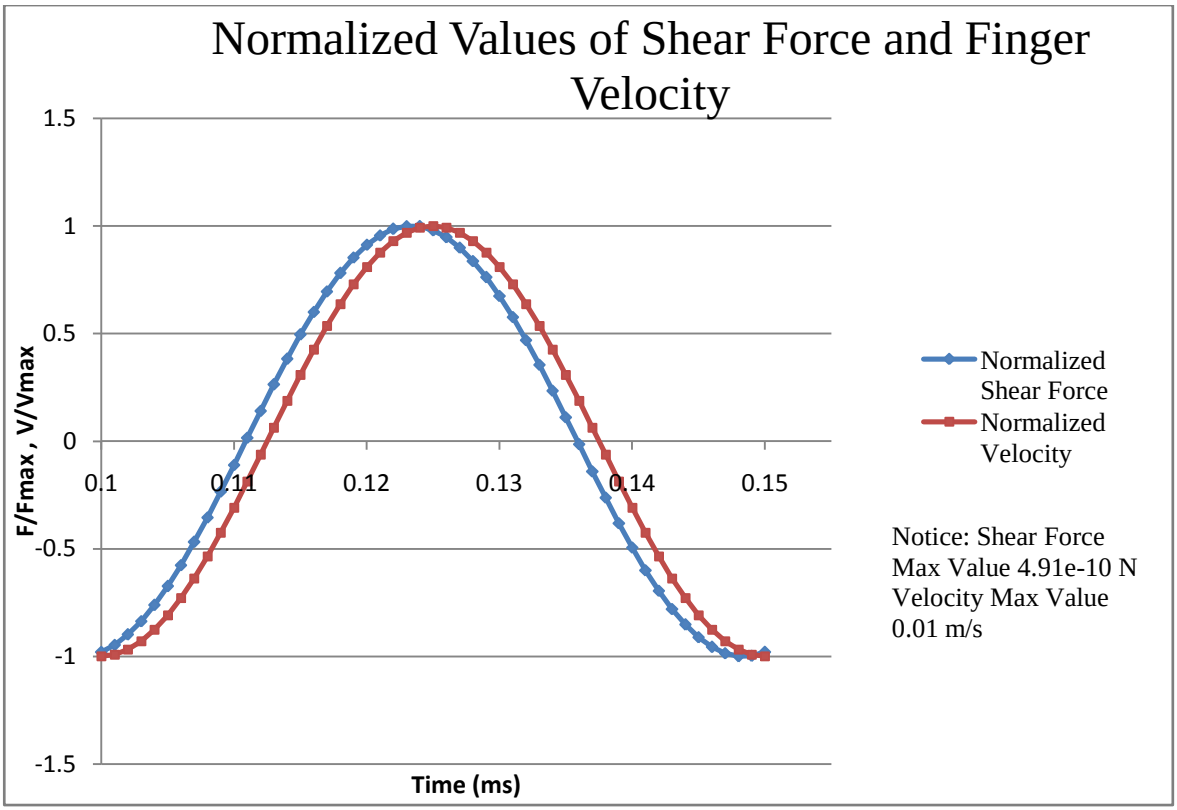

Figure 5.6 Phase comparison between velocity and shear force

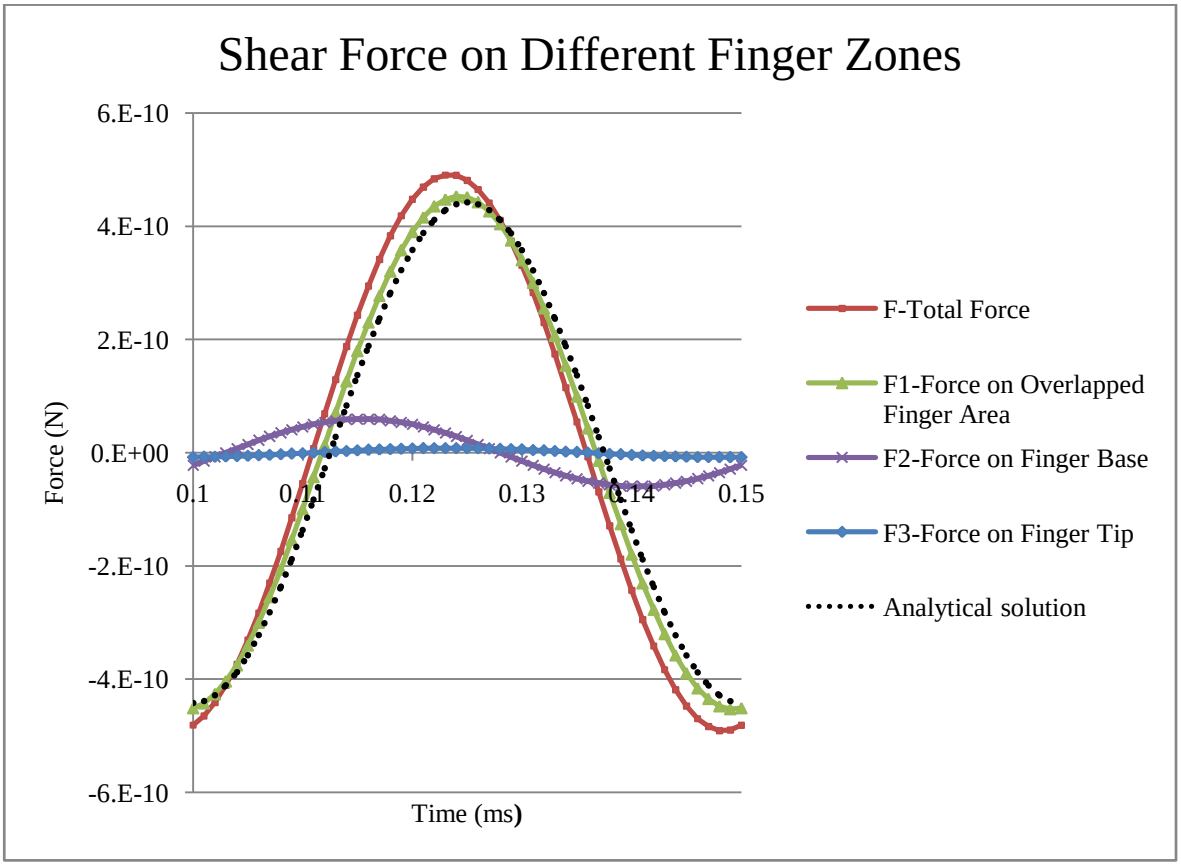

Figure 5.7 Shear Force acting on finger surface showed on different surface zones

Another issue worth of investigation is the effect of the amplitude of displacement or velocity onto the air damping mechanism. The displacement and velocity amplitude are interconnected with a simple time derivative/integral;

$$\left|V\right| = \omega \left|D\right| = 2\pi f \left|D\right| \tag{5.7}$$

where, V is velocity of oscillation; D is the displacement amplitude, ω and f are angular and ordinary frequency of oscillation. Therefore, we conduct the same analysis assuming the geometry parameters and changing the vibration amplitude. Keeping the oscillation frequency constant, the maximum displacement inevitably will change according to the velocity. The problem arisen with high displacements in Lagrangian FEM is a the lack of mesh quality because of mesh distortion; specific methods should be used to face this problem. Here, the analyses are conducted up to a displacement amplitude of $4\,\mu m$ for which the simulation converges.

According to the Couette flow equation, the force is linearly dependent on the velocity magnitude. This fact will be hold till we can assume the overlapping area is almost constant during the oscillation period. This assumption relies on the ratio of maximum displacement to finger width (which is $50\,\mu m$); therefore up to a displacement of $4\,\mu m$ we can hold this assumption satisfied enough.

The analyses are done and total force exerted on the rotor combfinger surface is extracted and is reported in Figure 5.8, as the ratio of force to velocity.

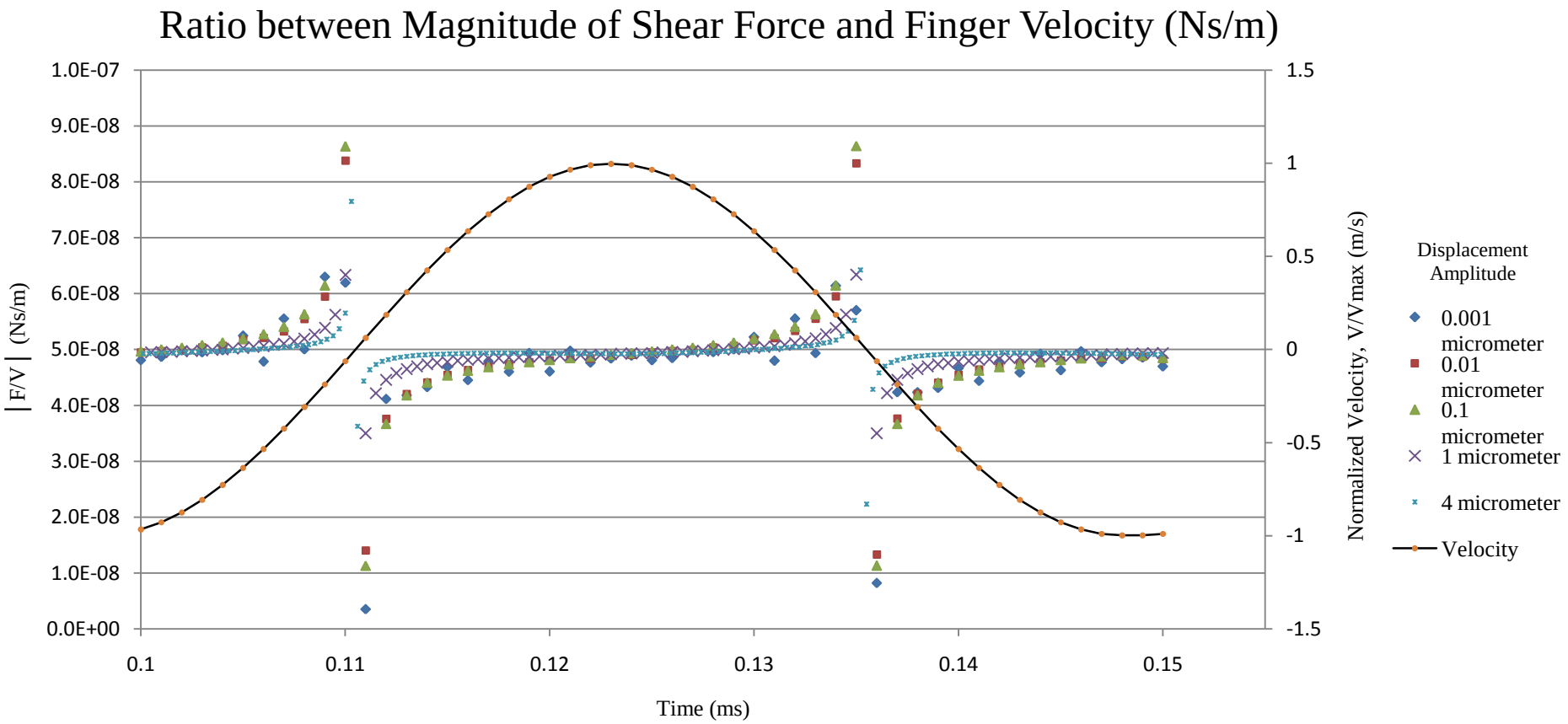

Figure 5.8 Ratio of shear force and imposed finger velocity

From Figure 5.8, the linear behavior of force respect to velocity projects into an almost constant force-velocity ratio. This ratio remains at constant value of $5 \cdot 10^{-8}$ for the most of oscillation period but it shows two jumps. This undesired behavior is due to singularity of division by zero value of velocity that happens twice in a period. As it has been mentioned before, a phase lag exists between force and velocity. To gain the force-velocity ratio, this phase lag should be considered. Because of discretization nature, the number of time steps for solution is limited; consequently the data set of force results cannot be completely in-phase with the time steps data set. This out-of-phase condition even if is minor, does not allow us to get the constant force-velocity ratio all over the oscillation period. Comparing the trend of different displacements in the above diagram shows that for higher displacement we got a finer behavior. The reason is not the higher displacement itself, but rather the finer discretization of time steps; this let us to match the force data set more accurately to velocity data set. It should be noted that this smaller time step is always necessary at higher displacements to get the solution convergence.

5.2 Discussion on the geometry effects

Like any fluid-mechanical problem, the damping forces depend on geometric parameters. To have an optimization of the combfinger geometry, parametric study should be done on the geometry itself. Changing the design, we calculate the damping force and consequently we can get the degree of importance of each geometry parameter separately.

Design prerequisites limit the number of parameters we can modify. In our case, only two parameters are allowed to vary; g, the gap between a pair of rotor and stator combfingers and a, the distance of the finger tip to the front face.

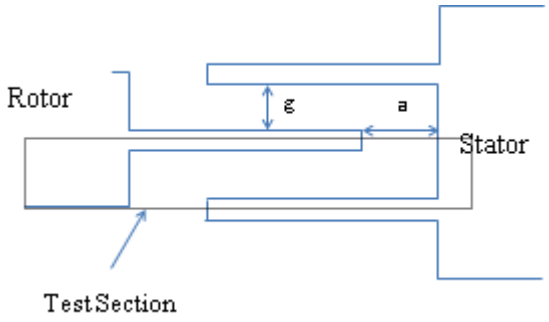

Figure 5.9 Schematic of volume of control

Changing g and a, the rest of geometry keeps the original values reported in Table 3.1. Nine geometry test cases have been defined according to the Table 5.3, in order to conduct the parametric analysis. By choosing $V = 0.01\ \mathrm{m/s}$ and $f = 20000\ \mathrm{Hz}$, the simulation has been repeated for these nine test cases and total shear force on rotor combfingers has been plotted in Figures 5.10 and 5.11:

Test case	a (μm)	g (μm)
1	1	25
2	2	25
3	3 ($Original\ design$)	25
4	4	25
5	5	25
6	3	15
7	3	20
8	3	30
9	3	35

Table 5.3 Different geometry test configurations

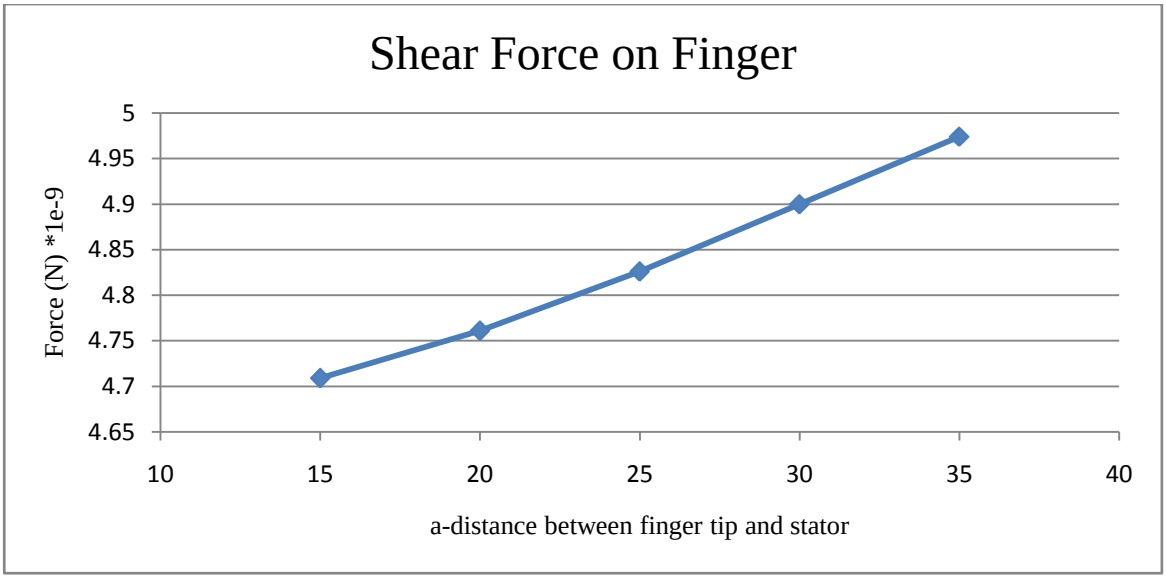

Figure 5.10 Shear force on finger as a function of a

As it can be seen in Figure 5.10, by changing a, the distance between finger tip and stator surface, the magnitude of shear force changes. With increasing a, the finger surface expands and more surface is under fluid-mechanical damping, thus as it is expected the magnitude of force increases almost linearly.

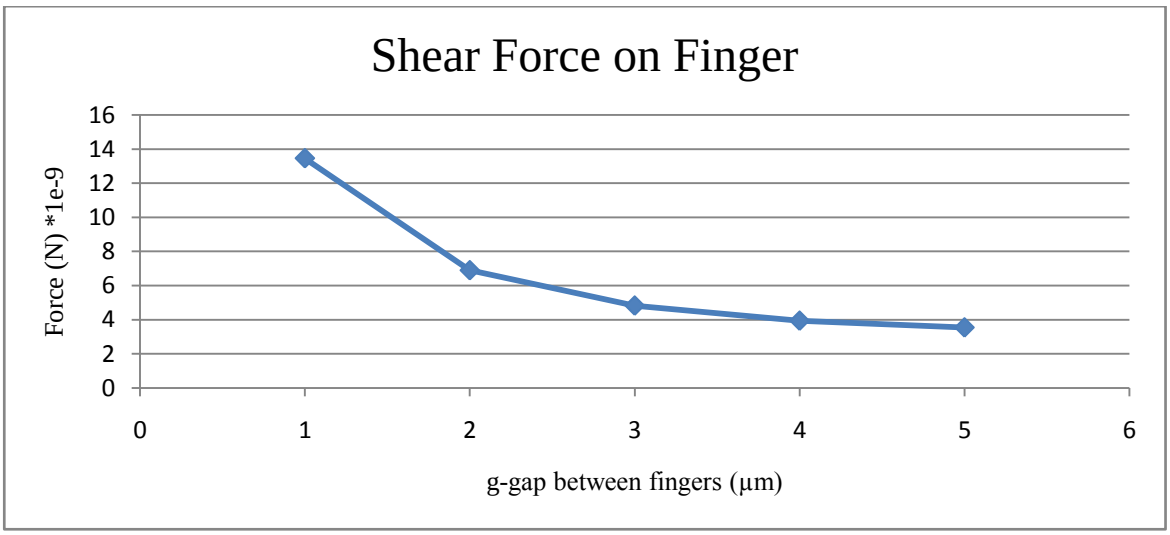

Figure 5.11 Shear force on finger as a function of g

As Equation (5.3) expresses, the damping force is inversely related to the gap size, and this dependency can be seen from Figure 5.11. Comparing the importance of these two parameters, we can emphasize the crucial role of gap in damping mechanism between combfingers.

Again, it is necessary to mention that, the translational motion here is analyzed which in the actual working condition, the mirror is tilting. Therefore, the flow field and consequently the damping forces will be different in these two cases. Later, the motion mode in analysis will be adapted to the actual condition.

5.3 Remeshing

The domain deformation basically causes mesh deformation. To model the domain deformation for small displacements, the mesh should deform. This approach works till the mesh quality targets keep being in satisfactory level. Mesh quality can be evaluated by some parameters such as aspect ratio, minimum orthogonality angle or expansion ratio. In some cases, the problem may be involved with significant mesh deformation lowering the mesh quality below the acceptable level. Periodic remeshing can help to maintain the mesh quality by replacing the old mesh with new mesh. Figure 5.12 shows the overall remeshing procedure in the simulation [30].

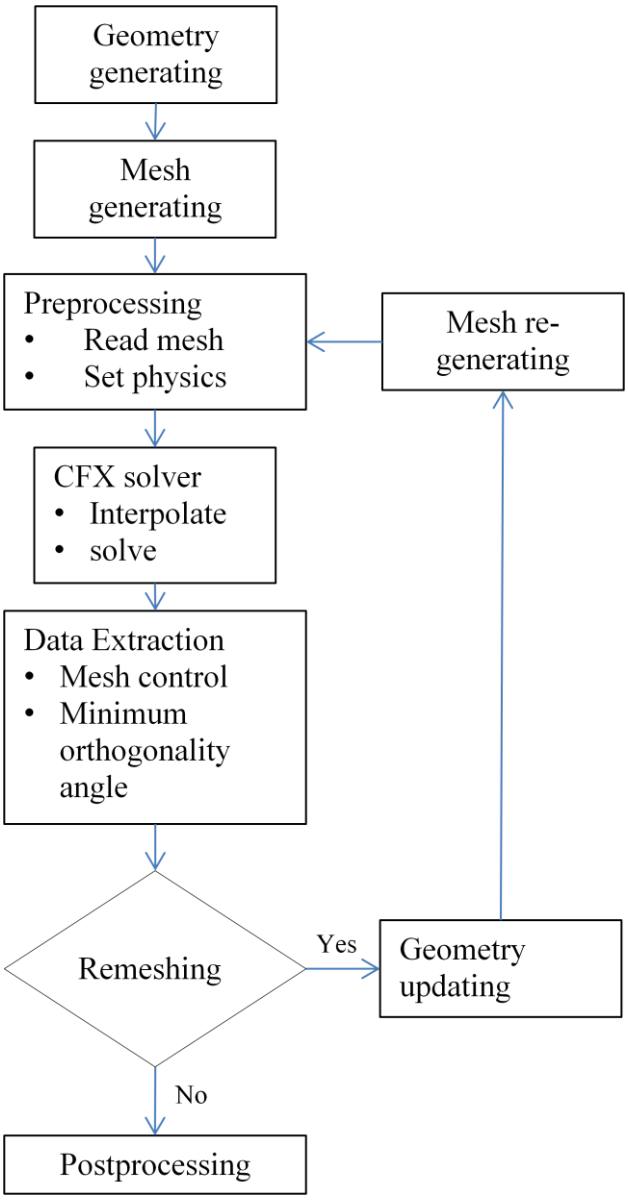

Figure 5.12 Simulation workflow by remeshing for large displacements

As it can be seen, in addition to the ordinary workflow, a remeshing loop is added consisted of three additional steps. These steps are responsible of doing following tasks:

- **Data extraction**: this step extracts the vital information on how to control the geometry and mesh from the last solution step.
- **Geometry updating**: is in charge of updating the geometry in a way that it conforms to the last analysis results. This is done with the geometry control data extracted in the previous step and then the new geometry is sent to meshing step.

- **Mesh re-generating**: generates new mesh corresponding to updated geometry and mesh control data extracted before.

There are two remeshing options in CFX; ICEM CFD replay and user defined. In the first option, all the steps are done automatically but for the latter one, the user should define the three steps of data extraction, geometry updating and mesh re-generating. In Sections 5.3.1 and 5.3.2, these options are described in detail.

5.3.1 ICEM CFD replay remeshing

This option utilizes ANSYS ICEM CFD mesh generation software to provide a simple method for remeshing. The drawback of this method is that it can do remeshing only for translational movements and not for rotational nor arbitrary displacement. To do remeshing, a master replay file is assembled from several task-oriented files and user provided specifications for remeshing. All automatic steps of remeshing for this option can be summarized as below:

- Extract the geometry and mesh control data including centroid displacements of boundaries' centroid, mesh control parameters and scalar parameters [26], and write them into the cfx_params.rpl file.
- Run the ANSYS ICEM CFD mesh generation program using the master replay file, which executes the following tasks in detail:
    - Read the cfx_params.rpl file.
    - Loading the reference geometry file.
    - Apply displacements on the boundaries.
    - Apply the new mesh on the updated geometry through the user-defined replay file for meshing.
    - Export a new mesh to ANSYS CFX.
- Insert new mesh into analysis definition
- Interpolate the results of the most recent solution step on the nodes of new mesh and using them as initial condition of the new solution

The user is required to create the reference geometry file and the mesh replay file specific to each analysis.

5.3.2 User defined remeshing

With this option more flexibility is provided with the expense of writing some executive remeshing scripts or manually doing the remeshing. The automatic steps mentioned in Section 5.3.1, are decreased to:

- Run the specified external command to generate a new mesh.
- Insert the new mesh into analysis definition and generate an updated CFX-Solver input file.
- Interpolate the previously generated analysis results onto the new mesh, repartition the mesh if a parallel run mode is selected and continue the solution process.

5.3.3 Remeshing procedure

Due to complexity of remeshing step, first we tried to obtain it by using the automatic method despite of its limitation to only translational movements. A simple test case was defined including a solid box moving inside an air duct which has two openings at the top and the bottom surfaces.

For implementing this remeshing method, the geometry has been created in ANSYS Modeler and then exported to ICEM CFD to create the first mesh and write the replay file corresponding to the desired mesh. Then, the mesh and the replay file are transferred to ANSYS CFX and the connections between boundaries (in CFX) and geometry in (ICEM CFD) are introduced. Also, an interruption criterion has to be defined to stop the run, and call the meshing software. Here, we used the minimum value of orthogonality angle in the domain as the criterion. The concept of mesh orthogonality relates to how close the angles between adjacent element faces or adjacent element edges are to some optimal angles (e.g., 90^o for quadrilateral faced elements and 60^o for triangular faces elements). The most relevant measure of mesh orthogonality for the CFX-Solver is illustrated in Figure 5.13. It involves the angle between the vector that joins two mesh (or control volumes) nodes shown by *s*, and the normal vector for each integration point surface shown by *n* associated with that edge. Significant orthogonality and non-orthogonality are illustrated at *ip1* and *ip2* [28].

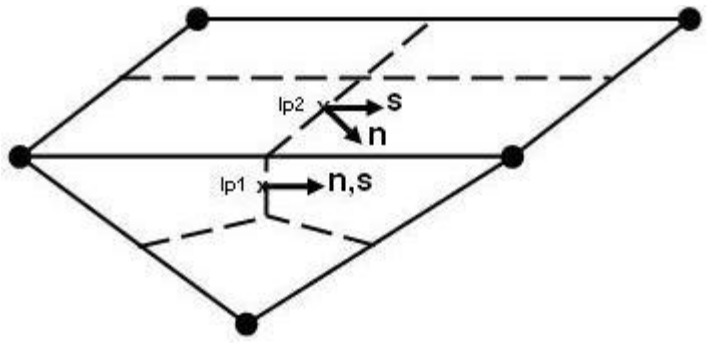

Figure 5.13 Mesh orthogonality measurement [28]

After the remeshing and solution were carried out and by looking at the remeshing result and how the mesh got deformed and was substituted (see Figure 5.14), it appeared that, the new mesh could not follow the moving geometry perfectly and in some edges the mesh penetrated the solid boundary surface. It shows that the links between two softwares did not work well. Despite the effort put on this issue, the problem could not been solved so we implement the other approach: the so-called user defined method. In Figure 5.14, distortion of boundaries is found when following the previous procedure.

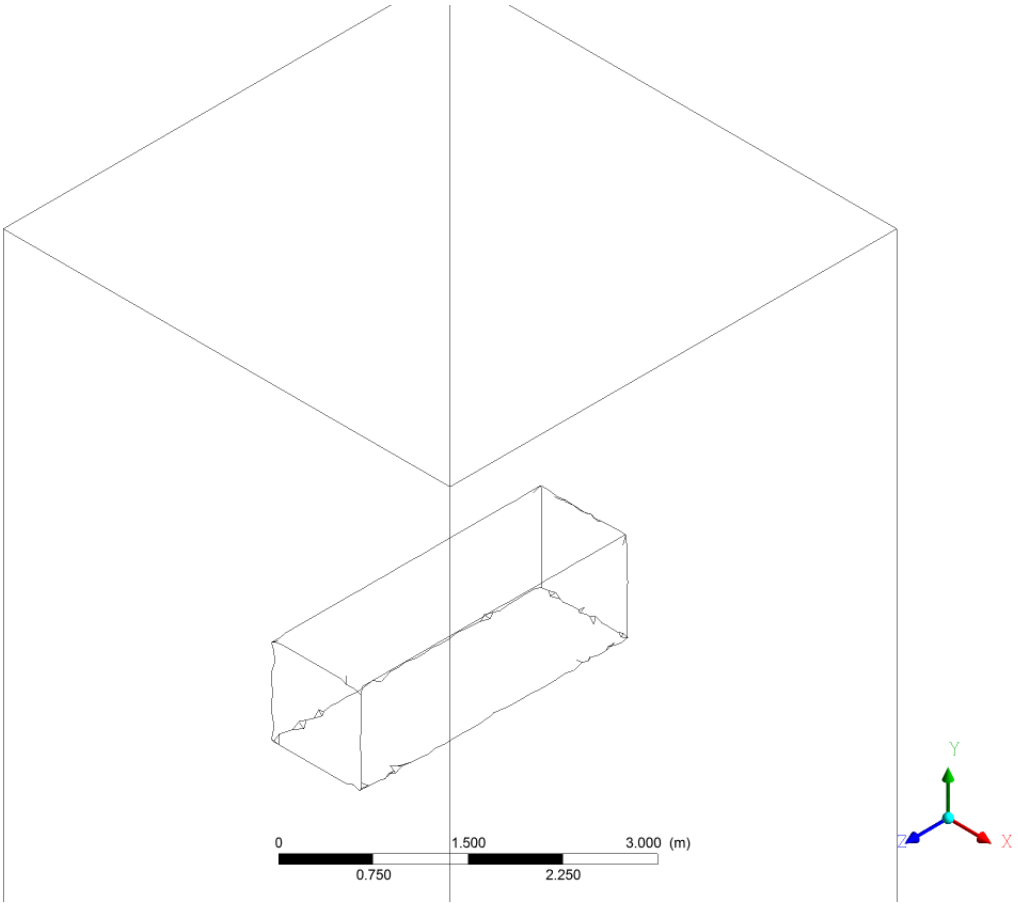

Figure 5.14 ICEM CFD remeshing result

With this second method, the geometry and mesh are both defined in ANSYS Workbench and CFX is applied in a different platform. The geometry is defined in a parametric way, so by editing the parameter, one can update the geometry and, sequentially, the corresponding mesh will be generated. The new mesh will be exported to CFX and the last set of results will be interpolated on the new mesh. This new set of data will be used as the initial condition for the new analysis. This method introduces some errors in the results for each remeshing step due to the interpolation of the results. Therefore, one can see the results' fluctuation at each remeshing, see Figures 5.16-18. Later these jumps can be smoothed out.

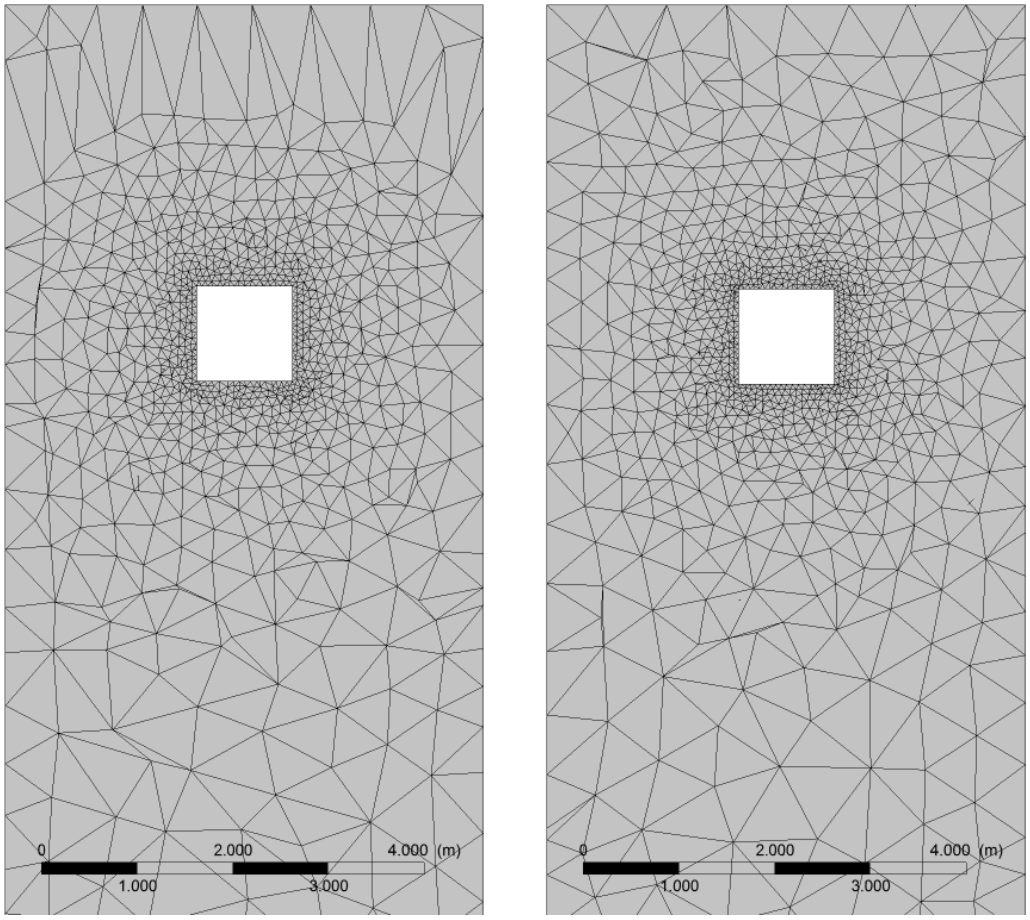

Figure 5.15 User defined remeshing, old mesh (left) and new mesh (right)

To investigate the effect of different options on the remeshing error, some analyses are carried out. The options include the number of time steps for transient solution and the maximum number of iteration for each time step. Figures 5.16-18 show the fluid force on the box while moving downward.

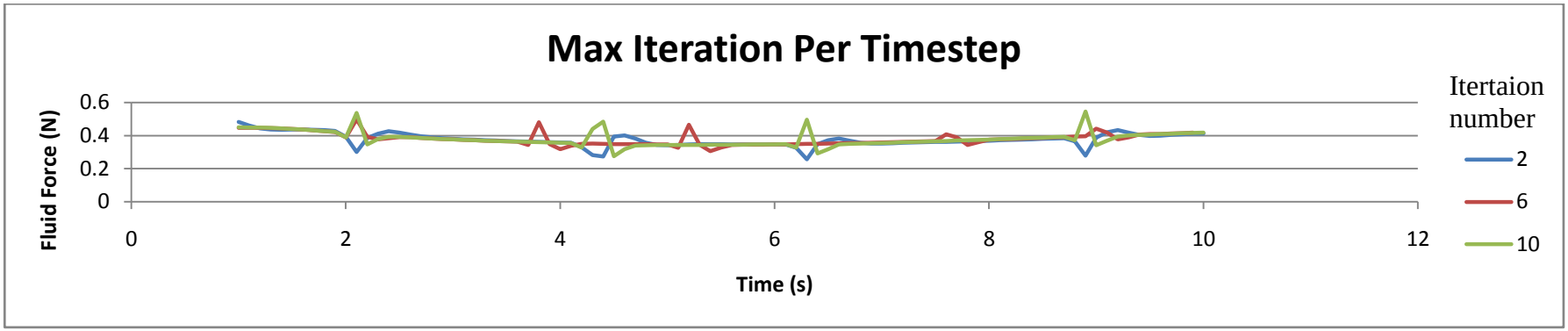

Figure 5.16 Effect of Maximum number of iterations per timestep on fluid force (100 timesteps)

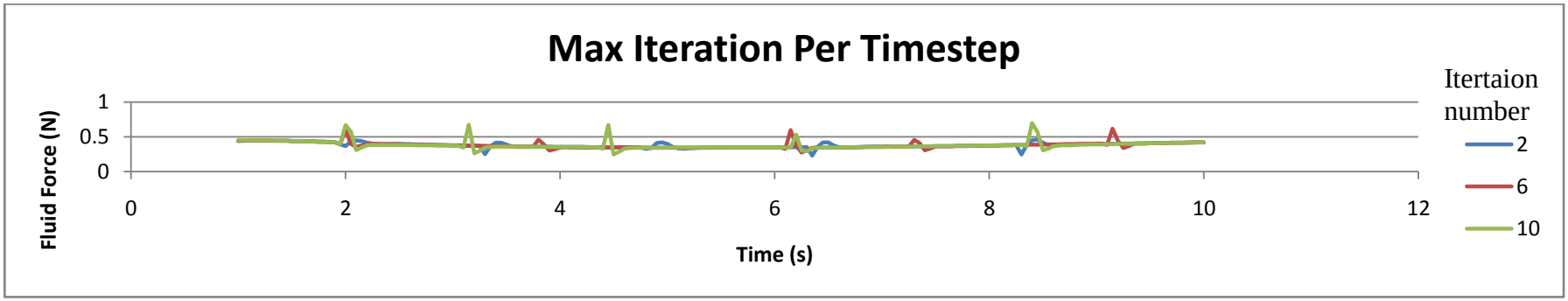

Figure 5.17 Effect of Maximum number of iterations per timestep on fluid force (200 timesteps)

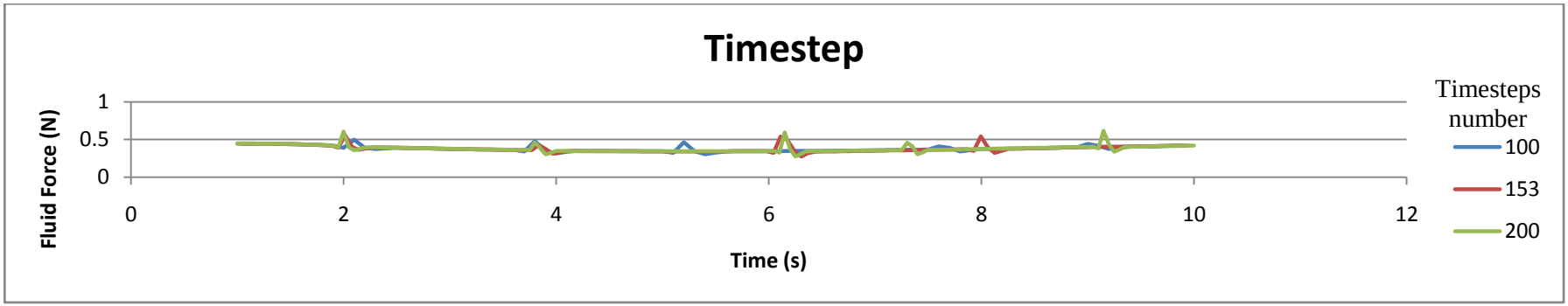

Figure 5.18 Effect of number timesteps on fluid force (6 iterations)

As the Figures 5.16-18 show, these two options affect the results fluctuation: we can decrease the range of fluctuations by changing maximum iteration number and timesteps. At the same time, we have to take the analysis time into account for each analysis. Having other cases and geometries, these parameters should be chosen carefully.

5.4. Lateral oscillation with large displacement

As shown in the previous section showed, a remeshing procedure was adopted for large displacements. First, this method is used for lateral oscillations, translation along *z*-direction. The analysis parameters are chosen similar to what is introduced in Table 5.2. Oscillation amplitude is chosen to be 50 µm which is equal to the thickness of the micromirror; therefore, that the rotor moves upward and downward up to complete disengagement of rotor and stator. Clearly by considering a gap size of 3 µm in comparison to the oscillation amplitude, we expect a huge mesh distortion and, consequently, the need for remeshing.

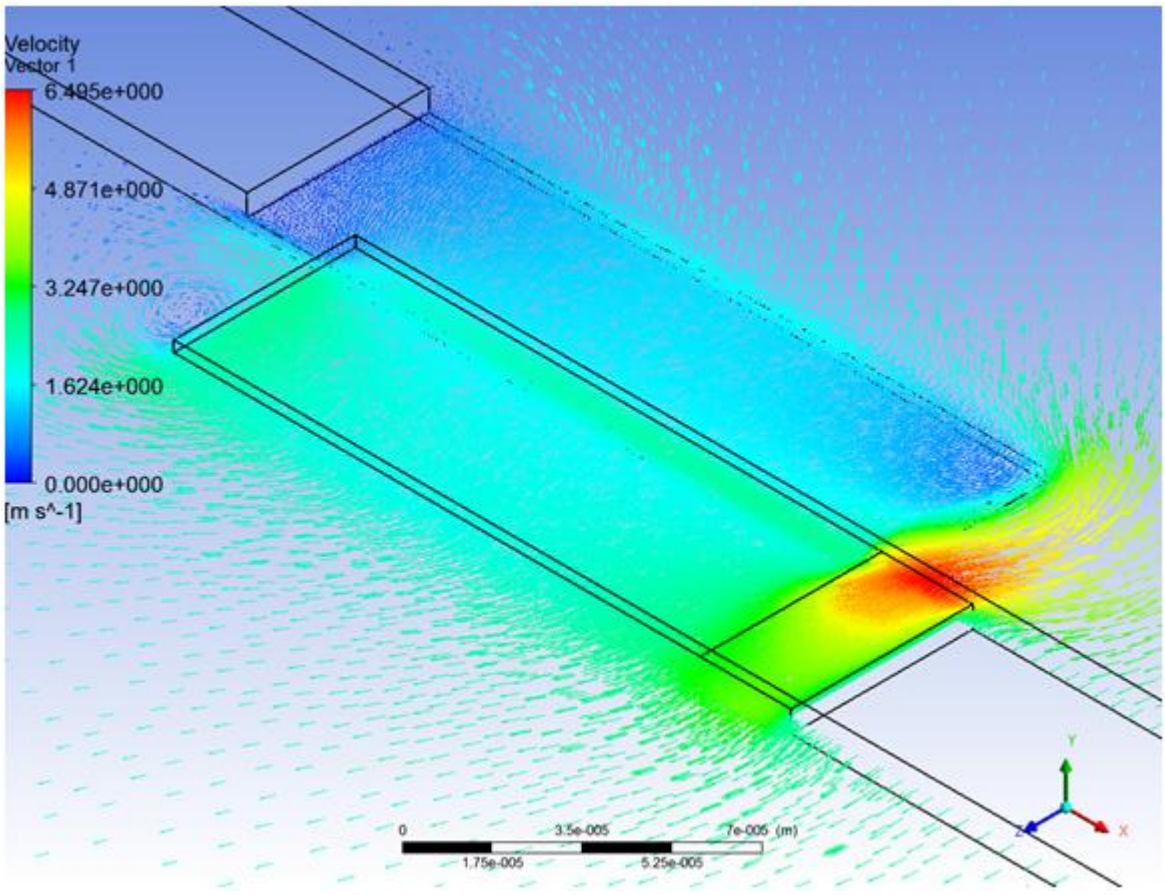

Figure 5.19 Velocity field around combfingers in high amplitude oscillation

Figure 5.19 shows the velocity field around the combfingers in a timestep which the rotor (right side of the figure) is getting disengaged from the stator (left side of the figure). It should be mentioned that, this velocity field may change for other timesteps due to the nonlinear behavior of the flow. By comparing the velocity field here and the one showed in Figure 5.5 corresponding to small amplitude oscillation, the differences in flow formation can be seen especially at the region around the rotor tip and the stator tip. As it had been done for small vibrations in Section 5.1, fluid-induced force on moving combfinger and ratio between the force and oscillation velocity are calculated and presented in Figure 5.20.

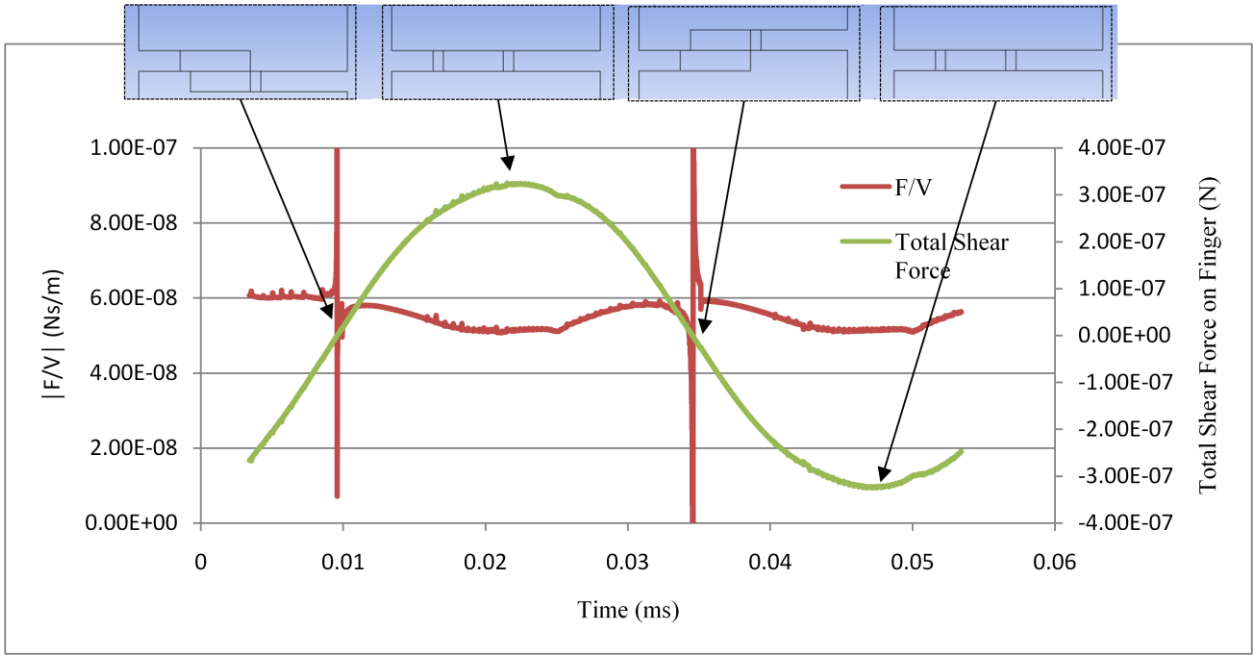

Figure 5.20 Shear force time evolution on moving combfinger, the relative location of combfingers are shown at the top

The evolution of the force has little differences to the cases with small amplitude oscillation. More clearly, the difference can be seen in the force/velocity ratio. In time range when the rotor is passing the fixed combfinger (stator), maximum force happens. In this time range, the overlapped area reaches to its maximum value and the problem resembles to small amplitude oscillations showed in Figure 5.5 which is showing value of $5 \cdot 10^{-8}$. Going over this time range the overlap area decreases and so the force shows lower values but force/velocity ratio grows. Reducing the overlap area basically should reduce the magnitude of shear force on combfinger but we see slight increase in the ratio value. This behavior is due to nonlinear end-effects which get more important as the combfingers disengage and compensate the reducing effect of less overlapping area. A similar observation has

been reported in [58] for a different geometry with finite plates moving. It should be mentioned that high jumps appeared in ratio values due to the same reason explained for Figure 5.5.

To have more insight into the importance of end-effect at high amplitudes, some other configurations are considered. By analyzing these configurations, we are providing more understanding on the force imposed on the combfinger, when it goes from the complete engaged condition toward the complete disengaged condition. The combfinger oscillation is set to the low amplitude of 1 µm but so that the rest position of oscillation varies between values of $d_c = 0, 50, 60, 100$ µm. d_c indicates the distance between centreline of the fixed and moving combfinger. Later the fixed combfinger is removed and just oscillation of rotor in air is studied. Figures 5.21-22 illustrate these two test cases.

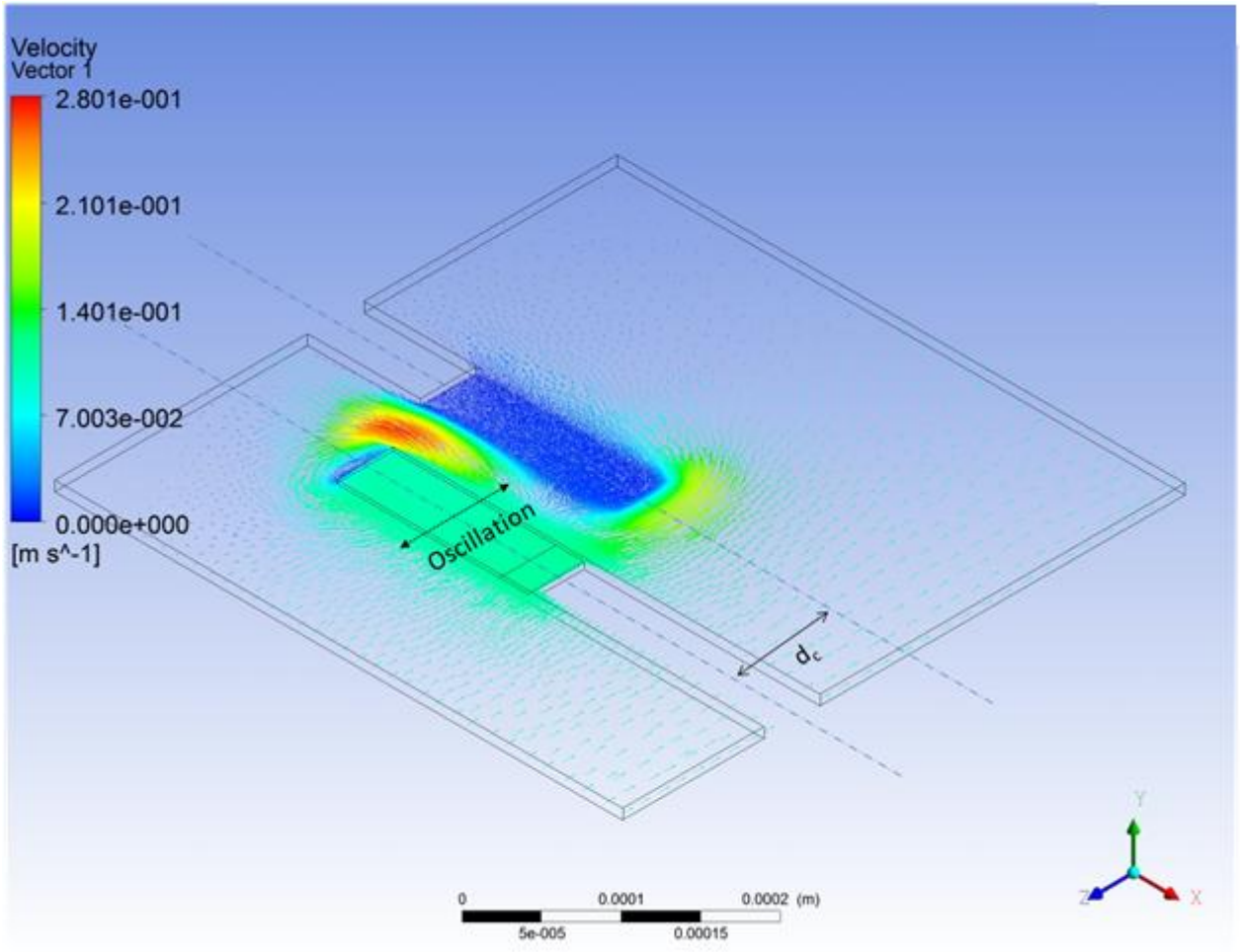

Figure 5.21 *Analyses with dislocated combfinger*

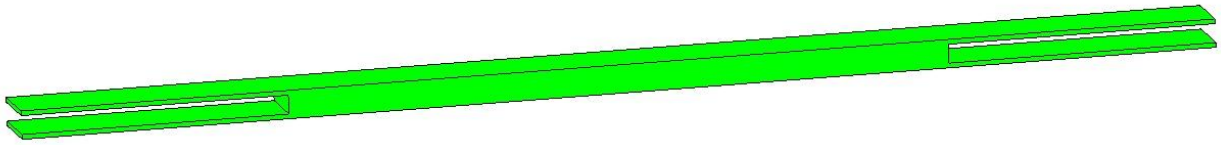

Figure 5.22 Moving combfinger in absence of fixed combfingers (No Stator configuration)

Shear forces exerted on combfinger by air in all the cases are presented in Figure 5.23.

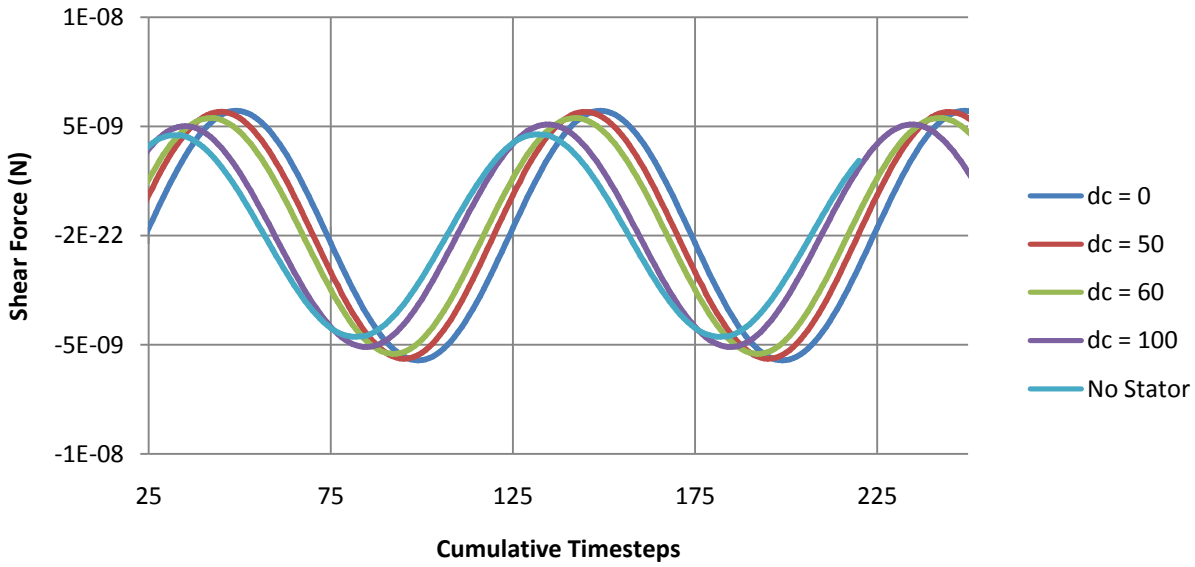

Figure 5.23 Shear forces time evolution on finger in different configurations

It can be seen that the end-effect contribution to the total shear force is not negligible. Especially this is dominant in oscillation of rotor in absence of the stator. This effect is also dependent to frequency and apparently in our chosen frequency of $20{,}000\ Hz$ has a significant effect.

5.5. Large angle tilting

Target design for the micromirror is a tilting movement up to $\pm\ 12^{o}$. At this angle, the combfingers are almost disengaged, see Figure 5.24. Similar to the large displacement lateral oscillation, the remeshing mechanism should be used in model. Due to tilting of combfinger, fluid travels between the two sides the

combfingers arrays and the symmetry boundary condition cannot be used as all the previous cases. Another minor difference here is the oscillation frequency set to 19,343 Hz as it is the frequency at which the actual micromirror works. Although remeshing is utilized in this simulation, tilting combfinger at high degrees produces mesh deformation resulting in simulation failure. This problem asks for special care on remeshing parameters and very fine timesteps. Timestep is chosen $3 \cdot 10^{-8}$ s which means discretiziation of each period of vibration into 1,725 steps of motion. Also, lack of symmetry condition for tilting oscillation doubles the number of elements and, therefore, the simulation time increases notably up to 15 hours for one period. A quad-core Intel Core i7 processor with 3.40 GHz and 16 GB of RAM was used for the simulation.

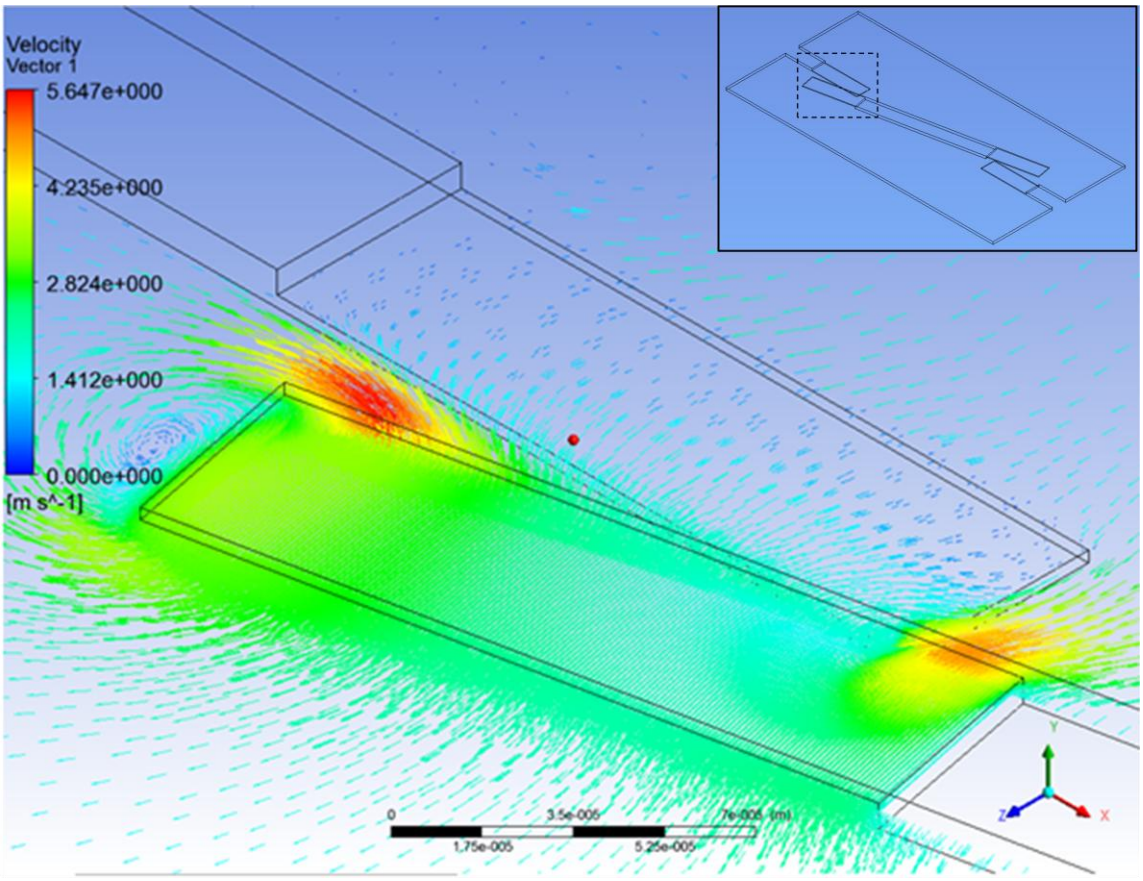

Figure 5.24 Velocity field between combfingers in tilting mode (dash line showing the combfingers region in the model)

A transient analysis for this configuration is carried out and the fluid fields for several periods are extracted. In Figure 5.24 an arbitrary timestep is chosen to

show the characteristics of flow field. In this timestep the rotor is tilting counter-clockwise. Once again, it should be point out that, due to nonlinear end-effects in large motions, the flow field for other timesteps might differ.

By integrating the shear forces values and corresponding distance from the rotation axis, the fluid torque resisting the rotor combfinger motion is achieved over time domain. These values are presented in Figure 5.25. As it can be seen, torque exhibits a periodic profile but not with a sinusoidal form. Maximum torque is corresponding to zero degree of tilting in which rotor and stator combfingers share the maximum overlapped surface. Large tilting angle effect can be observed in two sides of each torque peak. On left side of the peak, the rotor combfinger enters the gap between stators (engagement phase), but on the right hand, it leaves the gap (disengagement phase). Therefore, torque in these two phases is not identical. Remeshing mechanism happens numerously during this analysis. In each remeshing step, the last geometry and results were extracted. Then, the old mesh is replaced by the new mesh obtained with the new geometry. By interpolation of last set of results, the initial condition for the new run was provided. Interpolation procedure inevitably introduces errors in simulation. These errors appear in the form of fluctuations as it is shown in the zoom view of Figure 5.25.

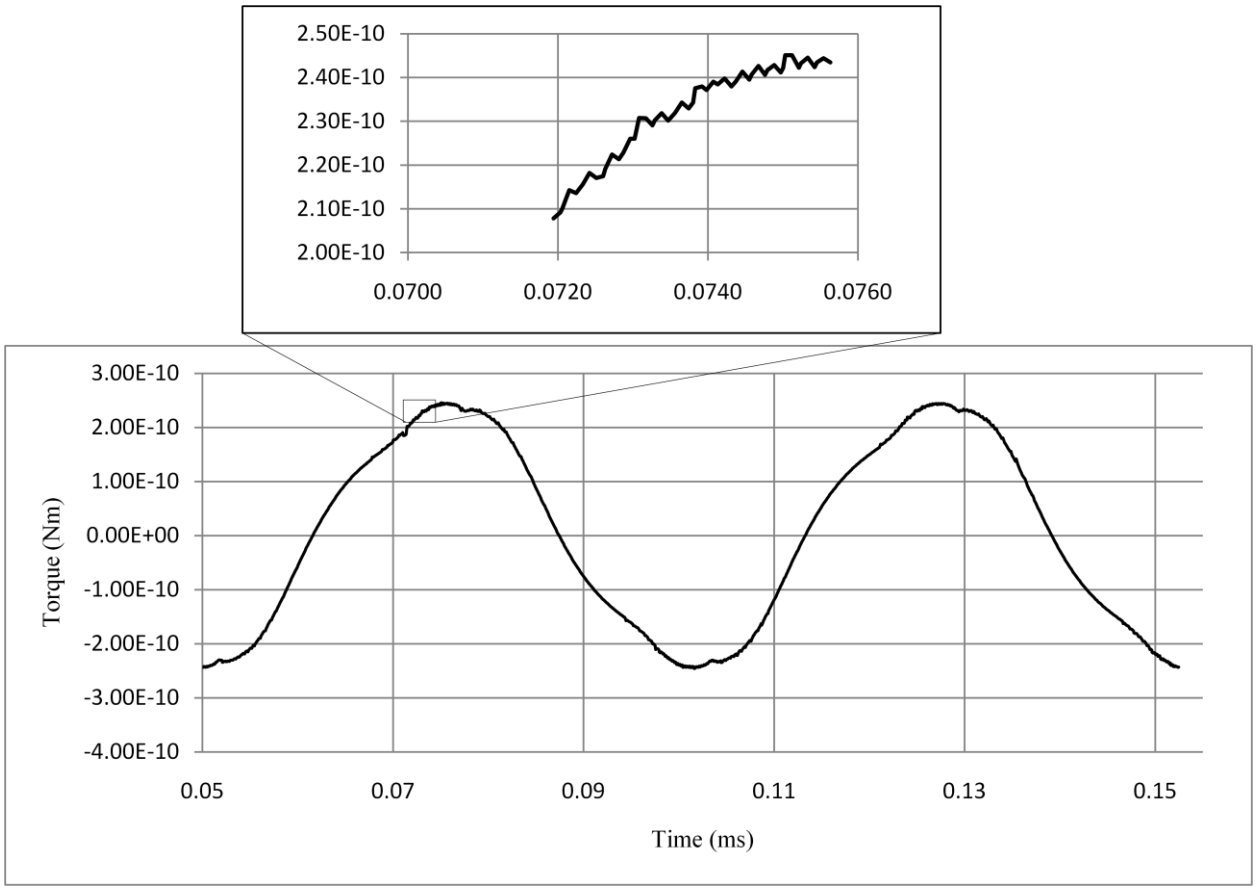

Figure 5.25 Imposed torque by air on combfinger

Another important portion of energy dissipation occurs in mirror plate by drag forces. This issue has been studied in another simulation by modeling the main body of micromirror. In this simulation the arrays of combfingers are neglected due to complexity of mesh and simulation convergence. Transient simulation of the oscillating combfinger is carried out in the same operational frequency but with tilting angle of 1^{o} to avoid remeshing. Figure 5.26 shows a sample of pressure contour and velocity field.

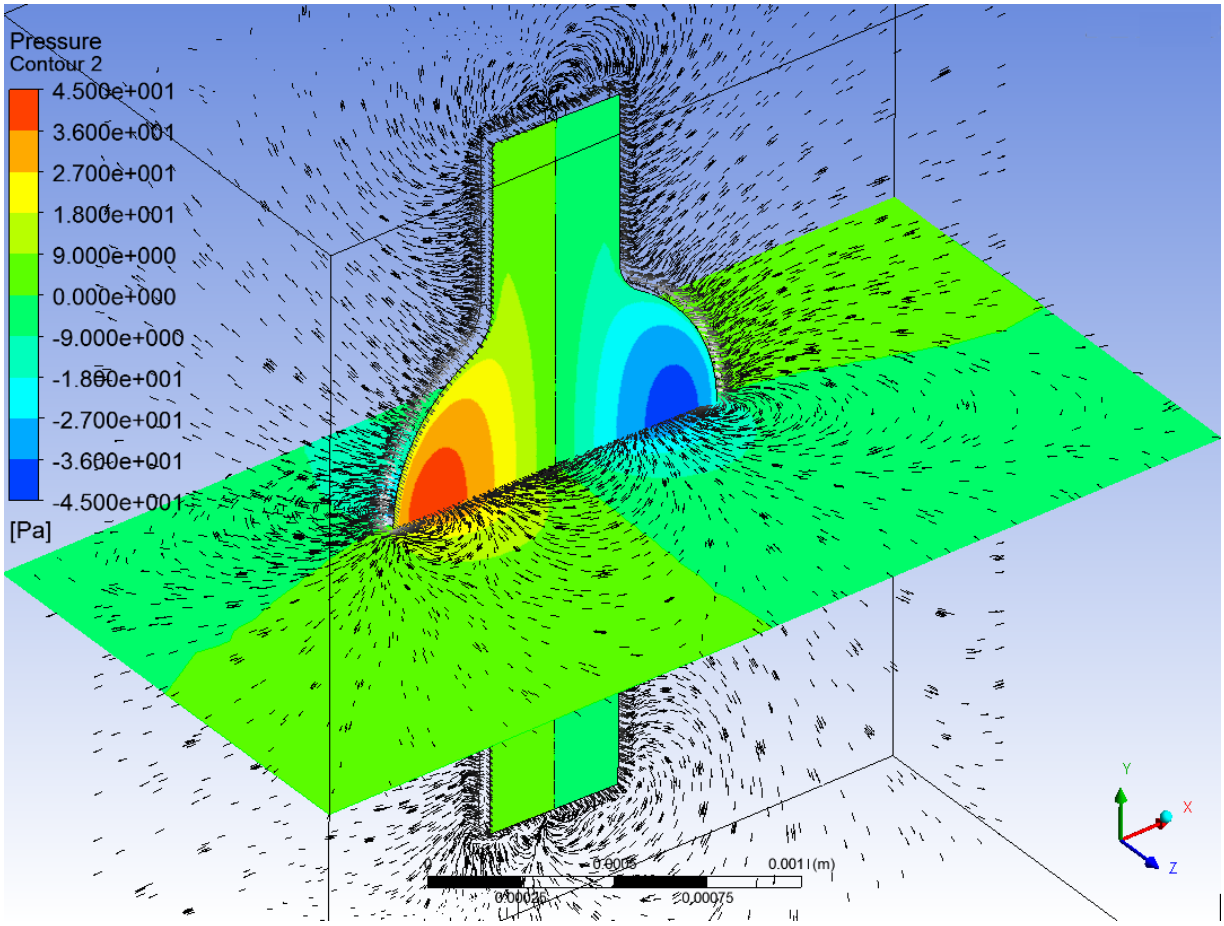

Figure 5.26 Drag damping simulation, pressure contour and velocity field around tilting micromirror

Squeeze damping's importance can be also evaluated by deriving the torque values over the top and bottom surface of micromirror. Deriving these values for several periods, Figure 5.27 gives details of drag torque on the structure. The micromirror is placed 450 µm above the substrate. In Figure 5.27, imposed torque on the top and the bottom surfaces are illustrated separately and they show close values. Therefore, we can certify our previous assumption on negligible effect of squeeze damping in the problem in hand.

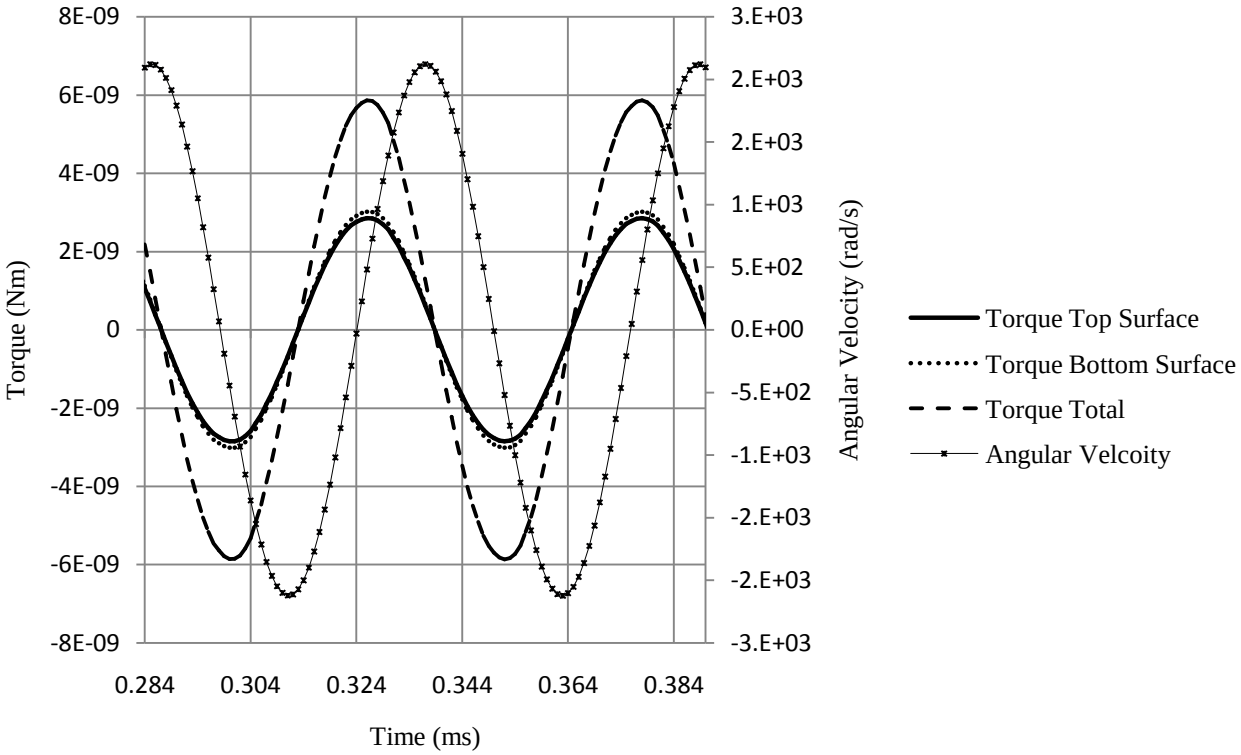

Figure 5.27 Damping torque on micromirror.

5.6 Quality factor

Quality factor can be evaluated by the definition of the energy performance of an oscillatory object as [2]:

$$Q = 2\pi \frac{E_{st}}{E_{loss}} \tag{5.8}$$

In Equation (5.8), energy loss refers to all kind of energy losses in the system, so by accounting for the combfinger loss only, we can evaluate the quality factor regarding this loss. This loss should be calculated on over a period of oscillation for the array of combfinger as:

$$E_{loss} = N \int_{period} T\dot{\theta} dt \tag{5.9}$$

where, N is the number combfingers, T is the resistive torque and $\dot{\theta}$ is the angular velocity. Stored energy is available for torsional motion of the micromirror as follows:

$$E_{st} = \frac{1}{2} I_{yy} \dot{\theta}_{max}^2 \tag{5.10}$$

in which I_{yy} is mass moment of inertia of the micromirror about its rotation axis and $\dot{\theta}_{max}$ is amplitude of angular velocity. Density of silicon, as it was mentioned in Section 3.2, is $\rho = 2.33\ \mathrm{gr/cm^3}$. Utilizing ANSYS to extract the micromirror geometrical characteristics, the value of I_{yy} is obtained as $9.3838 \cdot 10^{-15}\ \mathrm{kgm^2}$. From Equations (5.8-10), the quality factor by energy loss of the combfinger is evaluated as $Q = 1{,}074$.

To calculate the quality factor corresponding to the micromirror drag, we can still use Equations (5.8-10). Energy loss is the sum of the work done by the drag torque, which is a sum of pressure forces and friction forces on the micromirror surface. This torque experienced by an oscillating body is not automatically equal to the damping torque, which actually leads to a loss of energy in the oscillating systems. Fluid inertia and compressibility induce a phase shift $\Delta\varphi$ between oscillation velocity and the drag torque. Calculating the energy loss over a period of oscillation, it follows that the energy is dissipated only by the part of drag that is in-phase with oscillation velocity. The phase shift can be only get from a CFD analysis. Value of $\Delta\varphi$ is obtained as $\Delta\varphi = 1.337$ rad from Figure 5.27. Thus, Equation (5.8) gives a quality factor of 1,754 by the micromirror drag dissipation.

The relation between total quality factor, Q_{tot} , and each quality factor component is given by [65];

$$\frac{1}{Q_{tot}} = \sum_i \frac{1}{Q_i}. \tag{5.11}$$

As Equation (5.11) indicates the overall quality factor will be a lower value from all the quality factors we have got separately. What we obtained for fluid-mechanical damping happening in combfingers is the dominant energy loss effect. So adding micromirror drag quality factor leads us close to the experimental results.

Putting the quality factors achieved for dissipations in combfinger and micromirror drag and using Equation (5.11), the total quality factor is obtained as $Q = 672$.

The micromirror manufactured by STMicroelectronics is expected to operate with the quality factor between 500 and 800. Test setup has been prepared, and frequency response is obtained and shown in Figure 5.28.

The behavior of the device when the input frequency is steadily increasing or decreasing, is significantly different. By sweeping frequency for higher values, the system does not resonate. We need to actuate the system by decreasing the frequency to get the desired resonance. The force induced by the actuator is both time and displacement dependent. The dynamic behavior of the micromirror is called parametric resonance, and is due to this relatively complicated nature of the forcing function [76].

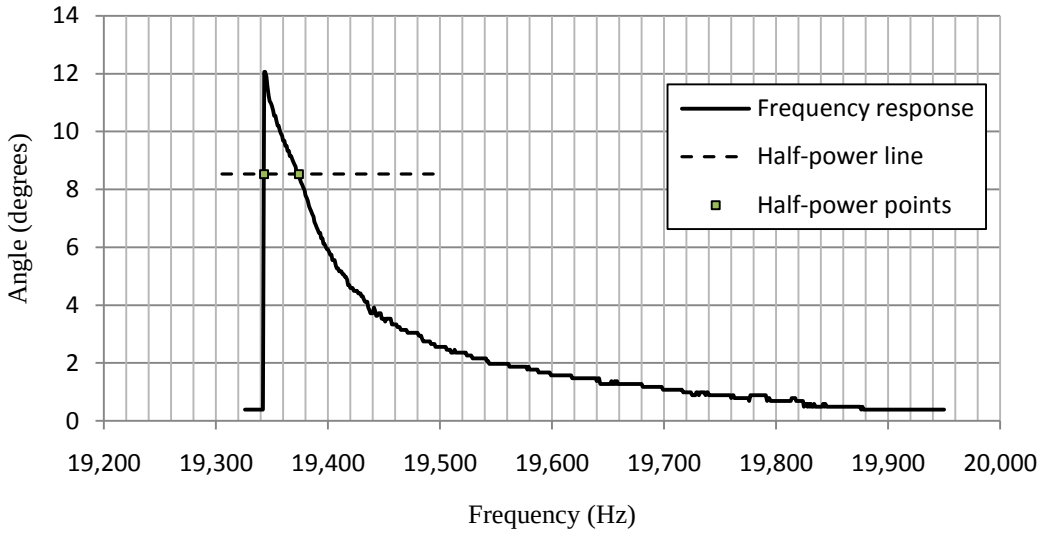

Figure 5.28 Dynamic response of the reference micromirror

At frequency $f = 19{,}343$ Hz, the resonance occurs. To derive the quality factor from Figure 2.8, we use the half-power bandwidth (HPB) formula. Let f_n denote the resonant frequency and f_1 and f_2 denote the half-power frequencies, where the amplitude of the oscillation is $1/\sqrt{2}$ times the resonant amplitude. Then, quality factor Q is expressed by [38]:

$$Q \approx \frac{f_n}{f_2 - f_1}. \tag{5.12}$$

By Equation (5.12), the value of quality factor is obtained $Q = 623$.

The simulation shows higher value for quality factor of the micromirror in comparison to the experiment. This difference between the values can be explained by the assumptions in the simulation of drag damping. By neglecting the combfingers in the last model for extracting the drag damping, we overlook the portion of dissipation occurring at combfingers. Even though the surface area of combfingers is not comparable to the one of micromirror, it is still a source of dissipation and by neglecting it, we are overestimating the quality factor value. Another source of error is the oscillation amplitude (tilting angle) in the last simulation. As previously at the end of Section 5.5 mentioned, the squeeze film damping is negligible (see Figure 5.27). This effect increases at bigger values of the tilting angle; consequently quality factor reduces. To evaluate this effect for tilting angle $\theta = \pm 12^{o}$, we need to adopt the remeshing method for simulating the micromirror drag damping. We have not conducted this last step of the simulation, and left it for future research activity.

To have an overview on this chapter, we have investigated the fluid-mechanical damping mechanisms, specifically the shear damping occurring in the combfingers. Transient simulations to extract damping force/torque have been conducted. Through these simulations, we have shown the geometry parameters' effects on the shear damping occurring in the combfingers. Then, combining the quality factor corresponding to combfinger damping and drag of the micromirror, an overall quality factor has been derived and compared with the experimental results.

Chapter 6

Conclusion

6.1 Outline of main results

The overall aim of this thesis was to provide MEMS producers with a numerical tool for the design optimization of resonating micromirrors. To pursue this objective, we divided the work into two parts.

First, we investigated the resonance frequency of a device. A numerical simulation for computing the frequency has been done by ANSYS Mechanical APDL. It has been enhanced by considering the effect of residual stress in the modal analysis, which has been observed in fabricated samples by STMicroelectronics. Through applying a virtual thermal load, it has been shown that the residual stresses do not change the resonance frequency of the torsional mode significantly. Then, the harmonic response analysis has been adapted, taking account of the micromirror and air coupled. In this analysis, the fluid structural interaction (FSI) has been modeled by coupling the pressure of air domain with displacement degrees of freedom (DOFs) of the nodes on the fluid-structure interface. We have shown that the micromirror operating in air has lower resonance frequency, than those operating in vacuum.

In the second part, we have focused on the fluid-mechanical damping. First, analytical one-directional steady flow between two parallel plates has been solved with the conventional (stick) and the slip boundary conditions. Then, the dynamic shear driven air flow between two oscillatory parallel plates has been solved accounting for both the boundary conditions. The corresponding damping coefficient, as a function of the oscillation frequency, is obtained. The damping coefficient shows constant value up a corner frequency, and then increases at a constant rate. It has been shown that the continuum model, along with the conventional boundary conditions is amenable for the reference micromirror with errors lower than 5% in the fluid-mechanical forces.

A pair of the rotor and stator combfingers has been modeled by CFX and the fluid-mechanical dissipation in small and large angle oscillations has been then investigated. By obtaining the temporal evolution of torque/force opposing the

combfinger rotation/motion, a comprehensive understanding of the dissipation has been achieved. CFX results for small oscillation are in good agreement with Couette flow model. For the large angle oscillations, it has been shown that, despite of the complete disengagement of combfingers, because of the end-effect non-linearities, the damping torque remains considerably high. This fact has been illustrated at the combfingers engagement and disengagement phases individually, and it has been concluded that the former has greater dissipative effects than the latter. The quality factor has been then computed for the fluid-mechanical dissipation in the combfingers.

Also, the drag damping of the tilting micromirror surface has been simulated, and the corresponding quality factor has been obtained. By combining the individual quality factors, the overall one has been computed and shown to be in a fairly good agreement with the available experimental data.

6.2 Future works

Capability of CFX for simulating the squeeze damping in micro systems has been shown in this work. By performing the drag damping simulations for large rotational angles, we might get a better understanding of all the fluid-mechanical damping effects occurring in the micromirror. Another enhancement of this work may be the analysis of the electro static field, and resultant actuation torque by considering the fringe field effects. Coupling the results of these two simulations can give us a compact model of the micromirror dynamics in case of very strong torsional oscillations.

Acronyms

FSI	Fluid Structural Interaction
DOF	Degree of Freedom
TMAC	Tangential Momentum Accommodation Coefficient
MEMS	Micro-Electro-Mechanical Systems
MOEMS	Micro-Opto-Electro-Mechanical-Systems
MOPOS	Micro-Optical-Positioning Systems
IC	Integrated Circuit
DLP	Digital Light Processor
RSD	Retinal Scanning Display
OXC	Optical Cross Connect
FEM	Finite Element Method
CFD	Computational Fluid Dynamics
SATP	Standard Ambient Temperature
CEL	CFX Expression Language
BC	Boundary Condition
RAM	Random-Access Memory
HD	High-Definition
VGA	Video-Graphics-Array

Bibliography

[1] M. Gad-el-Hak, “The fluid mechanics of microdevices”, The Freeman scholar lecture, Journal of Fluids Engineering, p. 121, 1999.

[2] E. Bertarelli, “BioMEMS for microscale fluid transport: design, simulation and prototyping” PhD dissertation, Politecnico di Milano, p. 8-9, 2011.

[3] W. Ko, “Trends and frontiers of MEMS”, Sensors and actuator A: physical, volume 136, p. 62-67, 2007.

[4] A.Q. Liu, X. M. Zhang, “A review of MEMS external-cavity tunable lasers”, Journal of micromechanical and microengineering, volume 17, p. R1-13, 2007.

[5] C. Lee, J.A. Yeh, “Development and evolution of MOEMS technology in variable optical attenuators”, Journal of micro/nanolithography. MEMS MOEMS, volume 7, p. 21-24, 2008.

[6] A.Q. Liu, X.M. Zhang, V.M. Murukeshan, X. Zhang, Q.B. Zou, S. Uppili, “An optical crossconnect (OXC) using drawbridge micromirrors”, Sensors and actuators A: physical, volume 97-98, p. 227-238, 2002.

[7] H. Toshiyoshi, H. Fujita, “An electrostatically operated torsion mirror for optical switching device”, Proceedings of the 995 international conference on solid-state sensors and actuators (Transducer ‘99), volume 68-B1, p. 297-300, 1995.

[8] H. Toshiyoshi, D. Miyauchi, H. Fujita, “Electromagnetic torsion mirrors for self-aligned fiber-optic cross connectors by silicon micromachining”, IEEE Journal of selected topics in quantum electronics, volume 5, p. 10-17, 1999.

[9] W.H. Juan, S.W. Pang, “High-aspect-ratio Si vertical micromirror array for optical switching”, Journal of microelectromechanical systems, volume 7, p. 207-213, 1998.

[10] U. Baran, D. Brown, S. Holmstrom, D. Balma, W.O. Davis, A. Mazzalai, P. Muralt, H. Urey, “High frequency torsional MEMS scanner for displays”, Proceeding of 25th annual IEEE MEMS, Paris, France, p. 636-639, 2012.

[11] C.H. Manh, K. Hane, “Vacuum operation of comb-drive micro display-mirrors”, Journal of micromechanics and microengineering., volume 19, p. 105-113, 2009

[12] P.F. Van Kessel, J. Hornbeck, R.E. Meier, M.R. Douglass, “A MEMS-based projection display”, Proceedings of the IEEE , volume 86, issue 8, p. 1687-1704, 1998.

[13] H. Urey, “Retinal Scanning Displays”, Encyclopedia of optical engineering, Marcel-Dekker, 2003.

[14] H. Urey, D.W. Wine, J. R. Lewis, “Scanner design and resolution tradeoffs for miniature scanning displays”, SPIE proceeding of conference on flat display technology and display metrology, p. 60-68, 1999.

[15] A. Wolter, H. Schenk, E. Gaumont, H. Lakner**, “**MEMS microscanning mirror for barcode reading: from development to production”, SPIE proceeding of MOEMS display and imaging systems II, volume 5348, p. 32-39, 2004.

[16] H.R. Shea, A. Gasparyan, “Design for reliability of drift free MEMS microscanners”, SPIE proceeding of MEMS, MOEMS and micromachining, volume 5455, p. 44-53, 2004.

[17] A.Q. Liu, X.M. Zhang, V.M. Murukeshan, Q.X. Zhang, Q.B. Zou, S. Uppili, “An opticalcrossconnect (OXC) using drawbridge micromirrors”, Sensors and actuators A: physical, volume 97-98, p. 227-238, 2002.

[18] H. Xie, Y. Pan, G.K. Fedder, “Endoscopic optical coherence tomography imaging with a CMOS-MEMS micromirror”, Sensors and actuators A: physical, volume 103, p. 237-241, 2003.

[19] Y. Yee, H.J. Nam, S.H. Lee, J.U. Bu, J.W. Lee. “PZT actuated micromirror for fine tracking mechanism of high-density optical data storage”, Sensors and actuators A: physical, volume 89, p. 166-173, 2001.

[20] J. Comtois, A. Michalicek, W. Cowan, J. Butler, “Surface-micromachined polysilicon MOEMS for adaptive optics”, Sensors and actuators A: physical, volume 78, p. 54-62, 1999.

[21] G. Zhou, F.S. Chau, “Grating-assisted optical microprobing of in-plate and out-of-plane displacements of microelectromechanical devices”, IEEE/ASME journal of microelectromechanical Systems, volume 15, p. 388-395, 2006.

[22] S. Park, S.R. Chung, J. T.W. Yeow, "Design and analysis of stacked micromirrors in stacked configurations with moving electrodes", International journal of smart sensing and intelligent system, volume 1, p. 480-497, 2008.

[23] Y. Okano, Y. Hirabayashi, “Magnetically actuated micromirror and measurement system for motion characteristics using specular reflection”, IEEE journal on selected topics in quantum electronics, volume 8, p.19-25, 2002.

[24] C. Liu, Y.W. Yi, “Micromachined magnetic actuators using electroplated permalloy”, IEEE transactions on Magnetics, volume 35, p. 1976-1985, 1999.

[25] S. Schweizer, S. Calmes, M. Laudon, Ph. Renaud, “Thermally actuated optical microscanner with large angle and low consumption”, Sensors and actuators A: physical, volume 76, p. 470-477, 1999.

[26] M. Sasaki, T. Yamaguchi, J.H. Song, K. Hane, M. Hara, and K. Hori, “Optical scanner on a three-dimensional microoptical bench”, Journal of lightwave technology, volume 21, p. 602-608, 2003.

[27] A. Atre, "Analysis of out-of-plane thermal microactuators", Journal of micromechanics and microengineering, p. 205-213, 2006.

[28] F. Filhol, E. Defaÿ, C. Divoux, C. Zinck and M-T. Delaye, "Piezoelectric micromirrors for fast optical scanning with large angular deflection", Presented in IEEE/LEOS international conference on optical MEMS and their applications, Kagawa, Japan, p. 190-191, 2004.

[29] U. Baran, D. Brown, S. Holmstrom, D. Balma, W.O. Davis, P. Muralt, H. Urey, "Resonant PZT MEMS scanner for high-resolution displays", Journal of microelectromechanical systems, volume 21, p. 1303-1310, 2012.

[30] ANSYS Reference guide, release 13.

[31] E. L.Kinsler. "Fundamentals of acoustics", John Wiley and Sons, New York. p. 98-123, 1982.

[32] K. J.Bathe. "Finite element procedures" Prentice-Hall.Englewood Cliffs,1996.

[33] J.F. Sigrist, "Symmetric and non-symmetric formulations for fluid–structure interaction problems: reference test cases for numerical developments in commercial finite element code", proceeding of ASME pressure vessel and piping, Vancouver, 2006.

[34] A. Ricci, E. Giuri, "FSI analysis of microcantilevers vibrating in fluid environment", Proceeding of the COMSOL conference Milano 2009. http://www.cosmpl.com/papers/6747/down-load/Ricci.pdf

[35] G. De Pasquale, A. Soma, "Dynamic identification of electrostatically actuated MEMS in the frequency domain", Mechanical systems and signal processing 24, Elsevier, p. 1621-1633, 2010.

[36] Z. Hou, D. Xiao, X. Wu , P. Dong, Z. Chen, Z. Niu, X. Zhang, "Effect of axial force on the performance of micromachined vibratory rate gyroscopes", Sensors, p. 296-309, 2011.

[37] M.Breccolotti, F. Ubertini, I.Venanzi, "Natural frequencies of prestressed concrete beams: theoretical prediction and numerical validation", XIX congress IMETA, 2009.

[38] W. Davis "Measuring quality factor from a nonlinear frequency response with jump discontinuities", Journal of microelectromechanical Systems, volume 20, p. 968 -975, 2011.

[39] G. Li and H. Hughes, "Review of viscosity damping in micro-machined structures", Proceeding of SPIE, p. 30-46, 2000.

[40] W. Ye, X. Wang, W. Hemmert, D. Freeman, J. White, "Air damping in laterally oscillating microresonators: a numerical and experimental study", Journal of microelectromechanical systems, p. 557–566, 2003.

[41] M.K. Andrews, I. Harris, G. Turner, "A comparison of squeeze film theory with measurements on a microstructure", Sensors and actuators A: physical, volume 36, p. 79–87, 1993.

[42] M. Bao, H. Yang, "Squeeze film air damping in MEMS", Sensors and actuators A: physics, Volume 136, p. 3–27, 2007.

[43] X. Guo, A.A. Alexeenko, "Compact model of squeeze-film damping based on rarefied flow simulations", Journal of Micromechanics and microengineering, p. 045026(7pp), 2009.

[44] T. Veijola,“Compact models for squeeze-film dampers with inertial and rarefied gas effects”, Journal of micromechanics and microengineering, volume 14, p. 1109–1118, 2004.

[45] W. Ye, X. Wang, W. Hemmert, D. Freeman, J. White, “Air damping in laterally oscillating microresonators: a numerical and experimental study”, Journal of microelectromechanical systems, volume 12 , p. 557–566, 2003.

[46] T. Veijola, H. Kuisma, J. Lahdenpera, T. Ryhanen, “Equivalent-circuit model of squeezed gas film in a silicon accelerometer”, Sensors and actuators A: physical, volume 48, p. 239-248, 1995.

[47] S. Dushman, “Scientific foundations of vacuum technique”, Wiley, New York, 1949.

[48] A. Burgdorfer, “The Influence of the molecular mean free path on the performance of hydrodynamic gas lubricated bearings”, Journal of basic engineering, Transaction ASME, volume 8, p. 94-99, 1959.

[49] Y.T. Hsia and G.A. Domoto,” An experimental investigation of molecular rarefaction effects in gas lubricated bearing at ultra-low clearance”, Journal of lubrication technology, Transaction ASME, volume 105, p. 120-130, 1983.

[50] Y. Mitsuya, “Modified Reynolds equation for ultra-thin film gas lubrication using 1.5-order slip flow model and considering surface accommodation coefficient”, ASME journal of tribology, volume 115, p. 289-294, 1993.

[51] R.W. Barber, D.R. Emerson, “A numerical study of low Reynolds number slip flow in the hydrodynamic development region of circular and parallel plate ducts”, Daresbury laboratory technical report DL-TR-01-001, 2001.

[52] A.B Basset,” A treatise on hydrodynamics”, Cambridge university press, 1888.

[53] S.A. Schaaf, P.L. Chambre, “Flow of rarefied gases”, Princeton university Press, 1961.

[54] A. Agrawal, S.V. Prabhu, ”Survey on measurement of tangential momentum accommodation coefficient”, Journal of vacuum sciences and technology, volume 26, p. 634-645, 2008.

[55] B.E. Arkilic, “Measurement of the mass flow and tangential Momentum Accommodation coefficient in silicon micromachined channels”, Thesis, MIT, 1997.

[56] CRC handbook of chemistry and physics, 80th Ed., CRC Press, 1999-2000.

[57] H. Schlichting, “Boundary-layer theory”, 3rd English Ed., McGraw-Hill, 1968.

[58] T. Veijola, M. Turowski, “Compact damping models for laterally moving microstructures with gas-rarefaction effects”, Journal of microelectromechanical systems, volume 10, p. 263-73, 2001.

[59] Y. Cho, A.P. Pisano, R.T. Howe, “Viscous damping model for laterally oscillating microstructures”, Journal of microelectromechanical systems, volume 3, p. 81–87, 1994.

[60] A. Burgdorfer, “The influence of the molecular mean free path on the performance of hydrodynamic gas lubricated bearings”, Journal of basic engineering., Transaction. ASME, volume 81, p. 94–99, 1959.

[61] G.R. Thurston, “Theory of oscillation of a viscoelastic medium between parallel planes”, Journal of applied physics, volume 30/12, p. 1855–1860, 1959.

[62] J. Bryzek, K. Petersen, W. Mcculley, ”micromachines on the march”, IEEE spectrum, p. 20-31, 1994.

[63] J.J. Blech, “On isothermal squeeze films”, Journal of lubrication technology, volume 105, p. 615-620, 1983.

[64] W.S. Griffin, H.H. Richardson, S. Yamamami, “A study of fluid squeeze film damping”, Journal of basic engineering, Transaction ASME, P. 451-456, 1966.

[65] T. Klose, H. Conrad. T. Sandner, H. Schenk, “Fluid-mechanical damping analysis of resonant micromirrors with out of plane comb drive”, Proceeding of COMSOL conference. Hannover. 2008

[66] W. Zhang, K. Turner, “Frequency dependent fluid damping of micro/nano flexural resonators: experiment, model and analysis”, Sensors and actuators A: physical, volume 134, p. 594-599, 2007.

[67] S.S. Mohite, V.R. Sonti, R. Pratap, “A compact squeeze-film model including inertia, compressibility, and rarefaction effect for perforated 3-D MEMS structures”, Journal of microelectromechanical systems, volume 17, p. 709-723, 2008.

[68] W.McC. Siebert. “Circuits, signals, and systems”, MIT Press, 1985.

[69] B.L. Foulgoc, T. Bourounia, I.L. Traon, A. Bosseboeuf, F. Marty, C. Breluzeay, J-P Grandchamp,S Masson, “Highly decoupled single-crystal Silicon resonators: an approach for the intrinsic quality factor”, Journal of micromechanics and Microengineering, p. 160-168, 2006.

[70] www.tf.uni-kiel.de/matwis/amat/semithech-en/kap_7/illustr/i7_1_2.html

[71] www.economist.com/node/539772

[72] www.directindustry.com/prod/keyence-deutschland/

[73] www.electronics.dit.ie/staff/gfarrell/optmultiplexnet.html

[74] H. Dong, “Design and analysis of a MEMS comb vibratory gyroscope”, Master thesis, University of Bridgeport, 2009.

[75] A.Frangi, A. Ghisi and L. Coronato, “On a deterministic approach for the evaluation of gas damping in inertial MEMS in the free-molecule regime”, Sensors and actuators A: physical, volume 149, p. 21-28, 2009.

[76] C. Ataman, O. Kaya, H Urey, “Analysis of parametric resonances in comb-driven microscanners”, Proceeding of SPIE 5455, p. 128-136, 2004.

[77] C. Ataman, “Design, modeling and characterization of electrostatically actuated microscanner-rs”, Thesis for MSc, Koc University, 2004.